Intensity-dependent phase shifts in optical materials for quantum state preparation and absorption measurements in thin film coatings and bulk material

Dissertation
zur Erlangung des Doktorgrades
an der Fakultät für Mathematik, Informatik und Naturwissenschaften
Fachbereich Physik
der Universität Hamburg

Vorgelegt von

Amrit Pal Singh

Hamburg

2018

Gutachter der Dissertation:	Prof. Dr. Roman Schnabel Prof. Dr. Henning Moritz
Zusammensetzung der Prüfungskommision:	Prof. Dr. Roman Schnabel Prof. Dr. Henning Moritz Prof. Dr. Dieter Horns Prof. Dr. Ludwig Mathey Prof. Dr. Günter Huber
Vorsitzende der Prüfungskommission:	Prof. Dr. Dieter Horns
Datum der Disputation:	25.05.2018
Vorsitzender Fach-Promotionsausschusses PHYSIK:	Prof. Dr. Wolfgang Hansen
Leiter des Fachbereichs PHYSIK:	Prof. Dr. Michael Potthoff
Dekan der Fakultät MIN:	Prof. Dr. Heinrich Graener

Abstract

Squeezed vacuum states of light can be used to enhance the sensitivity of high-precision measurement devices such as gravitational-wave detectors and they also can be utilized in quantum key distribution. The state-of-the-art method for the generation of squeezed vacuum states is the optical-parametric down-conversion. Another technique to create squeezed vacuum states is the cascaded optical Kerr effect. In this thesis I show for the first time a zero-span measurement of a Kerr-squeezed vacuum state with a nonclassical noise reduction of (2.0 ± 0.1) dB at a sideband frequency of 358.26 MHz and of (2.5 ± 0.1) dB at 1074.78 MHz, using a wavelength of 1550 nm.

The dominating noise source of gravitational-wave detectors in the mid-frequency range between 30 Hz and 100 Hz is coating thermal noise. An approach to reduce this noise source is the use of crystalline multilayer mirror coatings made of GaAs and $Al_{0.92}Ga_{0.08}As$. Due to the large circulating power in a gravitational-wave detector, the optical coating absorption needs to be below 1 ppm. In this thesis I investigate the optical absorption of these coatings with the photothermal self-phase modulation technique and finite element simulations with COMSOL Multiphysics. At 1064 nm, an absorption of (0.38 ± 0.02) ppm was detected and at 1550 nm an absorption of (0.65 ± 0.02) was observed.

For the MassQ project, sapphire test masses with low optical substrate absorption are needed to allow for a cryogenic operation. For this reason I have measured the absorption of two sapphire test masses from the same ingot at a wavelength of 1064 nm using cavity round-trip loss measurements. The detected bulk absorption was (2931 ± 22) ppm/cm.

Kurzfassung

Gequetsche Vakuumzustände des Lichts finden ihre Anwendung in der Verbesserung der Empfindlichkeit von hochpräzisen Messinstrumenten wie Gravitationswellendektektoren und in der Quantenschlüsselverteilung. Die am häufigsten angewendete Methode zur Erzeugung von gequetschten Vakuumzuständen ist die optische parametrische Abwärtskonversion. Eine weitere Methode um gequetschte Vakuumzustände herzustellen ist der kaskadierte optische Kerr-Effekt. In dieser Arbeit zeige ich zum ersten Mal eine mit Hilfe des kaskadierten Kerr-Effekts erzeugte nicht-klassische Rauschunterdrückung von (2.0 ± 0.1) dB bei einer Seitenbandfrequenz von 358.26 MHz und von (2.5±0.1) dB bei 1074.78 MHz, wobei eine Wellenlänge von 1550 nm verwendet wurde.
Die dominierende Störquelle in Gravitationswellendetektoren in dem Frequenzbereich zwischen 30 Hz und 100 Hz ist die thermische Bewegung der Spiegeloberflächen. Eine Möglichkeit diese zu reduzieren ist die Verwendung von kristallinen Spiegelbeschichtungen, welche aus abwechselnden Lagen GaAs und $Al_{0.92}Ga_{0.08}As$ bestehen. Aufgrund der hohen umlaufenden Lichtleistungen in einem Gravitationswellendetektor sollte des weiteren die optische Absorption der Spiegelbeschichtungen unter 1 ppm liegen. In dieser Arbeit untersuche ich die optische Absorption der kristallinen Spiegelbeschichtungen mit Hilfe der thermischen Selbstphasenmodulation und durch finite Elemente Simulationen, die mit COMSOL Multiphysics durchgeführt wurden. Bei 1064 nm wurde eine Absorption von (0.38 ± 0.02) ppm gemessen und bei 1550 nm eine Absorption von (0.65 ± 0.02) ppm.
Für das Projekt MassQ werden Testmassen aus Saphir mit einer geringen optischen Absorption gebraucht, um ein Kühlen auf kryogene Temperaturen zu ermöglichen. Deshalb habe ich in dieser Arbeit die Absorption von zwei Testmassen aus Saphir bei 1064 nm gemessen, welche aus dem selben Block gefertigt wurden. Durch die Messung der Umlaufverluste von optischen Resonatoren wurde eine Absorption von (2931 ± 22) ppm/cm ermittelt.

Contents

List of Figures

Glossary

BHD balanced homodyne detection
BS beam splitter
DBS dichroic beam splitter
ETM end test mass
EOM electro-optical modulator
FEA finite element analysis
FI faraday isolator
FSR free spectral range
FWHM full width at half maximum
ITM input test mass
LO local oscillator
MC mode-cleaner
MZI Mach-Zehnder interferometer
OMC output mode-cleaner
PD photo diode
PDH Pound-Drever-Hall
PPKTP periodically-poled potassium titanyl phosphate
PRM power-recycling mirror
PZT piezoelectric transducer
RBW resolution bandwidth
SHG second harmonic generation
SRM signal-recycling mirror
VBW video bandwidth

Chapter 1

Introduction and outline of this thesis

In this thesis, intensity-dependent phase shifts based on two different effects are used to generate squeezed vacuum states and to obtain the optical absorption of crystalline multilayer coatings made of GaAs and $Al_{0.92}Ga_{0.08}As$.
The first effect is the cascaded optical Kerr effect. It describes a special form of the phase shift of light that passes trough a second-order nonlinear medium, where the phase shift is caused by an intensity-dependent refractive index. The cascaded optical Kerr effect can be used to introduce correlations in the quantum noise and thus, to produce squeezed states of light. The second effect, leading to an intensity-dependent phase shift is the so-called thermal Kerr effect. Light power absorbed in an optical material is converted into heat. The thermal expansion coefficient of the material causes a thermally-induced length change of the material. This length change, as well as the thermally-induced change of the refractive index caused by the thermoelastic coefficient, leads to a phase shift of light that passes through the material. In this thesis, the thermal Kerr effect is used to obtain the optical absorption of crystalline GaAs/$Al_{0.92}Ga_{0.08}As$ coatings.
Furthermore, the substrate absorption of sapphire is measured using cavity round-trip loss measurements. At cryogenic temperatures, sapphire is a suitable material for optomechanical experiments.

This thesis has the following structure:

- Chapter 2 first introduces the theoretical foundations from nonlinear optics and quantum optics that are essential for the understanding of the generation of squeezed light. Then, the experimental setup for the production of squeezed vacuum states by means of the cascaded optical Kerr effect as well as the measurement results are presented.

- Chapter 3 begins with an introduction about gravitational-wave detectors and describes coating thermal noise as the limiting noise source within the frequency range

between 30 Hz and 100 Hz. Then crystalline GaAs/$Al_{0.92}Ga_{0.08}As$ coatings as a possible solution to decrease this noise source are introduced. After that, the theory of thermal effects as well as the measurement and data evaluation method for obtaining the coating absorption are presented. Then, the experimental setup is explained and the measurement results at 1064 nm and 1550 nm at are shown.

- Chapter 4 first describes why sapphire is a suitable material for experiments performed at cryogenic temperatures. Then, the measurement method for the substrate absorption at 1064 nm and the experimental setup are described. At the end, the obtained measurement results are presented.

- Chapter 5 summarizes the results of this thesis.

Chapter 2

Continuous-wave squeezed-light generation via the cascaded optical Kerr effect

2.1 Introduction

The state-of-the-art process that is used to generate squeezed vacuum states of light is the degenerate parametric down-conversion. During this process, a pump photon interacts with a second-order nonlinearity and decays into two new photons with the same frequency, which show quantum correlations [9]. In 1986 the parametric down-conversion was first used by Wu et al. [93] to show a nonclassical noise reduction of 3.5 dB below the vacuum noise level and in 2017 Vahlbruch et al. [88] demonstrated the generation of vacuum squeezing of 15 dB. Modern squeezing experiments based on the degenerate parametric down-conversion employ one resonator for the generation of the frequency-doubled light that is used as pump for the squeezing resonator. A simpler concept for the production squeezed light is provided by the third-order nonlinear optical Kerr effect. It uses the phase shift gained by the intensity-dependence of the refractive index to transform the vacuum noise and thus, to produce squeezing [9]. Due to the small third-order nonlinearities, only experiments in the pulsed laser regime succeeded in the generation of squeezed states by means of the optical Kerr effect. Heersink et al. [39] demonstrated the generation of bright squeezing of 5.1 dB by using optical fibers and laser pulses. The second-order nonlinear cascaded optical Kerr effect mimics a third-order nonlinearity and can be used for the generation of squeezed light in the continuous-wave laser regime [91]. The generation of bright squeezed light of 1.5 dB was achieved by Zhang et al. [94]. To the best of my knowledge, the production of squeezed vacuum states in the continuous-wave laser regime using the cascaded optical Kerr effect has not been realized so far. Strong Kerr squeezed vacuum

states can be used to create wigner functions with a non-gaussian probability distribution [47, 68].

2.2 Nonlinear optics

In this section, nonlinear interactions such as the optical Kerr effect, the second harmonic generation and the cascaded optical Kerr effect are introduced. This section follows the references [18, 34, 45, 48, 59, 65].

2.2.1 The optical Kerr effect

When an electric field $E(\omega)$ enters a medium, for example a crystal, it displaces the electrons of the atoms of the material and induces electric dipole moments. For weak strengths, and thus small displacements, the restoring forces are proportional to the electrical field and the dipoles radiate an electric field with the same frequency ω as the incident field. If the field strengths are large, the response of the medium depends in a nonlinear way on the electric field. Then, the dipole moment per unit volume, the so called polarization $P(\omega)$, can be written as ([18], p. 2)

$$P(\omega) = \epsilon_0 \left[\chi^{(1)} E(\omega) + \chi^{(2)} E^2(\omega) + \chi^{(3)} E^3(\omega) + ... \right]. \tag{2.1}$$

The quantities $\chi^{(1)}$, $\chi^{(2)}$ and $\chi^{(3)}$ are the first, second and third-order nonlinear susceptibilities. A resulting third-order effect is the intensity-dependent refractive index ([18], p. 11)

$$n(I) = n_0 + n_2 I, \tag{2.2}$$

which is also called optical Kerr effect. Here n_0 is the weak-field refractive index and n_2 is the second-order refractive index which increases proportional to the intensity $I = E^2(\omega)$. The relationship between n_2 and the third-order susceptibility is given by ([18], p. 12)

$$n_2 = \frac{3\chi^{(3)}}{4 n_0^2 \epsilon_0 c}, \tag{2.3}$$

where ϵ_0 is the vacuum permittivity and c is the speed of light. By the use of equation (2.2), the phase shift of a plane wave that passes through a third-order nonlinear Kerr medium with a geometrical length d and an optical length $L_{\text{opt}} = nd$, can be calculated to ([45], p. 37)

$$\Phi = k L_{\text{opt}} = k n_0 d + k n_2 d I = \Phi_0(d) + \Phi_{\text{Kerr}}(d). \tag{2.4}$$

Here, $k = 2\pi/\lambda$ is the wave number and λ the wavelength. The wave has gained a phase shift due to the linear refractive index n_0 and an intensity-dependent phase shift because of the second-order refractive index n_2.

2.2.2 Second harmonic generation and the cascaded optical Kerr effect

In the process of the second harmonic generation (SHG), light at the fundamental frequency ω_1 polarizes a medium with a second-order susceptibility $\chi^{(2)}$ and a polarization wave is generated. The polarization wave radiates light with the frequency ω_1 and with $\omega_2 = 2\omega_1$, the second harmonic light field. The photon picture illustrates the energy conservations during this process. Two photons with the fundamental frequency ω_1 are annihilated and at the same time, a photon with frequency $\omega_2 = 2\omega_1$ is created (see figure 2.3a). The differential equations that describe the fundamental and the SHG field in the case of plane waves in a loss-free medium are ([18], p. 98)

$$\frac{dE_1}{dz} = \frac{2i\omega_1^2 d_{\text{eff}}}{k_1 c^2} E_2 E_1^* e^{-i\Delta k z} \tag{2.5}$$

and

$$\frac{dE_2}{dz} = \frac{i\omega_2^2 d_{\text{eff}}}{k_2 c^2} E_1^2 e^{i\Delta k z}. \tag{2.6}$$

Here E_1 and E_2 denote the amplitudes of the fundamental and second harmonic field, k_1 and k_2 are the corresponding wave numbers and c is the speed of light. The magnitude

$$\Delta k = 2k_1 - k_2 \tag{2.7}$$

is the wave vector mismatch that describes the conservation of momentum during the SH generation. While the fundamental wave as well as the induced polarization wave travel with velocity $v_{\text{ph, f}} = n_1\omega_1/c$ through the nonlinear medium, the second harmonic field has the velocity $v_{\text{ph, shg}} = n_2\omega_2/c$. As a consequence of dispersion, with $n_2 > n_1$, the fundamental field with wavelength λ_1 and the SHG field become dephased. After the coherence length [34]

$$L_{\text{coh}} = \frac{\lambda_1}{4(n_2 - n_1)}, \tag{2.8}$$

the phase difference is π. Thus, the SHG waves generated at different places inside of the nonlinear medium interfere destructively. After the distance $2L_{\text{coh}}$, the SHG field has vanished completely. To ensure an efficient SHG conversion along the complete nonlinear

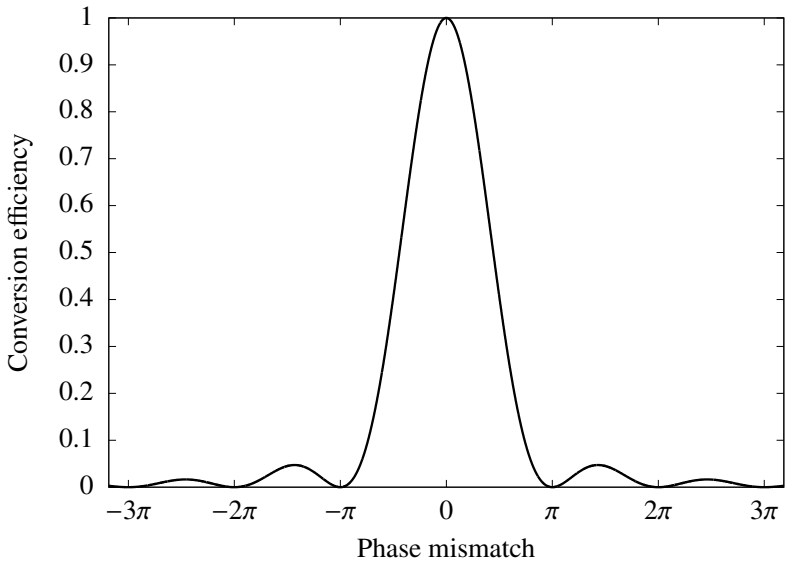

Figure 2.1: Simulated SHG conversion efficiency for a single pass through a nonlinear medium in the case of plane waves. A maximum conversion from the fundamental to the second harmonic light is achieved for a wave-vector mismatch of $\Delta k = 0$. The first conversion minima are located at $\pm\pi$.

medium, the fundamental and the SHG wave have to travel with the same velocity. To fulfill this condition, the wave-vector mismatch has to vanish, $\Delta k = 0$. In this case, the refractive indices have to satisfy the condition $n_1 = n_2$, the nonlinear medium is now phase matched. To experimentally achieve the phase matching condition, birefringent crystals together with type I or type II phase matching can be used. A third alternative is the quasi-phase matching.

For a small conversion, the amplitude of the fundamental field is considered to be constant, $A_1 \approx \text{const}$, and equation (2.6) can be integrated over the length L of the nonlinear medium ([18], p. 78)

$$I_2 = |E_2^2| \propto I_1^2 L^2 \left(\frac{\sin\left(\frac{\Delta kL}{2}\right)}{\frac{\Delta kL}{2}} \right)^2 = I_1^2 L^2 \,\mathrm{sinc}\left(\frac{\Delta kL}{2}\right)^2 . \tag{2.9}$$

The second harmonic intensity I_2 scales proportional to L^2 and the square of the fundamental power I_1. From this result, the conversion efficiency can be deduced to

$$\eta(\Delta k) = \frac{I_2}{I_1} \propto \mathrm{sinc}\left(\frac{\Delta kL}{2}\right)^2 . \tag{2.10}$$

The dependence of $\eta(\Delta k)$ on the wave-vector mismatch Δk is shown in figure 2.1 for a single pass through the nonlinear medium. For a wave-vector mismatch of $\Delta k = 0$, the

conversion efficiency shows a maximum, while the first conversion minima are located at $\Delta k = \pm\pi$. In an experiment, the total achievable conversion would be limited by absorption inside of the nonlinear crystal. Another possible solution of equations (2.5) and (2.6) can be obtained with the function ([48], p. 25)

$$E_1(z) = |E_1|e^{i\Phi(z)}. \tag{2.11}$$

Equation (2.11) represents a fundamental field with a constant amplitude $|E_1|$ and a variable phase $\Phi(z)$ that depends on the spatial coordinate z.
The phase of the fundamental field can be calculated as ([48], p. 26)

$$\Phi(z) = \Phi_0(z) + \frac{\Delta k z}{8 + \frac{\Delta k^2}{2\kappa_{\mathrm{NL}}^2 I_1}}\left(1 - \operatorname{sinc}\left(\sqrt{\left(\frac{\Delta k}{2}\right)^2 + 4\kappa_{\mathrm{NL}}^2 I_1 z}\right)\right), \tag{2.12}$$

with

$$\kappa_{\mathrm{NL}}^2 = \frac{\pi^2 d_{\mathrm{eff}}^2}{\lambda_1^2 n_1 n_2}. \tag{2.13}$$

The constant κ_{NL}^2 includes the effective second-order nonlinearity $d_{\mathrm{eff}} = \frac{1}{2}\chi^{(2)}$, the wavelength λ_1 of fundamental field and the refractive indices n_1 and n_2 of the fundamental and harmonic field. The first term in equation (2.12) is the phase due to propagation of the fundamental field. The second term that depends on the intensity of the fundamental field, $I_1 = |E_1|^2$, characterizes an additional intensity-dependent phase shift. In the maximum SHG conversion, where $\Delta k = 0$, the intensity-dependent phase shift vanishes. In contrast, it is maximized in the first conversion minima of the second harmonic field (see figure 2.1), where it becomes ([48], p. 26)

$$\Phi(z) = \Phi_0(z) \pm \frac{\kappa_{\mathrm{NL}}^2 z^2}{\pi} I_1. \tag{2.14}$$

For a nonlinear medium of length d, this equation has a similar form as equation (2.4) which describes the nonlinear phase shift due to the third-order optical Kerr effect. Thus, a second-order nonlinear medium can be used to mimic the intensity-dependent phase shift that is provided by a third-order nonlinear medium. Since $\chi^{(2)}$ is several orders of magnitude larger than $\chi^{(3)}$, the cascaded Kerr effect provides a possibility to explore the intensity-dependent phase shift in the continuous-wave laser regime.
The intensity-dependent phase shift can be conceptually described with a Mach-Zehnder-interferometer containing two nonlinear second-order media ([48], p. 27) which is depicted

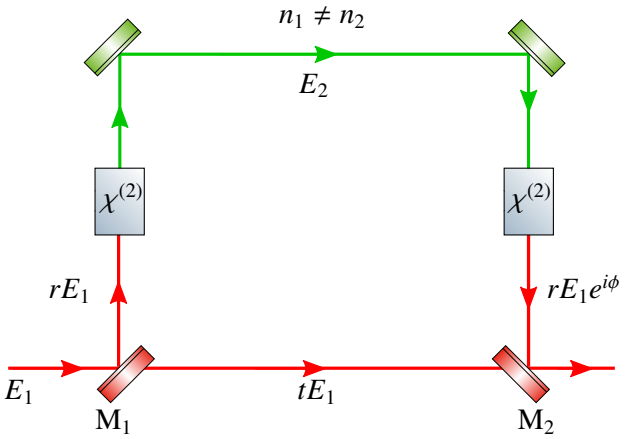

Figure 2.2: Illustration of the nonlinear Kerr phase shift with a Mach-Zehnder interferometer (MZI). First, the incident fundamental field with amplitude E_1 is divided by M_1 into a transmitted part tE_1 and a reflected part rE_1. The latter is up-converted to the SHG field by the $\chi^{(2)}$ medium in the left arm of the MZI, while the transmitted part of the fundamental field propagates towards mirror M_2. The $\chi^{(2)}$ medium in the right arm of the MZI converts the SHG field back to the fundamental. Since the system is not phase matched, $n_1 \neq n_2$, and the up- and down converted part of the fundamental light has gained a phase shift $e^{i\Phi}$. Both parts of the fundamental field are superimposed at mirror M_2. Thus, the resulting fundamental field has gained an intensity-dependent phase shift. Adapted from ([48], p. 27).

in figure 2.2. First, the incident fundamental field E_1 is divided by mirror M_1 into the reflected part rE_1 and the transmitted part tE_1. The first nonlinear medium on the left hand side converts the reflected part rE_1 into the second harmonic field E_2. E_2 propagates until the second nonlinear medium, experiencing a phase shift due to the refractive index n_2. The second nonlinear medium converts E_2 back to the fundamental field $rE_1e^{i\phi}$. The transmitted part of the fundamental field tE_1 propagates towards M_2 experiencing a phase shift due to the refractive index n_1. Both fields are superimposed at M_2 where $rE_1e^{i\phi}$ gets completely reflected and tE_1 gets fully transmitted. In the case of a large phase mismatch $\Delta k \neq 0$, the refractive indices are not equal, $n_1 \neq n_2$. Consequently, both parts of the fundamental field have experienced different optical path lengths and the up- and down converted part of the field has gained an additional phase shift $e^{i\phi}$. Therefore, the overall fundamental field leaving the Mach-Zehnder interferometer has obtained a phase shift.

The previous calculations are valid for a second-order nonlinear medium that is made of a single crystal. The nonlinear second-order crystal used in this work is made of periodically poled potassium titanyl phosphate (PPKTP) and is divided into several domains. Each domain has the length L_{coh} and the sign of the spontaneous polarization is periodically reversed in every domain. Thus, the phase difference between fundamental and SHG field is restored after each coherence length and the SHG field continues to grow. Because of the temperature dependence of the refractive indices n_1 and n_2 and due to thermal expansion, the length of the domains can be altered as a function of the temperature [34]. If each domain has the length L_{coh}, the PPKTP crystal is perfectly quasi-phase matched and optimum conversion from the fundamental to the second harmonic field is achieved. In this case, the fundamental field does not experience an intensity-dependent phase shift. To reach the first conversion minimum, the length of the domains is temperature-tuned and the quasi-phase matching is worsened. Similar to a single crystal, the fundamental field gains an intensity-dependent phase shift in the conversion minimum [59].

The two cascaded nonlinear interactions of the Kerr effect, SHG and down conversion, are illustrated in the photon picture in figure 2.3. In the SHG process, an atom of the crystal lattice absorbs two photons at the fundamental frequency ω_1. After that, it decays and a photo with frequency $\omega_2 = 2\omega_1$ is emitted. During the down conversion process, an atom of the crystal lattice absorbs a photon with the frequency $\omega_2 = 2\omega_1$. In a subsequent decay two photons with the frequency ω_1 are radiated. The solid horizontal line describes the ground state and the dashed lines are virtual energy levels.

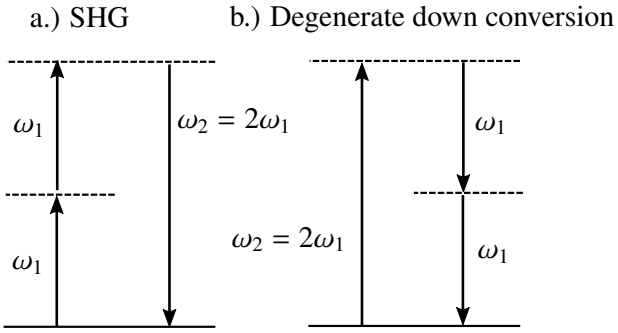

Figure 2.3: Nonlinear interactions of the cascaded Kerr effect in the photon picture. a.) During the SHG process, two fundamental photons with frequency ω_1 are absorbed by an atom of the crystal lattice and one photon with frequency $\omega_2 = 2\omega_1$ is created. The opposite process takes place in the degenerate down conversion interaction, shown in b.). Here one photon with the frequency $\omega_2 = 2\omega_1$ is absorbed and subsequently, the atom radiates two photons with frequency ω_1. Adapted from ([18], p. 5, p. 9).

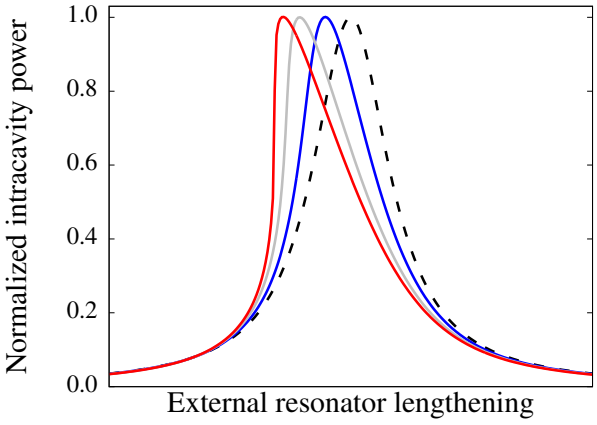

Figure 2.4: Simulated and normalized intracavity power of a nonlinear Kerr resonator. Initially, the resonator length is tuned to the left hand side of the resonance and all light is reflected. If the round-trip length is externally increased and the resonance is approached, light enters the cavity and starts to build up. The nonlinear Kerr medium produces an intensity-dependent phase shift that corresponds to an additional increase of the round-trip length. As a consequence, the intracavity power rises further, leading to a large Kerr-induced phase shift and vice versa. The blue, gray and red graph illustrate the resulting Kerr-induced resonance peak deformation for increasing intensity-dependent phase shifts while the dashed black curve shows the cavity resonance without Kerr medium.

2.2.3 Kerr medium inside of an optical resonator

The intracavity power $|A|^2$ of a two-mirror resonator containing a nonlinear Kerr medium is given by ([45], p. 52), [84]

$$|A|^2 = \frac{1 - R_1}{1 - R_1 R_2 - 2\sqrt{R_1 R_2}\cos\left[2\left(\Phi + \theta_K |A|^2\right)\right]} |A_{in}|^2. \tag{2.15}$$

Here R_1 and R_2 are the mirror power reflectivities, Φ is the geometric cavity detuning, $|A_{in}|^2$ is the incident laser power and θ_K is a constant that includes material specific parameters of the nonlinear medium as well as further resonator parameters. For a second-order nonlinear medium, θ_K is given by the second term in equation (2.14). The product $\theta_K |A|^2$ is the intensity-dependent phase shift. The implicit equation (2.15) was numerically solved with the program N.L.C.S. (the nonlinear cavity simulator, a detailed description can be found in ([50], pp. 21-59) in the first SHG conversion minimum at $\Delta k = \pi$, where the intensity-dependent phase shift due to the cascaded Kerr effect has a positive sign. While the blue, gray and red curves in figure 2.4 show the solution of equation (2.15) for increasing Kerr phase shifts, the dashed black graph depicts the solution for the same cavity without Kerr medium. To understand the resonance peak deformation, let us first consider an off resonant detuning on the left hand side of the resonance, where all incident pump light gets reflected. If the cavity length is externally increased and the resonance is approached, light enters the cavity and starts to build up. Consequently, the nonlinear Kerr medium produces an intensity-dependent phase shift that corresponds to an additional resonator lengthening. The extra lengthening results again in an increase of the intracavity power and so on. Thus, the nonlinear Kerr medium produces a positive feedback and the maximum of the cavity resonance is reached in a faster time than without a Kerr medium. For this reason, the left hand side of the cavity resonance shows a steep slope while the right hand side features a shallow slope. In the case of the red curve in figure 2.4, the left hand side of the cavity resonance shows an infinite slope. This regime can be used to increase the sensitivity of a gravitational-wave detector [67].

2.3 Quantum-mechanical states of light

In this section, the quantization of the electric field and coherent states, number states and squeezed states are introduced. The generation of squeezed light with nonlinear second-order media and its detection is shown. Also, the impact of optical losses on squeezed light is discussed. This section is based on the references [14, 17, 22, 27, 52, 56, 65, 66, 71, 72, 78, 89, 90].

2.3.1 Expectation value, variance and uncertainty principle

In quantum mechanics, physical quantities like position and momentum are called observables and are characterized by an operator $\hat{A}$. For a given quantum-mechanical state $|\Psi\rangle$ the expectation value of $\hat{A}$ can be calculated to ([22], p. 17)

$$\langle \hat{A} \rangle = \langle \Psi | \hat{A} | \Psi \rangle . \tag{2.16}$$

For a large number of measurements, the expectation value $\langle \hat{A} \rangle$ characterizes the average value. The variance $(\Delta \hat{A})^2$ which describes the quadratic fluctuations around the expectation values is defined as ([90], pp. 40-41)

$$(\Delta \hat{A})^2_\Psi = \langle \hat{A}^2 \rangle - \langle \hat{A} \rangle^2 = \langle \Psi | \hat{A}^2 | \Psi \rangle - \langle \Psi | \hat{A} | \Psi \rangle^2 . \tag{2.17}$$

Thus, the standard deviation which corresponds to the uncertainty of the physical quantity represented by operator $\hat{A}$, is calculated by taking the square root of equation (2.17)

$$(\Delta \hat{A})_\Psi = \sqrt{\langle \hat{A}^2 \rangle - \langle \hat{A} \rangle^2} = \sqrt{\langle \Psi | \hat{A}^2 | \Psi \rangle - \langle \Psi | \hat{A} | \Psi \rangle^2}. \tag{2.18}$$

According to Heisenberg's uncertainty principle, two observables, characterized by the operators $\hat{A}$ and $\hat{B}$ cannot be measured simultaneously with arbitrary precision. If observable $\hat{A}$ is determined with high accuracy, this comes at the expense of an increased uncertainty in observable $\hat{B}$. For the variances of the operators $\hat{A}$ and $\hat{B}$, this is illustrated by the inequality ([90], p. 43)

$$(\Delta \hat{A})^2_\Psi (\Delta \hat{B})^2_\Psi \geq \frac{1}{4} \left| \langle [\hat{A}, \hat{B}] \rangle \right|^2. \tag{2.19}$$

The quantity $[\hat{A}, \hat{B}]$ on the right hand side of equation (2.19) is called commutator. It is defined as ([90], p. 37)

$$[\hat{A}, \hat{B}] = \hat{A}\hat{B} - \hat{B}\hat{A}. \tag{2.20}$$

If equation (2.20) is equal to zero, then $\hat{A}\hat{B} = \hat{B}\hat{A}$ and $\hat{A}$ and $\hat{B}$ commute. In this case, the observables described by $\hat{A}$ and $\hat{B}$ can be measured simultaneously with arbitrary precision. The Heisenberg uncertainty principle can also be written by using the standard deviations instead of the variances, yielding

$$(\Delta A)_\Psi (\Delta B)_\Psi \geq \frac{1}{2} \left| \langle [\hat{A}, \hat{B}] \rangle \right|. \tag{2.21}$$

2.3.2 Quadrature operators and quantization of the optical electric field

The wave equation in an isotropic medium is given by ([14], p. 13)

$$\nabla^2 \vec{E}(\vec{r},t) - \frac{1}{c^2}\frac{\partial^2}{\partial t^2}\vec{E}(\vec{r},t) = 0. \tag{2.22}$$

Here $\vec{E}(\vec{r},t)$ is the electric field, t is the time, $\vec{r}$ is the spatial coordinate and c is the speed of light. A solution of equation (2.22) is

$$\vec{E}(\vec{r},t) = E_0 \left[\alpha(\vec{r},t)\, \mathrm{e}^{\mathrm{i}\omega t} + \alpha^*(\vec{r},t)\, \mathrm{e}^{-\mathrm{i}\omega t}\right] \vec{p}(\vec{r},t), \tag{2.23}$$

where $\omega = 2\pi f$ is the angular frequency and f is the frequency in Hz. $\vec{p}(\vec{r},t)$ is the polarization of the wave and the complex and dimensionless amplitude $\alpha(\vec{r},t)$ characterizes its spatial shape. In the case of a monochromatic plane wave that propagates in direction z, the amplitude becomes

$$\alpha(z) = \alpha_0 \mathrm{e}^{-\mathrm{i}kz}. \tag{2.24}$$

$k = 2\pi/\lambda$ is the wave number, $\lambda = c/nf$ is the wavelength and n the refractive index of the medium. Using the quadrature amplitudes ([14], p. 17)

$$X_1 = \alpha(\vec{r},t) + \alpha^*(\vec{r},t) \tag{2.25}$$

and

$$X_2 = -\mathrm{i}\left[\alpha(\vec{r},t) - \alpha^*(\vec{r},t)\right], \tag{2.26}$$

equation (2.23) can be rewritten as

$$\vec{E}(\vec{r},t) = E_0 \left[X_1 \cos(\omega t) - X_2 \sin(\omega t)\right] \vec{p}(\vec{r},t). \tag{2.27}$$

X_1 and X_2 are called amplitude and phase quadrature. They are the amplitudes of two oscillating fields which are 90° out of phase.
In a ring cavity with round-trip length L only modes which satisfy the condition ([14], p. 61)

$$\lambda = \frac{L}{m},\ m = 1, 2, 3... \tag{2.28}$$

can be resonant. The energy of the cavity modes can be expressed as ([14], p. 61)

$$H = \sum_i \frac{\hbar\omega_i}{4}\left(X_{1_i}^2 + X_{2_i}^2\right), \tag{2.29}$$

where i denotes the different cavity modes and $\hbar$ is the reduced Planck constant. From now on, the treatment will be restricted for simplicity to a single mode of the electric field. Thus, the energy of a single cavity mode with angular frequency ω is

$$H = \frac{\hbar\omega}{4}\left(X_1^2 + X_2^2\right). \tag{2.30}$$

To perform the transition to quantum mechanics, amplitude and phase quadrature can be replaced by the corresponding operators ([14], p. 68)

$$\hat{X}_1 = \hat{a} + \hat{a}^\dagger \tag{2.31}$$

and

$$\hat{X}_2 = -\mathrm{i}(\hat{a} - \hat{a}^\dagger) = \mathrm{i}(\hat{a}^\dagger - \hat{a}). \tag{2.32}$$

$\hat{a}$ and $\hat{a}^\dagger$ are the annihilation and creation operators that fulfill the boson commutator relations ([14], p. 64)

$$[\hat{a}, \hat{a}] = [\hat{a}^\dagger, \hat{a}^\dagger] = 0 \tag{2.33}$$

and

$$[\hat{a}, \hat{a}^\dagger] = 1. \tag{2.34}$$

With regard to calculations in later sections, it is useful to define the general quadrature operator ([89], p. 45)

$$\hat{X}_\vartheta = \hat{a}\mathrm{e}^{-\mathrm{i}\vartheta} + \hat{a}^\dagger\mathrm{e}^{\mathrm{i}\vartheta}, \tag{2.35}$$

where ϑ is the quadrature angle. $\vartheta = 0$ yields the amplitude quadrature $\hat{X}_1$ while $\vartheta = \pi/2$ results in the phase quadrature $\hat{X}_2$. The quadrature operators $\hat{X}_1$ and $\hat{X}_2$ satisfy the commutator relation ([89], p. 16)

$$[\hat{X}_1, \hat{X}_2] = 2\mathrm{i}. \tag{2.36}$$

Consequently, $\hat{X}_1$ and $\hat{X}_2$ cannot be measured simultaneously with arbitrary precision and thus, obey the uncertainty relation

$$\Delta\hat{X}_1 \Delta\hat{X}_2 \geq \frac{1}{2}|\langle[\hat{X}_1, \hat{X}_2]\rangle| = 1. \tag{2.37}$$

If one quadrature is measured precisely, the uncertainty in the opposite quadrature will rise. Using the quadrature operators defined in (2.31) and (2.32), equation (2.30) can be rewritten as the Hamiltonian ([22], p. 14)

$$\hat{H} = \hbar\omega\left(\hat{a}^\dagger\hat{a} + \frac{1}{2}\right) = \hbar\omega\left(\hat{n} + \frac{1}{2}\right), \tag{2.38}$$

where

$$\hat{n} = \hat{a}^\dagger\hat{a} \tag{2.39}$$

is the number operator which quantifies the number of photons in a single mode of the electric field and $\hbar\omega$ is the corresponding photon energy of one photon. Thus, each cavity mode can be described by a quantized harmonic oscillator. $\hat{H}$ yields the discrete and equally spaced energy spectrum ([37], p. 14)

$$E_n = \hbar\omega\left(n + \frac{1}{2}\right). \tag{2.40}$$

It becomes obvious that even if a mode is not occupied by any photon, it still exhibits the so called zero point energy

$$E_0 = \frac{\hbar\omega}{2}. \tag{2.41}$$

2.3.3 Number states

The eigenstates of the number operator $\hat{n} = \hat{a}^\dagger\hat{a}$ are the number states $|n\rangle$, also called Fock states. Since they are orthogonal $\langle n|m\rangle = \delta_{mn}$ and complete $\sum_{n=0}^{\infty} |n\rangle\langle n| = 1$ ([89], p. 11), they form a basis of a Hilbert space. Applying the number operator on a number state yields the number of photons n inside of a single mode ([14], p. 64):

$$\hat{n}\,|n\rangle = n\,|n\rangle\,. \tag{2.42}$$

The effect of the operators $\hat{a}^\dagger$ and $\hat{a}$ on a number state is, to create or to annihilate a photon with the energy $\hbar\omega$ ([14], p. 65):

$$\hat{a}^\dagger\,|n\rangle = \sqrt{n+1}\,|n+1\rangle \tag{2.43}$$

$$\hat{a}\,|n\rangle = \sqrt{n}\,|n-1\rangle\,. \tag{2.44}$$

The application of the annihilation operator $\hat{a}$ also defines the ground state of the electric field by means of ([14], p. 64)

$$\hat{a}\,|0\rangle = 0. \tag{2.45}$$

The number states can be created from the ground state $|0\rangle$ by the consecutive use of the creation operator $\hat{a}^\dagger$ ([14], p. 65):

$$|n\rangle = \frac{(\hat{a}^\dagger)^n}{\sqrt{n!}}\,|0\rangle\,,\ n = 0, 1, 2... \tag{2.46}$$

The variance of the amplitude and phase quadrature of a number state is identical in both quadratures ([89], p. 44)

$$\begin{aligned}(\Delta\hat{X}_1)_n^2 &= \langle n|\,\hat{X}_1^2\,|n\rangle - \langle n|\,\hat{X}_1\,|n\rangle^2 \\ &= \langle n|\,(\hat{a}^\dagger + \hat{a})^2\,|n\rangle - \langle n|\,(\hat{a}^\dagger + \hat{a})\,|n\rangle^2 \\ &= \langle n|\,(\hat{a}^\dagger\hat{a}^\dagger + 2\hat{a}^\dagger\hat{a} + 1 + \hat{a}\hat{a})\,|n\rangle - \langle n|\,(\hat{a}^\dagger + \hat{a})\,|n\rangle^2 \\ &= 2n + 1 = (\Delta\hat{X}_2)_n^2\end{aligned} \tag{2.47}$$

and is minimized by the vacuum state $|0\rangle$ to

$$(\Delta\hat{X}_1)_0^2 = (\Delta\hat{X}_2)_0^2 = 1. \tag{2.48}$$

The fact that the vacuum state $|0\rangle$ does not contain any photons can be seen by calculating the expectation value of the vacuum state for the number operator as well as its variance, which both vanish ([22], p. 17):

$$\langle\hat{n}\rangle = \langle 0|\,\hat{n}\,|0\rangle = 0 \tag{2.49}$$

$$(\Delta\hat{n})_0^2 = \langle 0|\,\hat{n}^2\,|0\rangle - \langle 0|\,\hat{n}\,|0\rangle^2 = 0. \tag{2.50}$$

Even in the absence of any photons, the vacuum state of a single mode of the electric field exhibits equal fluctuations in both quadratures, characterized by the standard deviation

$$(\Delta\hat{X}_1)_0 = (\Delta\hat{X}_2)_0 = 1. \tag{2.51}$$

The origin of these zero point fluctuations is the non-vanishing zero point energy $\hbar\omega/2$ of the harmonic oscillator that describes the corresponding mode (see equation (2.41)). These

zero point fluctuations of the electric field are also named shot noise or vacuum noise. The eigenvalue equations of the quadrature operators $\hat{X}_1$ and $\hat{X}_2$ are defined as ([14], p. 69)

$$\hat{X}_1 |x_1\rangle = x_1 |x_1\rangle \tag{2.52}$$

and

$$\hat{X}_2 |x_2\rangle = x_2 |x_2\rangle , \tag{2.53}$$

where x_1 and x_2 are the eigenvalues. The result of measuring a certain value x_1 if a measurement on the observable $\hat{X}_1$ is carried out is given by the probability distribution ([14], p. 71)

$$P_0 (x_1) = |\langle x_1|0\rangle|^2 = \frac{1}{\sqrt{\pi}} \exp (- x_1^2), \tag{2.54}$$

where equation (2.52) has been used. A similar result is obtained for the $\hat{X}_2$ quadrature with equation (2.53)

$$P_0 (x_2) = |\langle x_2|0\rangle|^2 = \frac{1}{\sqrt{\pi}} \exp (- x_2^2). \tag{2.55}$$

For the vacuum state $|0\rangle$, the probability distributions in amplitude and phase quadrature are both given by a Gaussian distribution with a standard deviation of 1. In the two-dimensional phase space, which is formed by the amplitude quadrature $\hat{X}_1$ and the phase quadrature $\hat{X}_2$, the uncertainty area of the vacuum state is depicted by a circle with a radius of 1 which corresponds to the standard deviation ([27], p. 37), as shown in figure 2.5. The dark red colour in the center of the circle emphasizes that the probability distribution is larger at the origin, than further outside in radial direction. This circular uncertainty area is the projection of the contour line of a wigner function onto the plane, formed by $\hat{X}_1$ and $\hat{X}_2$ ([14], pp. 238 – 240).

2.3.4 Coherent states

Coherent states of light are used to represent a large number of photons in an optical mode. Thus, their phase can be calculated accurately. They are the preferred states to describe the light of a stabilized laser that doesn't exhibit technical laser noise at frequencies above its relaxation oscillation. A coherent state can be expressed in terms of the number states $|n\rangle$ and is obtained by the application of the displacement operator ([89], p. 12)

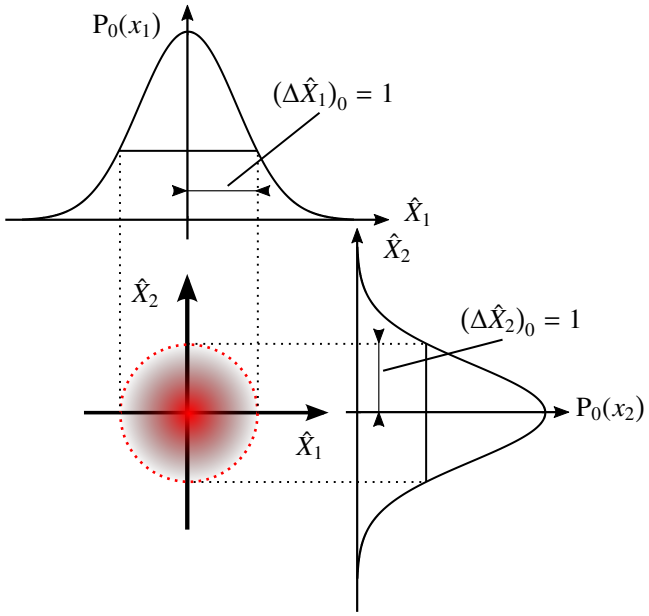

Figure 2.5: Phase space representation of the vacuum state. In the phase space that is formed by the amplitude quadrature $\hat{X}_1$ and the phase quadrature $\hat{X}_2$, the uncertainty of the quadrature values for the vacuum state $|0\rangle$ is depicted as a circle centered at the origin. The radius of the circle is the standard deviation $(\Delta\hat{X}_1)_0 = (\Delta\hat{X}_2)_0 = 1$ of the Gaussian probability distributions $P_0(x_1)$ and $P_0(x_2)$. Adapted from ([57], p. 9).

$$\begin{aligned} D(\alpha) &= \exp\left(\alpha\hat{a}^\dagger - \alpha^*\hat{a}\right) \\ &= \exp\left(-\frac{1}{2}|\alpha|^2 + \alpha\hat{a}^\dagger - \alpha^*\hat{a}\right) \end{aligned} \tag{2.56}$$

on the vacuum state $|0\rangle$, leading to

$$\begin{aligned} |\alpha\rangle &= D(\alpha)\,|0\rangle \\ &= \exp\left(-\frac{1}{2}|\alpha|^2\right)\sum_{n=0}^{\infty}\frac{\alpha^n}{\sqrt{n!}}\,|n\rangle\,. \end{aligned} \tag{2.57}$$

Here,

$$\alpha = |\alpha|e^{i\phi} \tag{2.58}$$

is a complex amplitude ([37], p. 45).

Coherent states are also defined as eigenstates of the annihilation operator $\hat{a}$, satisfying the eigenvalue equations ([90], p. 40)

$$\hat{a}\,|\alpha\rangle = \alpha\,|\alpha\rangle \tag{2.59}$$

and

$$\langle\alpha|\,\hat{a}^\dagger = \langle\alpha|\,\alpha^*. \tag{2.60}$$

The expectation values of the quadrature operators $\hat{X}_1$ and $\hat{X}_2$ for a coherent state are proportional to the real and imaginary part of the electric field, as already mentioned in section 2.3.2 ([90], p. 42)

$$\langle\hat{X}_1\rangle_\alpha = \langle\alpha|\,\hat{X}_1\,|\alpha\rangle = \langle\alpha|\,(\hat{a}+\hat{a}^\dagger)\,|\alpha\rangle = \alpha+\alpha^* = 2\,\mathrm{Re}\{\alpha\} \tag{2.61}$$

$$\langle\hat{X}_2\rangle_\alpha = \langle\alpha|\,\hat{X}_2\,|\alpha\rangle = \mathrm{i}\,\langle\alpha|\,(\hat{a}^\dagger-\hat{a})\,|\alpha\rangle = \mathrm{i}(\alpha^*-\alpha) = 2\,\mathrm{Im}\{\alpha\}. \tag{2.62}$$

The variance of the amplitude quadrature of a coherent state is ([90], p. 44)

$$\begin{aligned}
(\Delta\hat{X}_1)^2_\alpha &= \langle\alpha|\,\hat{X}_1^2\,|\alpha\rangle - \langle\alpha|\,\hat{X}_1\,|\alpha\rangle^2 \\
&= \langle\alpha|\,(\hat{a}^\dagger+\hat{a})^2\,|\alpha\rangle - \langle\alpha|\,(\hat{a}^\dagger+\hat{a})\,|\alpha\rangle^2 \\
&= \langle\alpha|\,(\hat{a}^\dagger\hat{a}^\dagger + 2\hat{a}^\dagger\hat{a} + 1 + \hat{a}\hat{a})\,|\alpha\rangle - \langle\alpha|\,(\hat{a}^\dagger+\hat{a})\,|\alpha\rangle^2 \\
&= \alpha^{*2} + \alpha^2 + 2|\alpha|^2 + 1 - \alpha^{*2} - \alpha^2 - 2|\alpha|^2 \\
&= 1.
\end{aligned} \tag{2.63}$$

An identical result is obtained for the phase quadrature $\hat{X}_2$

$$(\Delta\hat{X}_2)^2_\alpha = \langle\alpha|\,\hat{X}_2^2\,|\alpha\rangle - \langle\alpha|\,\hat{X}_2\,|\alpha\rangle^2 = 1. \tag{2.64}$$

Hence, the standard deviations are

$$(\Delta\hat{X}_1)_\alpha = 1 \tag{2.65}$$

and

$$(\Delta\hat{X}_2)_\alpha = 1. \tag{2.66}$$

Similar to the vacuum state $|0\rangle$, the coherent state is a quantum state with minimum uncertainty in both quadratures. As shown in figure 2.6, for a certain point in space and time, the coherent state $|\alpha\rangle$ can be depicted in phase space by a vector of the length $|\alpha| = 1/2\sqrt{\langle\hat{X}_1\rangle^2_\alpha + \langle\hat{X}_2\rangle^2_\alpha}$ ([90], p. 42). The vector, also called phasor, starts at the origin of the coordinate system and ends at a point (x_1, x_2) in phase space. On top, the phasor displays a circular uncertainty area with radius of 1, describing the Gaussian noise in amplitude and phase.

Measuring the power of a laser is equivalent to the detection of the photon number n of a

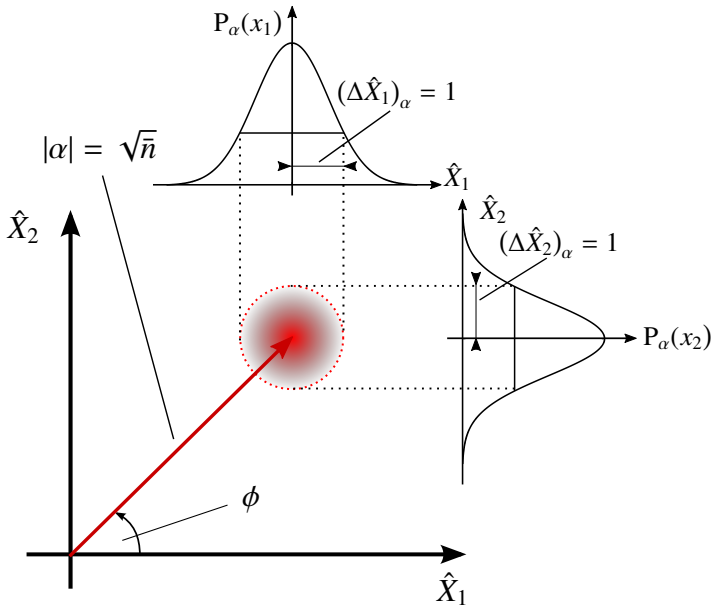

Figure 2.6: Phase space representation of a coherent state. A coherent state is illustrated as a vacuum state that is displaced by a phasor with the amplitude $|\alpha| = \sqrt{\bar{n}}$ and rotated by the phase angle ϕ. On its top, the phasor shows the same Gaussian noise with a standard deviation of $(\Delta\hat{X}_1)_\alpha = (\Delta\hat{X}_2)_\alpha = 1$ in amplitude and phase quadrature, as the vacuum state $|0\rangle$. The length of the phasor $|\alpha| = \sqrt{\bar{n}}$ corresponds to the square root of the mean photon number. Adapted from ([14], p. 73) and ([90], p. 42).

coherent state in a certain time interval τ. In this time interval, the photons arrive randomly at the detector, resulting in a fluctuating photo-current. The average photon number of a coherent state can be calculated as ([89], p. 13)

$$\begin{aligned}\bar{n} &= \langle\alpha|\,\hat{n}\,|\alpha\rangle \\ &= \langle\alpha|\,\hat{a}^\dagger\hat{a}\,|\alpha\rangle \\ &= \alpha^*\alpha\,\langle\alpha|\alpha\rangle \\ &= |\alpha|^2. \end{aligned} \tag{2.67}$$

The fluctuation of photon number in the time interval τ follows a Poisson distribution which is obtained by computing the probability of measuring n photons ([89], p. 13)

$$
\begin{aligned}
P_\alpha(n) &= |\langle n|\alpha\rangle|^2 \\
&= \left|\exp\left(-\frac{1}{2}|\alpha|^2\right)\sum_{k=0}^{\infty}\frac{\alpha^k}{\sqrt{k!}}\langle n|k\rangle\right|^2 \\
&= \left|\exp\left(-\frac{1}{2}|\alpha|^2\right)\frac{\alpha^n}{\sqrt{n!}}\right|^2 \\
&= \exp\left(-|\alpha|^2\right)\frac{|\alpha|^{2n}}{n!} \\
&= \exp\left(-\bar{n}^2\right)\frac{\bar{n}^n}{n!}.
\end{aligned} \tag{2.68}
$$

The quadratic fluctuation of the average photon number $\bar{n}$ of a coherent state is given by the variance ([90], p. 41)

$$
\begin{aligned}
(\Delta\hat{n})_\alpha^2 &= \langle\alpha|\,\hat{n}^2\,|\alpha\rangle - \langle\alpha|\,\hat{n}\,|\alpha\rangle^2 \\
&= \langle\alpha|\,(\hat{a}^\dagger\hat{a})^2\,|\alpha\rangle - \langle\alpha|\,\hat{a}^\dagger\hat{a}\,|\alpha\rangle^2 \\
&= |\alpha|^4 + |\alpha|^2 - |\alpha|^4 = |\alpha|^2 \\
&= \bar{n}.
\end{aligned} \tag{2.69}
$$

Thus, the standard deviation is the square of the mean photon number

$$
\Delta\hat{n} = \pm\sqrt{\bar{n}}. \tag{2.70}
$$

This is the characteristic feature of a Poisson distribution. Figure 2.7 illustrates the photon number distributions $P_\alpha(n)$ for two coherent states with the average photon numbers of $\bar{n} = 3$ and $\bar{n} = 6000$. For the latter, the Poisson distribution can be approximated with a Gaussian function.

2.3.5 The squeezed vacuum

In the last two sections, states of light as the vacuum state or the coherent state were presented, that exhibit the minimum uncertainty $\Delta\hat{X}_1 = \Delta\hat{X}_2 = 1$ in both, amplitude and phase quadrature. Thus, they obey the Heisenberg uncertainty relation $\Delta\hat{X}_1\Delta\hat{X}_2 \geq 1$. In this section, the so called squeezed states are introduced. These states show in one quadrature a noise, that is below the vacuum noise. To still fulfill Heisenberg's uncertainty relation, the opposite quadrature then exhibits quantum fluctuations above the vacuum noise.
Squeezed states of light are created by the squeezing operator ([14], p. 242)

$$
\hat{S}(r,\theta) = \exp\left[\frac{1}{2}\left(r\mathrm{e}^{-2\mathrm{i}\theta}\hat{a}^2 - r\mathrm{e}^{2\mathrm{i}\theta}\hat{a}^{\dagger 2}\right)\right]. \tag{2.71}
$$

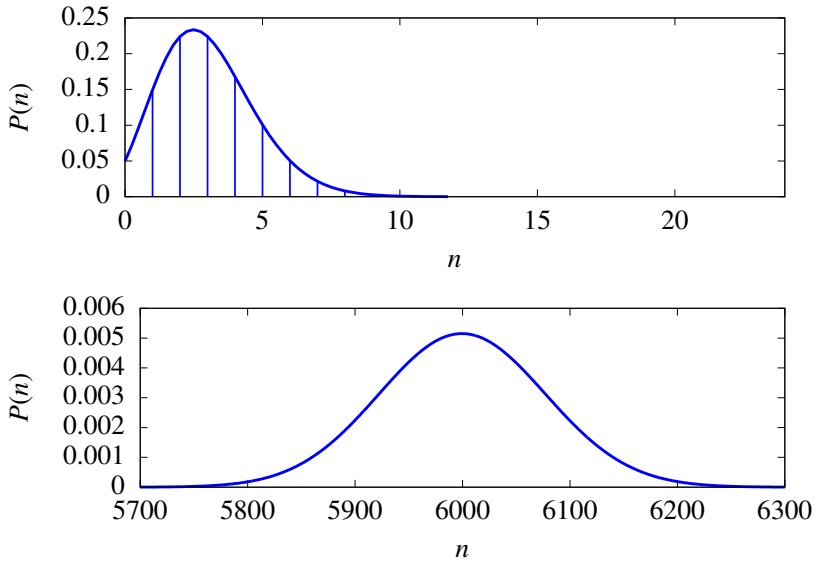

Figure 2.7: Simulated photon number distribution $P_\alpha(n)$ for a coherent state. The upper graph shows a photon number distribution for a mean photon number of $\bar{n} = 3$. The lower graph depicts a photon number distribution for $\bar{n} = 6000$. Here, the distribution is almost Gaussian.

Here, r is the squeezing parameter that determines the strength of the squeezing and θ is the squeezing angle, that defines the quadrature in which the squeezing is generated. Since $\hat{S}(r,\theta)$ contains the square of $\hat{a}$ and $\hat{a}^\dagger$, it annihilates and creates photons pairwise. It also fulfills the relations ([14], p. 242)

$$\hat{S}^\dagger(r,\theta)\,\hat{a}\hat{S}(r,\theta) = \hat{a}\cosh(r) - \hat{a}^\dagger e^{-2i\theta}\sinh(r) \tag{2.72}$$

$$\hat{S}^\dagger(r,\theta)\,\hat{a}^\dagger\hat{S}(r,\theta) = \hat{a}^\dagger\cosh(r) - \hat{a}e^{2i\theta}\sinh(r)\,, \tag{2.73}$$

with $\hat{S}^\dagger(r,\theta) = \hat{S}^{-1}(r,\theta)$. The squeezed vacuum state is generated by applying the squeezing operator on the vacuum state ([37], p. 153)

$$|\xi\rangle = \hat{S}(r,\theta)\,|0\rangle\,. \tag{2.74}$$

The fluctuations of the $\hat{X}_1$ quadrature of the squeezed vacuum state are given by its variance ([37], p. 153)

$$
\begin{aligned}
(\Delta\hat{X}_1)_\xi^2 &= \langle 0|\,\hat{S}^\dagger(r,\theta)\,\hat{X}_1^2\hat{S}\,(r,\theta)\,|0\rangle - \langle 0|\,\hat{S}^\dagger(r,\theta)\,\hat{X}_1\hat{S}\,(r,\theta)\,|0\rangle^2 \\
&= \langle 0|\,\hat{S}^\dagger(r,\theta))\left(\hat{a}+\hat{a}^\dagger\right)^2\hat{S}\,(r,\theta)\,|0\rangle - \langle 0|\,\hat{S}^\dagger(r,\theta)\left(\hat{a}+\hat{a}^\dagger\right)\hat{S}\,(r,\theta)\,|0\rangle^2 \\
&= \cosh^2(r) + \sinh^2(r) - 2\sinh(r)\cosh(r)\cos(\theta)\,. \qquad (2.75)
\end{aligned}
$$

Please note that this result differs by a factor of $1/4$ to the one shown in [37]. This is due to the different normalization of the vacuum. For the computation of equation (2.75) the relations ([14], p. 242)

$$
\begin{aligned}
\langle 0|\,\hat{S}^\dagger(r,\theta)\,\hat{a}^2\hat{S}\,(r,\theta)\,|0\rangle &= -\exp(-2\mathrm{i}\theta)\cosh(r)\sinh(r) \\
\langle 0|\,\hat{S}^\dagger(r,\theta)\,\hat{a}\hat{a}^\dagger\hat{S}\,(r,\theta)\,|0\rangle &= \cosh^2(r) \\
\langle 0|\,\hat{S}^\dagger(r,\theta)\,\hat{a}^\dagger\hat{a}\hat{S}\,(r,\theta)\,|0\rangle &= \sinh^2(r) \\
\langle 0|\,\hat{S}^\dagger(r,\theta)\,\hat{a}^{\dagger 2}\hat{S}\,(r,\theta)\,|0\rangle &= -\exp(2\mathrm{i}\theta)\cosh(r)\sinh(r)
\end{aligned} \qquad (2.76)
$$

have been used. A similar calculation yields for the variance of the phase quadrature

$$
(\Delta\hat{X}_2)_\xi^2 = \cosh^2(r) + \sinh^2(r) + 2\sinh(r)\cosh(r)\cos(2\theta)\,. \qquad (2.77)
$$

With a squeezing angle of $\theta = 0°$, equations (2.75) and (2.77) become ([14], p. 243)

$$
(\Delta\hat{X}_1)_\xi^2 = \exp(-2r) \qquad (2.78)
$$

$$
(\Delta\hat{X}_2)_\xi^2 = \exp(2r)\,. \qquad (2.79)
$$

Thus, the quantum fluctuations in both quadratures, given by the standard deviations, are

$$
(\Delta\hat{X}_1)_\xi = \exp(-r) \qquad (2.80)
$$

$$
(\Delta\hat{X}_2)_\xi = \exp(r)\,. \qquad (2.81)
$$

As depicted in figure 2.8, this result shows that the quantum noise in the amplitude quadrature $(\Delta\hat{X}_1)_\xi$ drops below the vacuum fluctuations of $(\Delta\hat{X}_1)_0 = (\Delta\hat{X}_2)_0 = 1$, the noise gets squeezed. Simultaneously, the fluctuations of the phase quadrature $(\Delta\hat{X}_2)_\xi$ are larger than the vacuum fluctuations, they get anti-squeezed. The product of the standard deviations is

$$
(\Delta\hat{X}_1)_\xi(\Delta\hat{X}_2)_\xi = 1. \qquad (2.82)
$$

Thus, Heisenberg's uncertainty relation is satisfied.

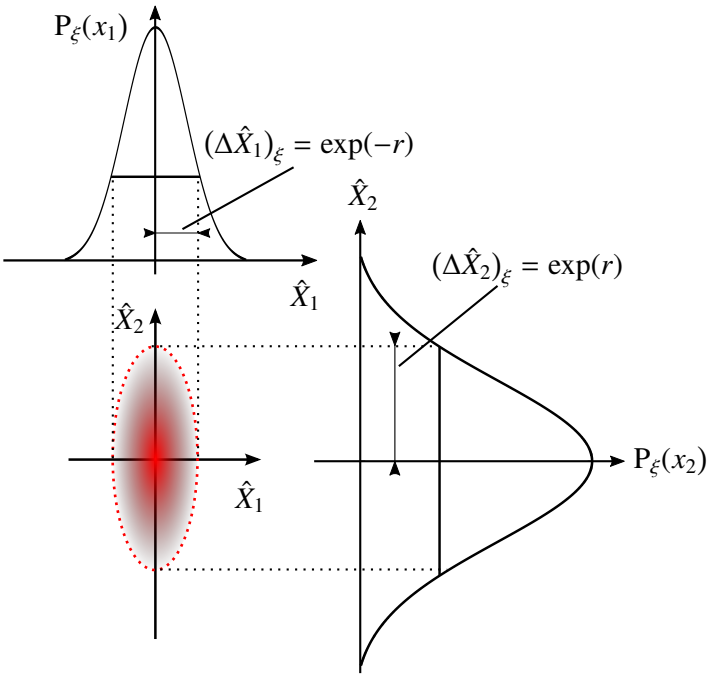

Figure 2.8: Phase space representation of an amplitude squeezed vacuum state. The quantum noise in direction of $\hat{X}_1$, characterized by the standard deviation $(\Delta\hat{X}_1)_\xi = \exp(-r)$ of the probability distribution $P_\xi(x_1)$, is reduced below the vacuum uncertainty of $(\Delta\hat{X}_1)_0 = 1$. Simultaneously, the quantum noise of the phase quadrature, described by the standard deviation $(\Delta\hat{X}_2)_\xi = \exp(r)$, is increased above the quantum noise of the vacuum state. The magnitude r which characterizes the squeezing strength, is called squeezing parameter. Adapted from ([37], p. 154).

The photon number $\bar{n}$ of a squeezed vacuum state is obtained by computing the expectation value of the squeezed vacuum state with the number operator $\hat{n}$ ([14], p. 245)

$$\begin{aligned}\bar{n} = \langle\hat{n}\rangle_\xi &= \langle 0|\,\hat{S}^\dagger(r,\theta)\,\hat{n}\hat{S}\,(r,\theta)\,|0\rangle \\ &= \langle 0|\,\hat{S}^\dagger(r,\theta)\,\hat{a}^\dagger\hat{a}\hat{S}\,(r,\theta)\,|0\rangle \\ &= \sinh^2(r) > 0. \end{aligned} \tag{2.83}$$

Thus, the squeezed vacuum state contains photons which show quantum correlations. The energy of the squeezed vacuum is obtained with the Hamiltonian of the quantized harmonic oscillator, given by equation (2.38) ([52], p. 34)

$$\begin{aligned}\langle\hat{H}\rangle_\xi &= \langle 0|\,\hat{S}^\dagger(r,\theta)\,\hbar\omega(\hat{n}+1/2)\hat{S}\,(r,\theta)\,|0\rangle \\ &= \hbar\omega\left(\frac{1}{2}+\sinh^2(r)\right). \end{aligned} \tag{2.84}$$

This result shows that the energy of the squeezed vacuum is larger than the energy of the ground state, given by equation (2.41).
Because the squeezing operator (2.71) only creates and annihilates photons pairwise, the probability of measuring an odd number of photons vanishes. The probability for a squeezed vacuum state of measuring $2n$ photons is given by ([37], p. 161)

$$P_\xi(2n) = |\langle 2n|\xi\rangle|^2 = \frac{(2n)!}{2^{2n}\,(n!)^2}\frac{(\tanh(r))^{2n}}{\cosh(r)}. \tag{2.85}$$

An example of a photon number distribution, simulated for a 10 dB squeezed vacuum state is shown in figure 2.9. Only even numbers of photons can be measured.

2.3.6 Kerr Squeezed quadrature states

Another tool for the generation of squeezed states is the optical Kerr effect. If a coherent state is transmitted through a Kerr medium of length L, the noise in its quadratures gets rearranged by the intensity-dependent phase shift, that was introduced in section (2.2.1). The Kerr effect is described by the Hamilton operator ([89], p. 88)

$$\hat{H}_K = \frac{\hbar}{2}\chi\hat{a}^{\dagger 2}\hat{a}^2. \tag{2.86}$$

The factor χ is defined as ([65], p. 29)

$$\chi = \frac{3\hbar\omega_0^2}{2V\epsilon_0^2 n_0^4}\chi^{(3)} = \frac{3\hbar\omega_0^2}{2AL\epsilon_0^2 n_0^4}\chi^{(3)}. \tag{2.87}$$

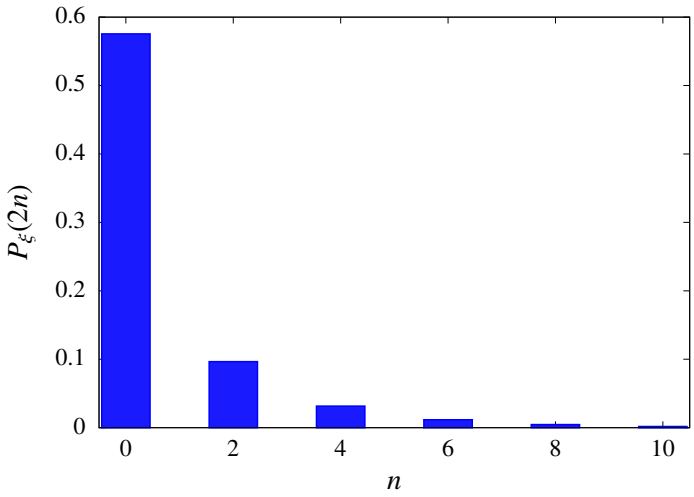

Figure 2.9: Simulated photon number distribution for a 10 dB squeezed vacuum state. Because the squeezing operator creates and annihilates photons pairwise, the probability of measuring odd photon numbers vanishes. Only even numbers of photons can be detected.

Here $\hbar$ is the reduced Planck constant, ω_0 the carrier frequency, ϵ_0 the vacuum permittivity, n_0 the linear refractive index and $\chi^{(3)}$ the third-order nonlinear susceptibility. $V = AL$ is the interaction volume. In the experiment, $A = \pi w_0^2$ is the cross section of the Gaussian beam inside of the nonlinear medium of the length L and w_0 is its waist ([83], p. 134).
To study the effect of a Kerr medium on the quadrature noise of a coherent state, first the time evolution of the annihilation operator $\hat{a}$ has to be calculated by solving Heisenberg's equation ([65], p. 47)

$$i\hbar\frac{d}{dt}\hat{a} = -\left[\hat{H}_K, \hat{a}\right] = \hbar\chi\hat{a}^\dagger\hat{a}\hat{a} = \hbar\chi\hat{n}\hat{a}. \tag{2.88}$$

Since the photon number operator $\hat{n}$ is a constant of motion ([65], p. 29)

$$[\hat{n}, \hat{H}_\mathrm{K}] = 0, \tag{2.89}$$

equation (2.88) is solved by

$$\hat{a}\,(t) = \exp\left(-\mathrm{i}\chi\hat{n}t\right)\hat{a}\,(0) = \exp\left(-\mathrm{i}\chi\hat{n}t\right)\hat{a}, \tag{2.90}$$

where t is the time. In the last step, $\hat{a}\,(0)$ was replaced by $\hat{a}$ since it has the same effect as the annihilation operator introduced in equation (2.59). Now let's assume a coherent state $|\alpha\rangle$ with a real amplitude α as initial state. After the interaction time t, the effect of the Kerr medium on the coherent state is given by the average amplitude of the coherent state ([89], p. 88)

$$\begin{aligned}\langle \hat{a}\,(t)\rangle &= \langle \alpha |\, \hat{a}\,(t)\, |\alpha\rangle \\ &= \alpha \exp\left[-\alpha^2\left(1-\exp\left(-\mathrm{i}\theta_K\right)\right)\right] \\ &= \alpha \exp\left[-\alpha^2\left(1-\cos\left(\theta_K\right)\right) - \mathrm{i}\alpha^2 \sin\left(\theta_K\right)\right], \end{aligned} \tag{2.91}$$

where the interaction parameter

$$\theta_K = \chi t \tag{2.92}$$

was used. Since $\chi \propto \chi^{(3)}$ is typically very small due to the third order nonlinearity and thus, $\theta_k \ll 1$, the sine and cosine functions in equation (2.91) can be replaced by their first order Taylor series and thus, the average amplitude of the coherent state can be approximated as ([89], p. 88)

$$\langle \hat{a}\,(\theta_K)\rangle \approx \alpha \exp\left(-\mathrm{i}\alpha^2\theta_K - \frac{\alpha^2\theta_K^2}{2}\right). \tag{2.93}$$

The first therm $\alpha^2\theta_K$ in the exponential expression causes a rotation of the average amplitude of the coherent state that depends on the light power $P = \alpha^2$. The second therm, $\alpha^2\theta_k^2/2 = \alpha^2\chi^2t^2/2$, leads to a decay of the amplitude that evolves with the square of the time t. However, for small interaction times or if the nonlinear Kerr medium is inside of an optical resonator, the second term can be neglected.

The effect of a Kerr medium on a coherent input state exhibiting vacuum noise in amplitude and phase quadrature, is shown in figure 2.10. The top of the blue phasor represents the point of the highest intensity of the noise circle and the top of the green phasor corresponds to the point with the lowest intensity. Due to the intensity-dependent refractive index, the point corresponding to the top of the blue phasor changes the refractive index more, than the point corresponding to the top of the green phasor. Consequently, the blue phasor receives the largest phase rotation and the green phasor the smallest. Because the optical Kerr effect acts on all points of the circular quantum noise distribution, all points experience an intensity-dependent phase shift. Thus, the initial circular noise distribution is transformed into an ellipse. The quantum noise gets squeezed in a certain quadrature $\hat{Y}_1$ and anti-squeezed in the orthogonal quadrature $\hat{Y}_2$. To calculate the non-classical noise transformation of the Kerr effect, the rotated quadrature operators [91]

$$\hat{Y}_1(\theta_K) = \hat{a}\,(\theta_K) + \hat{a}^\dagger\,(\theta_K) = \hat{a}\exp\left(-i\theta_K\hat{n}\right) + \hat{a}^\dagger \exp\left(i\theta_K\hat{n}\right) \tag{2.94}$$

and

$$\hat{Y}_2(\theta_K) = -\mathrm{i}\left(\hat{a}\,(\theta_K) - \hat{a}^\dagger\,(\theta_K)\right) = \mathrm{i}\left(\hat{a}^\dagger \exp\left(i\theta_K\hat{n}\right) - \hat{a}\exp\left(-i\theta_K\hat{n}\right)\right) \tag{2.95}$$

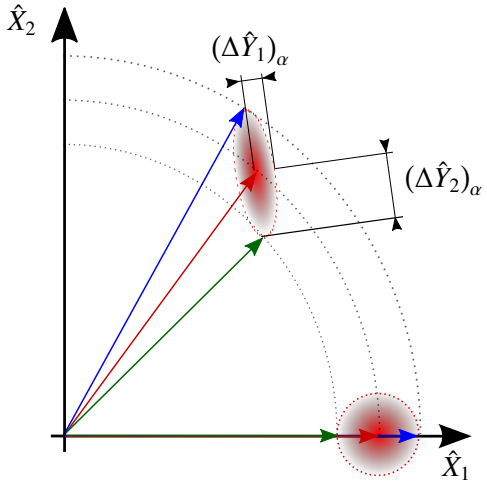

Figure 2.10: Generation of squeezing by means of the optical Kerr effect. In the initial coherent state with a circular noise distribution, the point represented by the top of the blue phasor corresponds to the largest intensity while the point described by the top of the green phasor has the lowest intensity. Due to the intensity-dependent refractive index of the Kerr medium, the point corresponding to the top of the blue phasor modulates the refractive index more than the top of the green phasor. The intensity-dependent phase shift acts on all points of the circular quantum noise distribution and transforms it into an ellipse. Thus, the fluctuations $(\Delta\hat{Y}_1^2)_\alpha$ in a certain rotated quadrature $\hat{Y}_1$ are smaller than the vacuum noise and a squeezed state is generated. Adapted from [91].

are defined.

To obtain the variances of the rotated quadrature operators, the magnitudes $\langle\alpha|\,\hat{Y}_i\,(\theta_K)^2\,|\alpha\rangle$ and $\langle\alpha|\,\hat{Y}_i\,(\theta_K)\,|\alpha\rangle^2$ need to be computed ([65], pp. 51 – 53):

$$\begin{aligned}\langle\alpha|\,\hat{Y}_1\,(\theta_K)\,|\alpha\rangle^2 &= \langle\alpha|\,\hat{a}\,(\theta_K) + \hat{a}^\dagger\,(\theta_K)\,|\alpha\rangle^2 \\ &= \alpha^2\left(\exp\left[-\alpha^2\left(1-\exp\left(-\mathrm{i}\theta_K\right)\right)\right] + \exp\left[-\alpha^2\left(1-\exp\left(\mathrm{i}\theta_K\right)\right)\right]\right)^2 \\ &= 2\alpha^2\exp\left[2\alpha^2\left(\cos\left(\theta_K\right)-1\right)\right]\left[\cos\left(2\alpha^2\sin\left(\theta_K\right)\right)+1\right] \end{aligned} \tag{2.96}$$

$$\begin{aligned}\langle\alpha|\,\hat{Y}_1^2\,(\theta_K)\,|\alpha\rangle &= \langle\alpha|\left(\hat{a}\,(\theta_K) + \hat{a}^\dagger\,(\theta_K)\right)^2|\alpha\rangle \\ &= \alpha^2\Big(\exp\left(-\mathrm{i}\theta_K\right)\exp\left[-\alpha^2\left(1-\exp\left(-2\mathrm{i}\theta_K\right)\right)\right] \\ &\qquad + \exp\left(\mathrm{i}\theta_K\right)\exp\left[-\alpha^2\left(1-\exp\left(2\mathrm{i}\theta_K\right)\right)\right]\Big)^2 \\ &= 2\alpha^2\exp\left[\alpha^2\left(2\cos\left(\theta_K\right)-1\right)\right]\cos\left[\alpha^2\sin\left(2\theta_K\right)+\theta_K\right] + 2\alpha^2 + 1 \end{aligned} \tag{2.97}$$

$$\begin{aligned}\langle\alpha|\,\hat{Y}_2(\theta_K)\,|\alpha\rangle^2 &= \mathrm{i}^2\,\langle\alpha|\,\hat{a}^\dagger(\theta_K)-\hat{a}(\theta_K)\,|\alpha\rangle^2\\ &= -\alpha^2\left(\exp\left[-\alpha^2\left(1-\exp\left(-\mathrm{i}\theta_K\right)\right)\right]-\exp\left[-\alpha^2\left(1-\exp\left(\mathrm{i}\theta_K\right)\right)\right]\right)^2\\ &= -2\alpha^2\exp\left[2\alpha^2\left(\cos\left(\theta_K\right)-1\right)\right]\left[\cos\left(2\alpha^2\sin\left(\theta_K\right)\right)-1\right] \qquad (2.98)\end{aligned}$$

$$\begin{aligned}\langle\alpha|\,\hat{Y}_2^2(\theta_K)\,|\alpha\rangle &= \langle\alpha|\left(\hat{a}(\theta_K)+\hat{a}^\dagger(\theta_K)\right)^2|\alpha\rangle\\ &= \alpha^2\Big(\exp\left(-\mathrm{i}\theta_K\right)\exp\left[-\alpha^2\left(1-\exp\left(-2\mathrm{i}\theta_K\right)\right)\right]\\ &\qquad +\exp\left(\mathrm{i}\theta_K\right)\exp\left[-\alpha^2\left(1-\exp\left(2\mathrm{i}\theta_K\right)\right)\right]\Big)^2\\ &= -2\alpha^2\exp\left[\alpha^2\left(\cos\left(2\theta_K\right)-1\right)\right]\cos\left[\alpha^2\sin\left(2\theta_K\right)+\theta_K\right]+2\alpha^2+1. \qquad (2.99)\end{aligned}$$

Consequently, the variances of the quadrature operators are ([65], p. 53)

$$\begin{aligned}\left(\Delta\hat{Y}_1^2\right)_\alpha &= \langle\alpha|\,\hat{Y}_1^2(\theta_K)\,|\alpha\rangle-\langle\alpha|\,\hat{Y}_1(\theta_K)\,|\alpha\rangle^2\\ &= 1+2\alpha^2[\exp\left(\alpha^2\left[\cos\left(2\theta_K\right)-1\right]\right)\cos\left[\alpha^2\sin\left(2\theta_K\right)+\theta_K\right]\\ &\qquad -\exp\left(2\alpha^2\left[\cos\left(\theta_K\right)-1\right]\right)\left(1+\cos\left(2\alpha^2\sin\left(\theta_K\right)\right)\right)+1] \qquad (2.100)\end{aligned}$$

and

$$\begin{aligned}\left(\Delta\hat{Y}_2^2\right)_\alpha &= \langle\alpha|\,\hat{Y}_2^2(\theta_K)\,|\alpha\rangle-\langle\alpha|\,\hat{Y}_2(\theta_K)\,|\alpha\rangle^2\\ &= 1+2\alpha^2[-\exp\left(\alpha^2\left[\cos\left(2\theta_K\right)-1\right]\right)\cos\left[\alpha^2\sin\left(2\theta_K\right)+\theta_K\right]\\ &\qquad -\exp\left(2\alpha^2\left[\cos\left(\theta_K\right)-1\right]\right)\left(1-\cos\left(2\alpha^2\sin\left(\theta_K\right)\right)\right)+1]. \qquad (2.101)\end{aligned}$$

$\left(\Delta\hat{Y}_1^2\right)_\alpha$ and $\left(\Delta\hat{Y}_2^2\right)_\alpha$ are shown in figure 2.11 for $\chi = 1$ and $\alpha^2 = 16$. For small values of θ_K, the fluctuations of the $\hat{Y}_1$ quadrature are below the vacuum noise level while the noise of the $\hat{Y}_2$ quadrature gets anti-squeezed. In a realistic experimental setup, $\chi \ll 1$ will be very small and thus, a very high light power and long interaction times t would be required in order to achieve small values of $\theta_K = \chi t$. To solve this problem, the cascaded optical Kerr effect instead of the third-order optical Kerr effect can be used. Consequently, χ will be proportional to the second-order susceptibility $\chi^{(2)}$ which is about two orders of magnitude larger, than $\chi^{(3)}$ ([83], p. 134). Therefore, the cascaded Kerr effect (see section 2.2.2) provides the possibility of squeezed light generation in the continuous-wave laser regime.

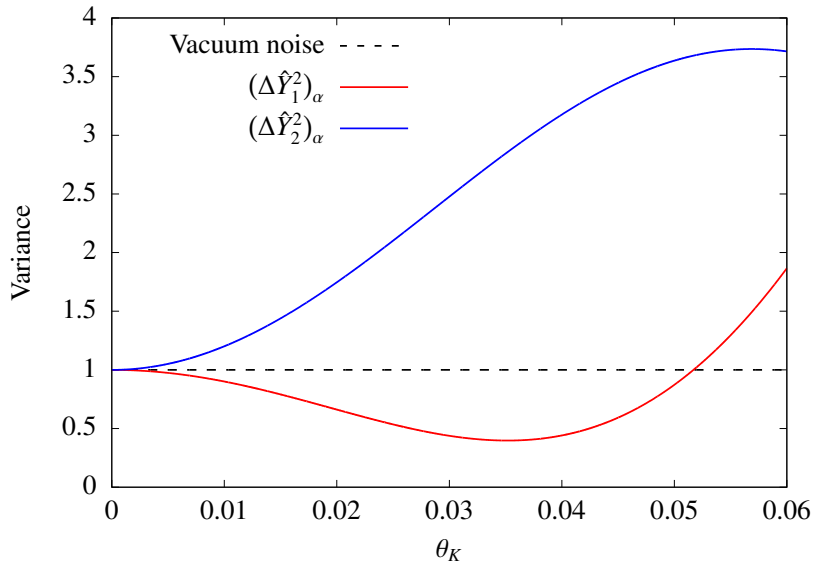

Figure 2.11: Simulation of the squeezed and anti-squeezed variance $(\Delta\hat{Y}_1^2)_\alpha$ and $(\Delta\hat{Y}_2^2)_\alpha$ as a function of the interaction parameter $\theta_K = \chi t$. The variance of the rotated quadrature $\hat{Y}_1$ drops below the vacuum noise level (black dashed line) while the opposite quadrature $\hat{Y}_2$ shows anti-squeezing. For this plot, an initial coherent state with an amplitude of $\alpha = 4$ and a constant $\chi = 1$ was assumed.

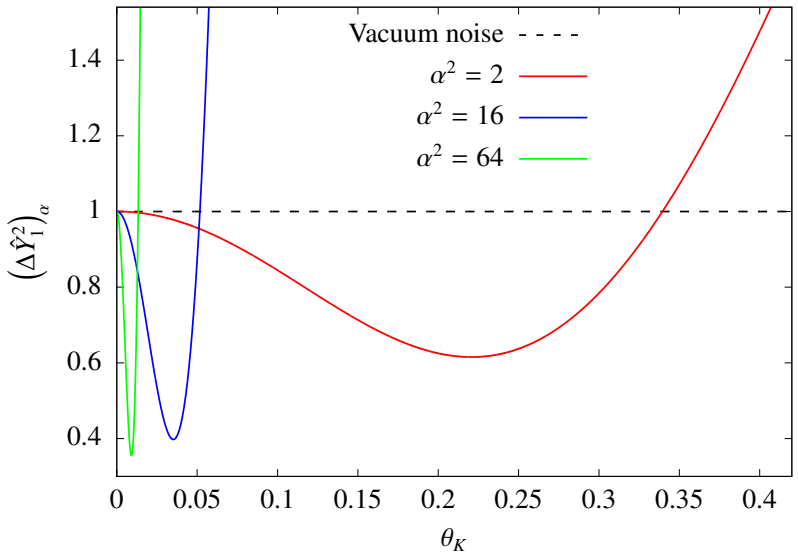

Figure 2.12: Simulation of the squeezed variance $(\Delta\hat{Y}_1^2)_\alpha$ as a function of the interaction parameter θ_K for different coherent intensities α^2. For larger values of α^2, the noise in $\hat{Y}_1$ is further reduced below the vacuum noise level (black dashed line).

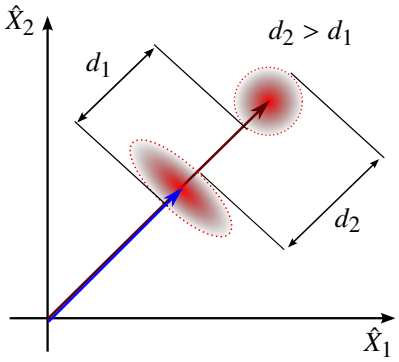

Figure 2.13: Illustration of the fundamental squeezing in the SHG process. The SHG acts as nonlinear loss on the fundamental pump, depicted by the dark red phasor. The conversion from the fundamental pump field to the SHG field reduces the dark red phasor to the blue one. The quantum noise of the initial state is also affected. The point corresponding to the top of the noise circle gains the largest nonlinear loss, denoted by d_2. The point, corresponding to the bottom of the circle is reduced by the amount d_1. Consequently, the quantum noise is squeezed in direction of the phasor. Adapted from ([90], p. 75).

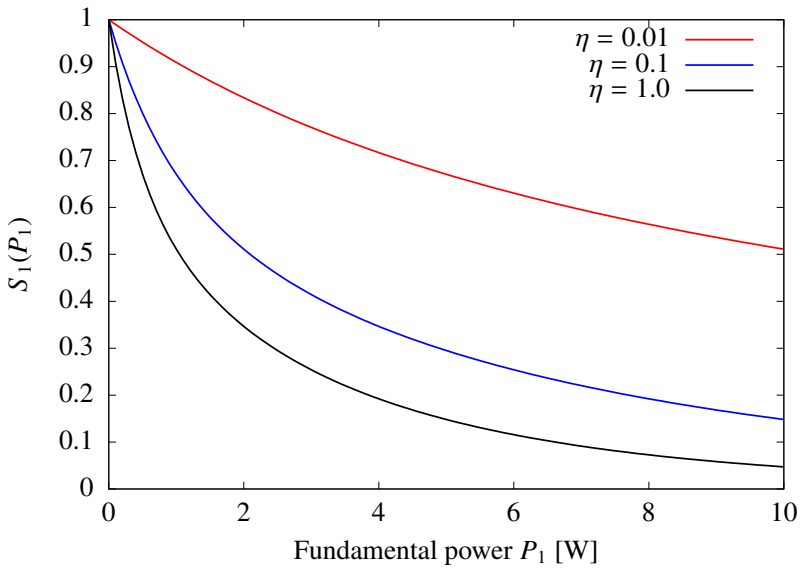

Figure 2.14: Simulated conversion efficiency-dependence of the squeezed fundamental field, produced in the SHG process. The squeezing of the fundamental field decreases with lower conversion efficiency η and it grows with the fundamental pump power P_1.

2.3.7 SHG squeezing

During the SHG conversion process, both, the fundamental field as well as the SHG field get squeezed. In this work, only the squeezing of the fundamental field is of importance. As shown in figure 2.13, the generation of the SHG light acts as nonlinear loss on the fundamental field. The length of the initial coherent state, illustrated by the dark red phasor, is reduced to the blue phasor. The nonlinear loss also transforms the circular quantum noise distribution of the initial coherent state. The point, corresponding to the top of the noise circle (seen in direction of the phasor) is the point of the largest intensity. It gets attenuated by the nonlinear loss by the amount d_2. The bottom of the circular noise distribution corresponds to the lowest intensity. This point experiences an attenuation of d_1. Since the top of the quantum noise circle corresponds to a larger fundamental intensity, it gets further reduced, than the bottom point. Thus, $d_2 > d_1$ and the quantum noise of the fundamental field gets squeezed in direction of the phasor ([90], p. 75). In order to fulfill Heisenberg's uncertainty principle, the quantum noise in direction perpendicular to the phasor is increased above the vacuum noise. The variance of the fundamental field is given by [72]

$$S_1 = [1 - \kappa \tanh(\kappa)^2 + 2 \tanh(\kappa)^2] \operatorname{sech}(\kappa)^2, \tag{2.102}$$

where $\kappa = \sqrt{\eta P_1}$ is the rescaled fundamental power. η denotes the conversion efficiency and P_1 is the fundamental power. As shown in figure 2.14, the squeezing of the fundamental light decreases for lower conversion efficiencies and increases with the pump power P_1.

2.3.8 Squeezing in the quantum sideband picture

Another alternative to illustrate squeezed states is the quantum sideband picture. To get a better idea of this picture, first the classical sideband picture is presented, which is used to describe amplitude and phase modulation of an electrical field. In the complex plane, the electric field can be represented by a vector that rotates with the frequency ω_0, named carrier. If now the transition into the so called rotating-frame coordinate system is performed, the carrier remains stationary. Periodic length and phase changes of the carrier field, called amplitude and phase modulation, can be described by small phasors, rotating at a lower and an upper sideband frequency. An amplitude modulated carrier field with frequency ω_0 can be written as ([17], p. 26)

$$\alpha_{\mathrm{am}}(t) = \alpha_0 \exp(\mathrm{i}\omega_0 t) [1 + m \cos(\Omega t)], \tag{2.103}$$

where α_0 is the amplitude, m is the modulation index and Ω is the modulation frequency. An amplitude modulation transfers energy from the carrier into new components, the upper

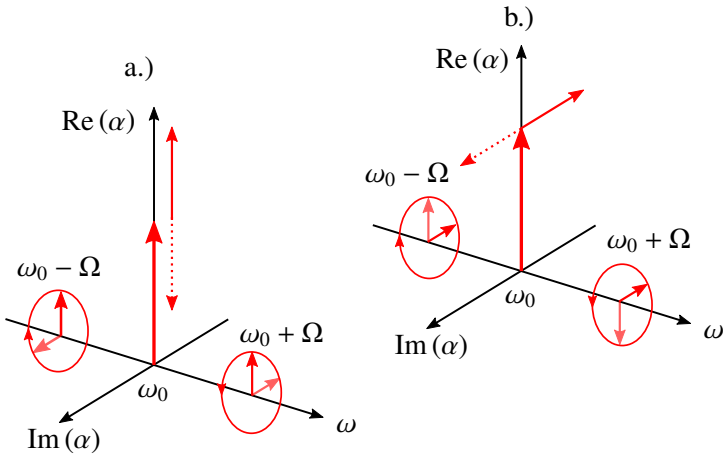

Figure 2.15: Amplitude and phase modulation in the rotating frame coordinate system. The lower sideband, rotates with frequency $-\Omega$ clockwise around the stationary carrier while the upper sideband spins counter clockwise with frequency Ω. For an amplitude modulation of the carrier, depicted in a.), both sidebands show a correlation in direction of the Re(α)-axis. The phase of the carrier is modulated, when both sidebands have a correlation along the Im(α)-axis, as shown in b.). Adapted from ([70], lecture 1, pp. 12 – 13).

and lower sidebands which are created at frequencies $\omega_0 - \Omega$ and $\omega_0 + \Omega$. The modulation index m determines the modulation strength and thus, how much energy is transferred from the carrier to the sidebands. For small modulations $m \ll 1$, only one lower and one upper sideband are taken into account and equation (2.103) can be approximated as

$$\alpha_{\mathrm{am}}(t) \approx \alpha_0 \exp(\mathrm{i}\omega_0 t)\left(1 + \frac{m}{2}\exp(\mathrm{i}\Omega t) + \frac{m}{2}\exp(-\mathrm{i}\Omega t)\right). \tag{2.104}$$

Figure 2.15a shows the carrier and both sidebands in the in rotating frame coordinate system. The lower sideband rotates clockwise with frequency $-\Omega$ and the upper sideband counter clockwise with frequency Ω. Both sidebands exhibit a correlation in direction of the Re(α) axis. Thus, the length of the carrier is periodically modulated. The phase modulation of an electric field is given by ([17], p. 24)

$$\alpha_{\mathrm{pm}}(t) = \alpha_0 \exp[\mathrm{i}(\omega_0 + m\cos(\Omega t))] \tag{2.105}$$

and can be approximated for a small modulation index $m \ll 1$ as ([17], p. 25)

$$\alpha_{\mathrm{pm}}(t) \approx \alpha_0 \exp(\mathrm{i}\omega_0 t)\left[1 + \mathrm{i}\frac{m}{2}\Big(\exp(\mathrm{i}\Omega t) + \exp(-\mathrm{i}\Omega t)\Big)\right]. \tag{2.106}$$

Lower and upper sideband show a correlation in direction of the Im (α) axis and thus, the phase of the carrier is periodically changed, as depicted in part b.) of figure 2.15.

In the same way, the quantum noise of a coherent amplitude at each frequency Ω_i can be characterized by the beat of the carrier field with a pair of a lower and an upper noise sideband [56]. This is shown in figure 2.16 for the quantum noise at the frequencies Ω_1 and Ω_2. Again, in the rotating frame coordinate system, the carrier with frequency ω_0 is stationary while the vacuum noise distributions rotate at frequencies $\pm\Omega_\mathrm{i}$. The quantum noise contribution at lower and upper sideband frequency is given by the phase space distribution of the vacuum noise with the variance $\Delta\hat{X}_1^2 = \Delta\hat{X}_2^2 = 1$ (dashed circles). Both noise contributions at $\omega_0 - \Omega_\mathrm{i}$ and $\omega_0 + \Omega_\mathrm{i}$ are random and don't show any mutual correlations. In order to describe pure vacuum noise, the carrier field in figure 2.16 has to be omitted. To produce vacuum squeezing at a sideband frequency Ω_i, a nonlinear medium is used to introduce a mutual correlation between the lower and the upper noise sideband at $\omega_0 \pm \Omega_i$. Figure 2.17a illustrates squeezing of the amplitude quadrature at the sideband frequencies Ω_1 and Ω_2. Here, the lower quantum noise sideband at $\omega_0 - \Omega_1$ and the upper quantum noise sideband at $\omega_0 + \Omega_1$ show an anti-correlation in $\hat{X}_1$ direction, marked by the '+'-sign. In the direction of $\hat{X}_2$, both sidebands exhibit a correlation described by the '×'-sign, resulting in anti-squeezing. The same applies for the quantum noise sidebands at $\omega_0 - \Omega_2$ and $\omega_0 + \Omega_2$. Squeezing of the phase quadrature at sideband frequencies Ω_1 and Ω_2 is depicted in figure 2.17b, where the anti-correlation, denoted by the □-symbol, is in direction of $\hat{X}_2$ while the correlation along the $\hat{X}_1$-axis is characterized by the △-symbol ([71], p. 31), [56].

2.3.9 Measuring squeezed light with the balanced homodyne detection

In a squeezing measurement, the reduction of quantum noise in a certain quadrature of the electric field has to be detected. Since the reduced quantum fluctuations are very small, they need to be amplified before they can be detected. This can be achieved by measuring the beat between a strong local oscillator (LO) field and the correlated sidebands (the signal field). Furthermore, the electric field oscillates with frequencies of several hundreds of THz. The 1550 nm light used in this experiment has a frequency of $f = 193 \cdot 10^{12}$ Hz. This corresponds to an oscillation period of $5.18 \cdot 10^{-15}$ s which is too fast to be resolved electronically. Consequently, it is also impossible to measure (quantum) modulations of the electric field directly [19], ([71], p. 11). An appropriate detection scheme that solves both problems is the balanced homodyne detection (BHD) which is depicted in figure 2.18. Here, a intense LO field $\hat{a}$, that also serves as phase reference, is superimposed with a weak signal field $\hat{b}$ on a 50/50 beam splitter. Both fields have the same spatial shape and polarization and are ideally from the same laser source in order to ensure temporal coherence. The outputs $\hat{c}$ and $\hat{d}$ of the beam splitter are monitored with the photo diodes PD_1 and PD_2, resulting in two photoelectric currents $\hat{i}_1$ and $\hat{i}_2$. By calculating the difference of the

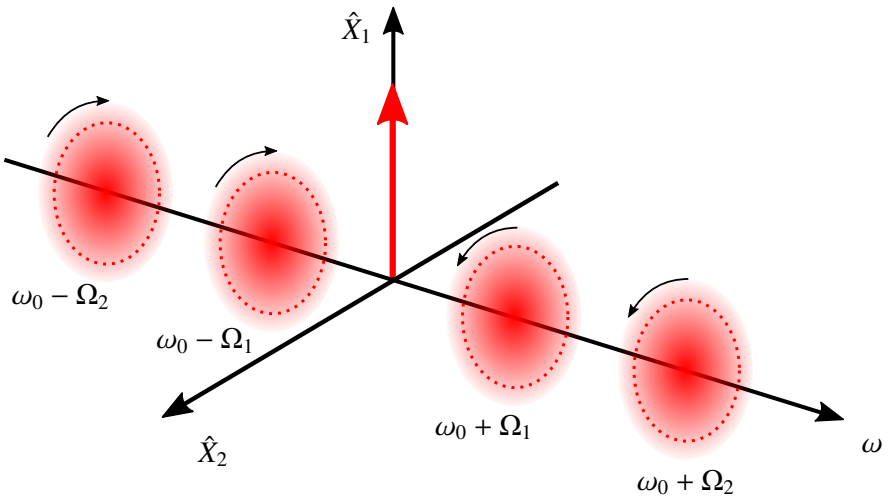

Figure 2.16: Quantum noise of a coherent amplitude in the quantum sideband picture. In the rotating frame coordinate system, the carrier at frequency ω_0 remains stationary while the noise sidebands rotate. The vacuum noise of the carrier at a certain sideband frequency Ω_i is described by the beat between the carrier and one lower and one upper quantum noise sideband at frequencies $\omega_0 \pm \Omega_i$. Adapted from ([14], p. 79) and ([71], p. 31).

photo currents, the oscillations in the THz-range are transformed into an electrical signal with maximum frequencies of several GHz. The optical mixing process together with the difference photo current detection corresponds to the transformation into the rotating frame coordinate system of the carrier. Thus, (quantum) modulations of the electric field can be investigated with state of the art spectrum analyzers.
In the case of perfect balancing, the beam splitter outputs $\hat{c}$ and $\hat{d}$ are related to the inputs $\hat{a}$ and $\hat{b}$ by the matrix-equation ([78], p. 44)

$$\begin{pmatrix}\hat{c}\\ \hat{d}\end{pmatrix} = \frac{1}{\sqrt{2}}\begin{pmatrix}1 & 1\\ -1 & 1\end{pmatrix}\begin{pmatrix}\hat{a}\\ \hat{b}\end{pmatrix} = \frac{1}{\sqrt{2}}\begin{pmatrix}\hat{a}+\hat{b}\\ -\hat{a}+\hat{b}\end{pmatrix}. \tag{2.107}$$

Here $\hat{a}$ is the local oscillator field and $\hat{b}$ is the signal field. From equation (2.107), the intensities $\hat{c}^\dagger\hat{c}$ and $\hat{d}^\dagger\hat{d}$ at the beam splitter outputs that are proportional to the photo currents measured by PD_1 and PD_2, can be calculated to

$$\hat{i}_1 \propto \hat{c}^\dagger\hat{c} = \frac{1}{2}\left(\hat{a}^\dagger\hat{a} + \hat{a}^\dagger\hat{b} + \hat{b}^\dagger\hat{a} + \hat{b}^\dagger\hat{b}\right) \tag{2.108}$$

and

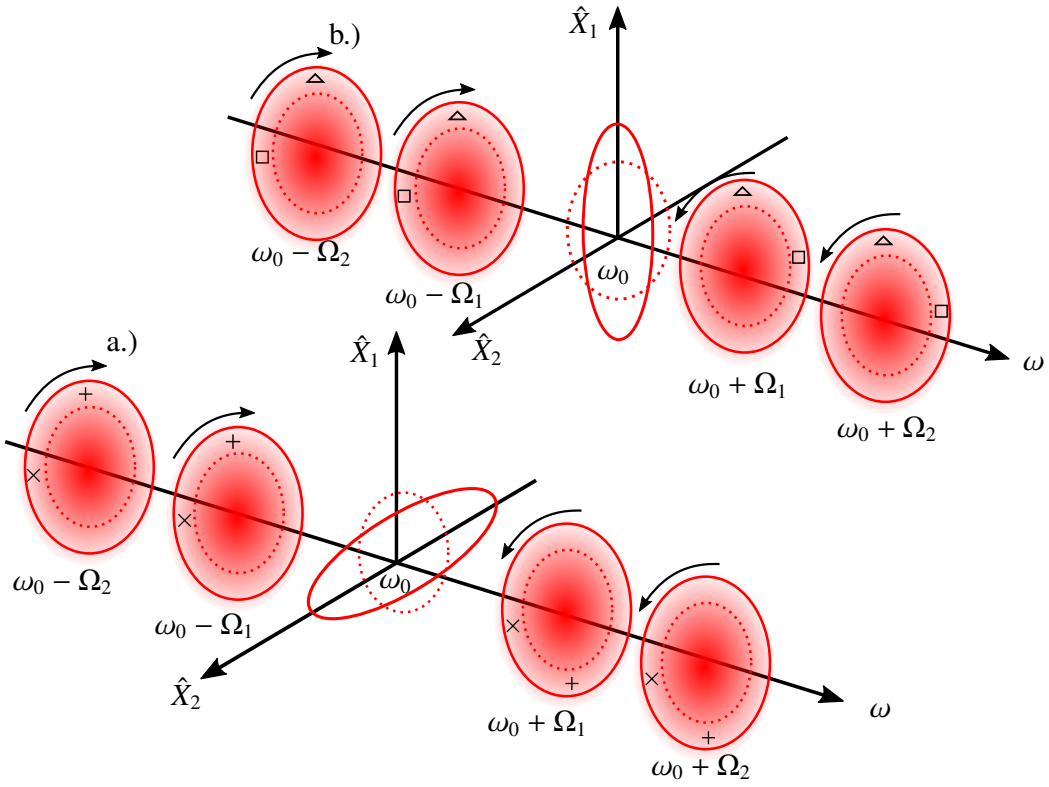

Figure 2.17: Visualization of squeezing in the quantum sideband picture. The sign '+' in figure a.) illustrates the quantum noise anti-correlation in $\hat{X}_1$-direction, resulting in amplitude squeezing at both sideband frequencies $\omega_0 \pm \Omega_1$ and $\omega_0 \pm \Omega_2$. The quantum noise correlation along the $\hat{X}_2$-axis is shown by the $\times$-sign. In figure b.), the quantum noise anti-correlations at the sideband frequencies $\omega_0 \pm \Omega_1$ and $\omega_0 \pm \Omega_2$ are shown by the $\square$-symbol along the $\hat{X}_2$-direction, leading to a phase squeezed state. The correlations are denoted by $\triangle$. Adapted from ([71], p. 31).

$$\hat{i}_2 \propto \hat{d}^\dagger \hat{d} = \frac{1}{2}\left(\hat{a}^\dagger \hat{a} - \hat{a}^\dagger \hat{b} - \hat{b}^\dagger \hat{a} + \hat{b}^\dagger \hat{b}\right). \tag{2.109}$$

Thus, the difference of both photo currents is

$$\hat{i}_\mathrm{d} \propto \hat{c}^\dagger \hat{c} - \hat{d}^\dagger \hat{d} = \hat{a}^\dagger \hat{b} + \hat{b}^\dagger \hat{a}. \tag{2.110}$$

The local oscillator field as well as the signal field can be split into two parts. The first part is their coherent and constant excitation, represented by the mean amplitudes α_LO and β. The second part are their fluctuations $\delta\hat{a}$ and $\delta\hat{b}$ ([14], p. 85). Thus, $\hat{a}$ and $\hat{b}$ become

$$\hat{a} = \alpha_\mathrm{LO} + \delta\hat{a} \tag{2.111}$$

$$\hat{b} = \beta + \delta\hat{b}. \tag{2.112}$$

Additionally, the relative phase ϑ between the two fields $\hat{a}$ and $\hat{b}$ can be decomposed from the complex amplitude $\hat{a}$ of the local oscillator ([78], p. 45)

$$\hat{a} = \alpha_\mathrm{LO} e^{\mathrm{i}\vartheta} + \delta\hat{a} e^{\mathrm{i}\vartheta}. \tag{2.113}$$

The amplitudes α_LO and β are now real numbers. By inserting equations (2.113) and (2.112) into (2.110), the photo current difference $\hat{i}_\mathrm{d}$ can be rewritten as

$$\hat{i}_\mathrm{d} \propto 2\cos(\vartheta)\,\alpha_\mathrm{LO}\beta + \alpha_\mathrm{LO}\delta\hat{X}^b_\vartheta + \beta\delta\hat{X}^a_{-\vartheta} + \delta\hat{a}^\dagger\delta\hat{b}e^{-\mathrm{i}\vartheta} + \delta\hat{b}^\dagger\delta\hat{a}e^{\mathrm{i}\vartheta}, \tag{2.114}$$

where the definition of the general quadrature operator from equation (2.35) has been used. During the balanced homodyne detection, the fluctuations $\delta\hat{X}^b_\vartheta$ of the signal field $\hat{b}$ are amplified by the amplitude α_LO of the local oscillator. Furthermore, the fluctuations of the local oscillator $\delta\hat{X}^a_{-\vartheta}$ are scaled with the amplitude β of the signal field. If the fluctuations of the signal and the local oscillator are both very small and $\alpha_\mathrm{LO} \gg \beta$, then $\alpha_\mathrm{LO}\delta\hat{X}^b_\vartheta \gg \beta\delta\hat{X}^a_{-\theta}$ is true. In this case, also the higher-order fluctuation terms $|\delta\hat{a}^\dagger\delta\hat{b}|$ and $|\delta\hat{b}^\dagger\delta\hat{a}|$ can be neglected and equation (2.114) becomes ([22], p. 33)

$$\hat{i}_\mathrm{d} \propto 2\cos(\vartheta)\,\alpha_\mathrm{LO}\beta + \alpha_\mathrm{LO}\delta\hat{X}^b_\vartheta. \tag{2.115}$$

For the measurement of (squeezed) vacuum, the amplitude of the signal is $\beta = 0$ and the difference of the photo currents is

$$\hat{i}_\mathrm{d} \propto \alpha_\mathrm{LO}\delta\hat{X}^b_\vartheta. \tag{2.116}$$

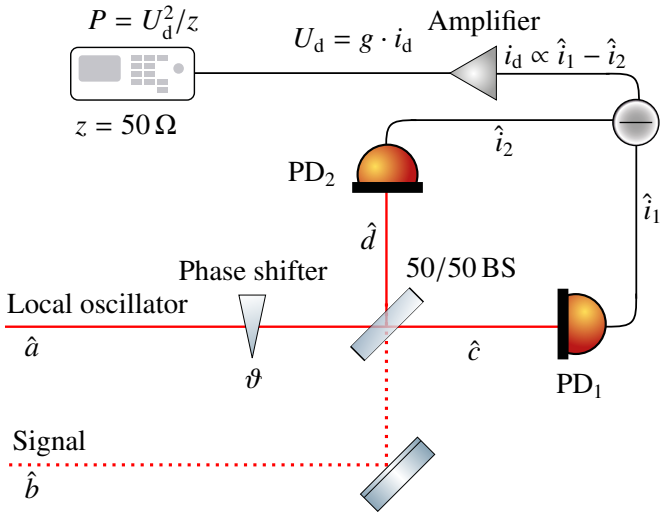

Figure 2.18: Balanced homodyne detection. A weak signal $\hat{b}$ and an intense local oscillator $\hat{a}$ are superimposed on a 50/50 beam splitter and the output fields $\hat{c}$ and $\hat{d}$ are measured with two photo diodes. The difference photo-current $\hat{i}_d \propto \hat{i}_1 - \hat{i}_2$ is amplified and transformed into a voltage U_d. A spectrum analyzer detects the power $P = U_d^2/z$ and displays a power spectral density. The phase shifter ϑ alternates the relative phase between the LO and the signal field. Thus, all quadratures of the signal field $\hat{b}$ can be monitored. Adapted from ([22], p. 27) and ([78], p. 44).

A trans-impedance amplifier intensifies $\hat{i}_d$ with a gain g and converts it into the voltage $U_d = g\hat{i}_d$. A spectrum analyzer detects the power $P = U_d^2/z$ where $z = 50\,\Omega$ is the typical input impedance, and yields a power spectral density. The power spectral density corresponds to the fluctuations of the measured photo current that are described by the variance ([22], p. 34)

$$V(\hat{i}_d) = \alpha_{LO}^2 (\delta \hat{X}_\vartheta^b)^2. \tag{2.117}$$

By changing the relative phase ϑ between the signal and the local oscillator with a piezo-actuated mirror, the fluctuations of the (squeezed) vacuum, scaled with the power of the local oscillator can be measured in an arbitrary quadrature.

2.3.10 Squeezed light and optical losses

Before a squeezed state is measured with a balanced homodyne detector, it experiences optical losses. Losses are due to the non-perfect escape efficiency of the squeezed light resonator, absorption and scattering on mirrors and lenses and non-perfect contrast at the beam splitter of the homodyne detector. Even the homodyne detectors photo diodes introduce losses, because they don't exhibit a quantum efficiency of 100%. The effect of

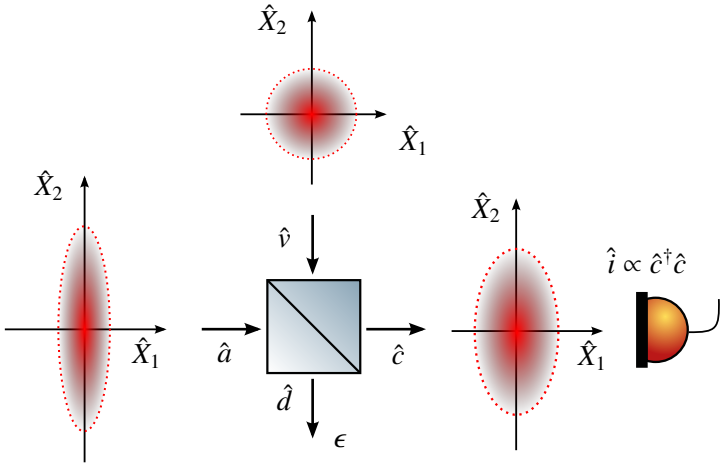

Figure 2.19: The impact of optical losses on an amplitude squeezed vacuum state. The effect of optical losses can be described by using the quantum model of a beam splitter. A small part ϵ of the squeezed field in port $\hat{a}$ is reflected towards port $\hat{d}$. Simultaneously, vacuum noise $\hat{v}$ is mixed in from the upper port. Thus, the transmitted state in port $\hat{c}$ is transformed into a mixed state that exhibits less amplitude squeezing. Adapted from ([87], p. 32).

optical losses on an amplitude squeezed vacuum state is depicted in figure 2.19. It can be modeled using a quantum-mechanical beam splitter with a (small) reflectivity of ϵ and a transmission of $1 - \epsilon$. Thus, a small part of the injected signal $\hat{a}$ (here the amplitude squeezed vacuum) is reflected in direction of $\hat{d}$ and simultaneously vacuum $\hat{v}$ is coupled in to fulfill energy conservation. The transmitted signal $\hat{c}$ can be calculated with the beam splitter matrix ([78], p. 47)

$$\begin{pmatrix} \hat{c} \\ \hat{d} \end{pmatrix} = \begin{pmatrix} \sqrt{1-\epsilon} & \sqrt{\epsilon} \\ -\sqrt{\epsilon} & \sqrt{1-\epsilon} \end{pmatrix} \begin{pmatrix} \hat{a} \\ \hat{v} \end{pmatrix}. \tag{2.118}$$

Writing the vacuum fluctuations as $\hat{v} = \delta\hat{v}$, the transmitted field $\hat{c}$ becomes

$$\hat{c} = \sqrt{1-\epsilon}\hat{a} + \sqrt{\epsilon}\delta\hat{v}. \tag{2.119}$$

If the signal field is separated into mean value and fluctuations, $\hat{a} = \alpha + \delta\hat{a}$, and second-order fluctuations terms are neglected, the photon number corresponding to the photo current can be calculated via ([78], p. 47)

$$\begin{aligned}\hat{i} \propto \hat{c}^\dagger \hat{c} &= \left(\sqrt{1-\epsilon}\hat{a}^\dagger + \sqrt{\epsilon}\delta\hat{v}^\dagger\right)\left(\sqrt{1-\epsilon}\hat{a} + \sqrt{\epsilon}\delta\hat{v}\right) \\ &= (1-\epsilon)\,\hat{a}^\dagger\hat{a} + \sqrt{\epsilon\,(1-\epsilon)}\left(\hat{a}^\dagger\delta\hat{v} + \delta\hat{v}^\dagger\hat{a}\right) \\ &= (1-\epsilon)\left[\alpha^2 + \alpha\delta\hat{X}_1^a\right] + \alpha\sqrt{\epsilon\,(1-\epsilon)}\delta\hat{X}_1^v \\ &= (1-\epsilon)\,\alpha^2 + \sqrt{1-\epsilon}\alpha\left[\sqrt{1-\epsilon}\delta\hat{X}_1^a + \sqrt{\epsilon}\delta\hat{X}_1^v\right]. \end{aligned} \tag{2.120}$$

On the other hand, the photo current can be calculated by decomposing $\hat{c}$ into the average amplitude c and the fluctuations $\delta\hat{c}$

$$\begin{aligned}\hat{i} \propto \hat{c}^\dagger \hat{c} &= (c + \delta\hat{c}^\dagger)\,(c + \delta\hat{c}) \\ &= c^2 + c\delta\hat{X}_1^c. \end{aligned} \tag{2.121}$$

The comparison of equations (2.120) and (2.121) yields the fluctuations of the photo current

$$\delta\hat{X}_1^c = \sqrt{1-\epsilon}\delta\hat{X}_1^a + \sqrt{\epsilon}\delta\hat{X}_1^v. \tag{2.122}$$

The variance of the beam splitter output $\hat{c}$ is ([78], p. 47)

$$V\left(\delta\hat{X}_1^c\right) = (1-\epsilon)V(\delta\hat{X}_1^a) + \epsilon V(\delta\hat{X}_1^v). \tag{2.123}$$

Equation (2.123) again illustrates that a squeezed state is superimposed with vacuum when experiencing optical loss. After being interfered with vacuum, the amplitude squeezed state becomes a mixed state with less squeezing than the pure state, as visualized in figure 2.19. In a squeezing measurement, the variance of the signal field $V(\delta\hat{X}_1^a) = x$ [dB] is measured with a spectrum analyzer in decibel. Furthermore, the variance of the vacuum is $V(\delta\hat{X}_1^v) = 1$ and equation (2.123) can be written as ([22], p. 29)

$$V\left(\delta\hat{X}_1^c\right) = 10 \cdot \log_{10}\left[(1-\epsilon)10^{x\,[\mathrm{dB}]/10} + \epsilon\right]. \tag{2.124}$$

Equation (2.124) is plotted in figure 2.20 for the initial anti-squeezed and squeezed variances of ±6 dB and ±12 dB. It can be seen that optical losses reduces the squeezed variance faster than the anti-squeezed variance. Furthermore, the squeezed variance showing a larger initial squeezing level is faster degraded by optical losses than a squeezed variance with a smaller initial squeezing level.

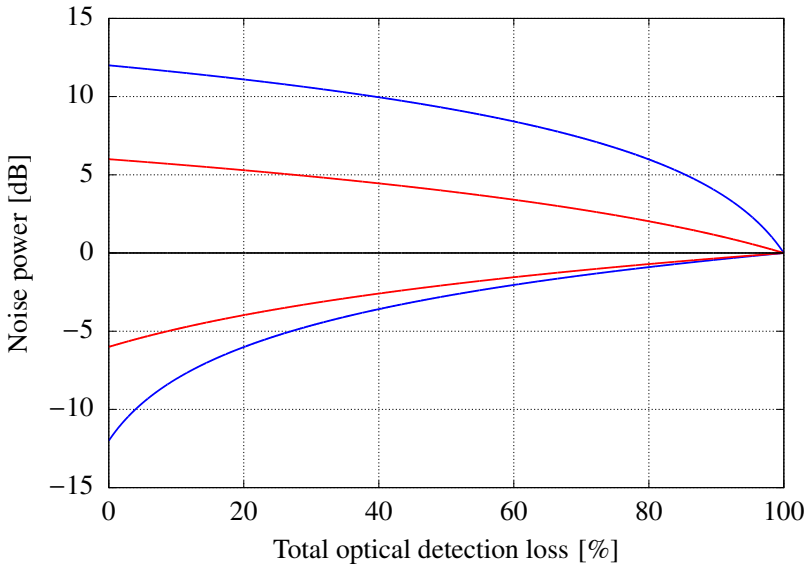

Figure 2.20: Simulated effect of optical losses on anti-squeezed and squeezed variance. The red graph shows the anti-squeezed and squeezed variance as a function of the optical losses for an initial anti-squeezing and squeezing of ±6 dB while the blue graph visualizes the dependence for the initial values of ±12 dB. Optical losses degrade the squeezed variance faster than the anti-squeezed variance. Also, optical losses degrade squeezed variances with a large initial squeezing level stronger than variances with a smaller initial squeezing level.

2.4 Experimental starting point

As explained in section 2.2.1, the third-order optical Kerr effect introduces an intensity-dependent phase shift that can be used to squeeze the quantum noise of the carrier field. A non-classical noise reduction of 5.1 dB using laser pulses injected into an optical fiber was demonstrated in [39]. However, since third-order nonlinearities are very small ($n_2 \sim 10^{-20}\,\mathrm{m^2/W}$) ([18], p. 211), no non-classical noise reduction in the continuous-wave laser regime has been observed. As described by equation (2.14), a second-order nonlinear medium operated in the SHG conversion minimum provides a similar intensity-dependent phase shift, as a third-order medium. Since the second-order nonlinearity is two orders of magnitude larger ($n_2 \sim 10^{-18}\,\mathrm{m^2/W}$) ([83], p. 134), it can be employed in the continuous-wave laser regime. White et al. [91] investigated the light reflected of a monolithic Kerr nonlinear cavity which was made of magnesium-doped lithium niobate. By means of the self-homodyne detection technique, a classical laser power noise reduction of 1.5 dB was observed, probing the light reflected off the Kerr cavity. An even larger classical laser power noise suppression of 32 dB was achieved by Khalaidovski et al. [46]. Since the sideband frequency of their measurement was close to the lasers relaxation oscillation, the laser exhibited a large amount of technical noise. Consequently, no non-classical noise reduction could be accomplished. A non-classical noise reduction of about 1.5 dB of a bright coherent state at 1.06 μm was demonstrated by Zhang et al. [94]. They used continuous-wave laser pump light and periodically-poled lithium niobate as cascaded second-order nonlinear medium. However, to the best of my knowledge, no generation of squeezed vacuum states in the continuous-wave laser regime using a cascaded second-order nonlinearity has been reported so far.

In the experiment presented in this work, a new approach was taken to produce squeezed vacuum states via the second-order cascaded optical Kerr effect. The main changes compared to the experiments in [46, 91] were:

1. To be shot noise limited from the beginning, squeezing measurements were carried out at sideband frequencies of several hundred MHz up to one GHz.

2. According to equation (2.14), the intensity-dependent phase shift is proportional to the second-order nonlinearity. The material used in [46] was magnesium-doped lithium niobate which has a second-order nonlinearity of 4.7 pm/V ([48], p. 18). In this experiment, periodically poled potassium titanyl phosphate (PPKTP) with an even stronger nonlinearity of 7.3 pm/V [12] was employed. Thus, the necessary pump power to exploit the cascaded Kerr effect could be reduced from several hundreds of milliwatts [46] to below 100 mW.

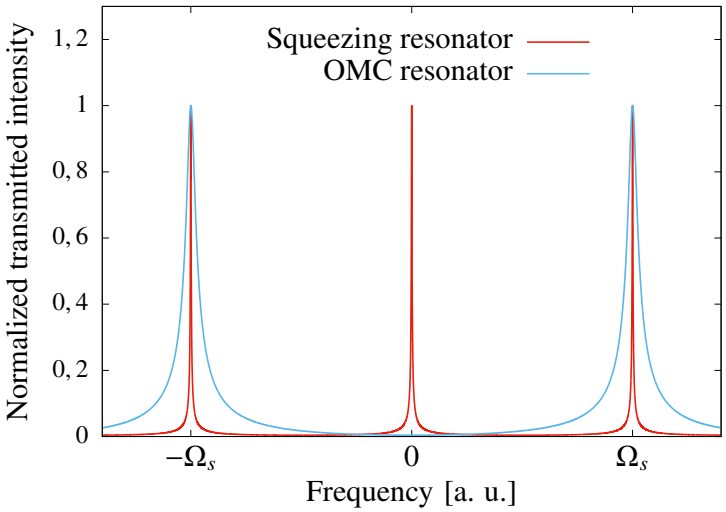

Figure 2.21: Illustration of the concept for the separation of the 1550 nm carrier light and the squeezed sidebands. The red graph depicts the transmission of the squeezing resonator and the blue line shows the one from the OMC resonator. Both are plotted as a function of the sideband frequency Ω. If the FSR of the OMC is twice as large as the FSR of the squeezing resonator, the carrier located at zero frequency gets reflected while the sidebands at $-\Omega_s$ and Ω_s get transmitted. Thus, the squeezed vacuum can be measured at a sideband frequency corresponding to the first FSR of the squeezing resonator, without damaging the homodyne detector photo diodes.

3. The new experiment was performed at the longer laser wavelength of 1550 nm. 1550 nm shows less absorption $\left(\alpha < \frac{0.01\%}{\text{cm}}\right)$ in PPKTP [12] than 1064 nm in lithium niobate $\left(\alpha < \frac{0.1\%}{\text{cm}}\right)$ ([48], p. 18). Consequently, thermal effects like the change of the refractive index and thermal expansion of the nonlinear crystal were reduced.

2.4.1 Choice and design of the squeezing resonator

As illustrated in figure 2.12, the non-classical noise reduction generated with the Kerr effect increases with larger pump power. For this reason, a very important property of the squeezing resonator is the intra-cavity power build up that is defined by the ratio of the power circulating inside of the resonator I_{cav} and the incident laser power I_{in} ([73], p. 416), ([60], p. 140)

$$PB = \frac{I_{\text{cav}}}{I_{\text{in}}} = \frac{1 - R_1}{\left(1 - \sqrt{R_1 R_2} V\right)^2}. \tag{2.125}$$

The power build up only depends on the mirror reflectivities R_1 and R_2 and on the optical loss V. For an over-coupled resonator with $R_1 < R_2 V^2$, larger reflectivities will result

in an increased power build up. To prevent the photo-diodes of the homodyne detector from damage, the squeezed sidebands need to be separated from the carrier light before they are measured. This can be achieved by reflecting the carrier from an off-resonant three mirror mode-cleaner ring resonator [32], while the sidebands get transmitted. In this thesis, this mode-cleaner resonator will be named *output mode-cleaner* (OMC). The OMC has a round-trip length of $L_{\mathrm{MC}} \approx 42\,\mathrm{cm}$, resulting in a free spectral range (FSR) of ([60], p. 564)

$$\Delta f = \frac{c}{L} \approx 714\,\mathrm{MHz}, \tag{2.126}$$

where c is the speed of light in vacuum. To achieve the off-resonant carrier reflection, the FSR of the squeezing resonator needs to be half of the OMC FSR. Or, in other words, the round-trip length of the squeezing resonator needs to be twice the one of the OMC. This results in a FSR of $\Delta f_{\mathrm{sqz}} \approx 357\,\mathrm{MHz}$ and is illustrated in figure 2.21. The red graph represents the resonance peaks of the squeezing resonator and the blue graph the resonance peaks of the OMC. The carrier light at zero frequency is reflected by the OMC, while the squeezed sidebands at the frequencies $-\Omega_s$ and $+\Omega_s$ (the minus and plus first FSR of the squeezing resonator) get transmitted. Another requirement of the squeezing resonator is a small waist size w_0 in order to maximize the factor χ that is defined in equation (2.87). The waist of a two-mirror resonator is defined as ([73], p. 747)

$$w_0 = \left(\frac{L\lambda}{\pi} \sqrt{\frac{g_1 g_2 (1 - g_1 g_2)}{g_1 + g_2 - 2 g_1 g_2}} \right)^{1/2}, \tag{2.127}$$

where g_1 and g_2 are given by equations (3.2) and (3.3), respectively. w_0 increases with the laser wavelength λ and with the round-trip length L. For this reason, the two-mirror resonator configuration used in many squeezing experiments is not suitable here. The resonator type employed in this experiment that fulfills both, a small waist and a large round-trip length, is the bow-tie resonator. The optical design of the chosen bow-tie configuration is depicted in figure 2.22. It was composed of four mirrors and a periodically poled potassium titanyl phosphate (PPKTP) crystal with a geometrical length of 9.32 mm that was manufactured by the company *Raicol Crystals*. On both crystal end-faces an anti-reflection coating with AR $\leq 0.05\,\%$ was applied. Mirror M_1 and M_2 were convex with a radius of curvature of $-500\,\mathrm{mm}$, yielding to an enlargement of the resonator mode. The concave mirror M_3 focused the resonator mode down to a waist size of $30.4\,\mu\mathrm{m}$ in the middle of the PPKTP crystal. The coupling mirror M_1 of the bow-tie resonator had a design power reflectivity of $R_{1,\,1550\,\mathrm{nm}} = 99\,\%$ at 1550 nm while the design power reflectivities of the other three mirrors were $R_{2,\,1550\,\mathrm{nm}} = R_{3,\,1550\,\mathrm{nm}} = R_{4,\,1550\,\mathrm{nm}} = 99.98\,\%$. All mirror reflectivities were specified for s-polarized light. They yielded a theoretical finesse of $F_{1550\,\mathrm{nm}} = 590$

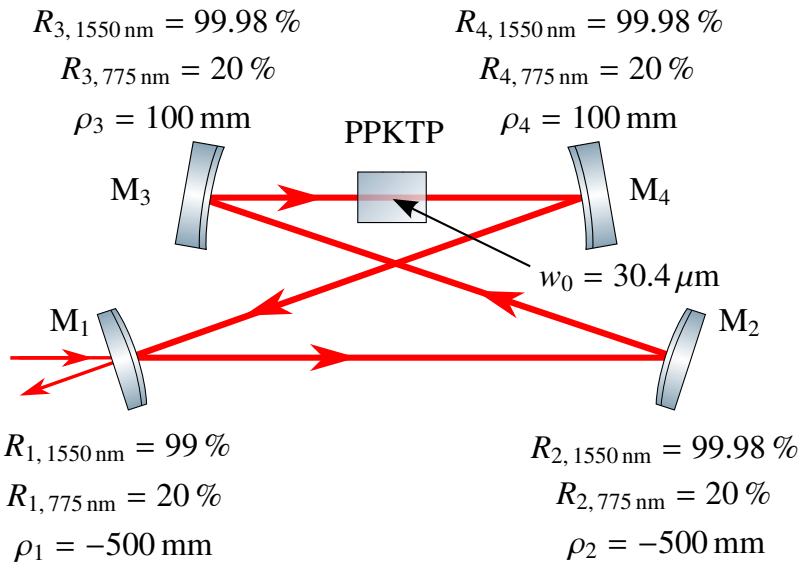

Figure 2.22: Design of the bow-tie squeezing resonator. The bow-tie resonator consisted of four mirrors and contained a 9.32 mm long PPKTP crystal. The coupling mirror M_1 and the mirror M_2 were convex in order to enlarge the diameter of the laser beam. The convex mirror M_3 focused the beam into the PPKTP crystal, leading to a waist size of $w_0 = 30.4\,\mu$m. The power reflectivity of the coupling mirror M_1 at 1550 nm was $R_{1,\,1550\,\mathrm{nm}} = 99\,\%$ while the other three mirrors had $R_{2,\,1550\,\mathrm{nm}} = R_{3,\,1550\,\mathrm{nm}} = R_{4,\,1550\,\mathrm{nm}} = 99.98\,\%$.

and a power build up of 354.5. For all four mirrors, the power reflectivity at 775 nm was 20 % and thus, no power build up for the second harmonic light occurred. The total optical round-trip length of the bow-tie resonator was $L_{\text{bow-tie}} \approx 0.8369\,\mathrm{m}$, resulting in a FSR of 358.22MHz. Mirror M_3 was clamped on a piezo-electric transducer (PZT). Thus, its position could be actuated in order to geometrically change the bow-tie resonator round-trip length. The PPKTP crystal was positioned inside of an oven and its temperature was controlled by a peltier element. Further information about the mechanical design of the bow-tie resonator can be found in ([74], pp. 65 – 66).

2.5 Experimental results

This experiment was realized in collaboration with Stefan Ast. His PhD thesis [11] shows the measured squeezing spectra at the first and third FSR of the bow-tie squeezing resonator. My thesis for the first time presents the measurements of the SHG conversion as well as the matching of the FSRs of the bow-tie resonator and the OMC. Furthermore, my thesis for the first time shows the zero-span squeezing measurements at the first and third

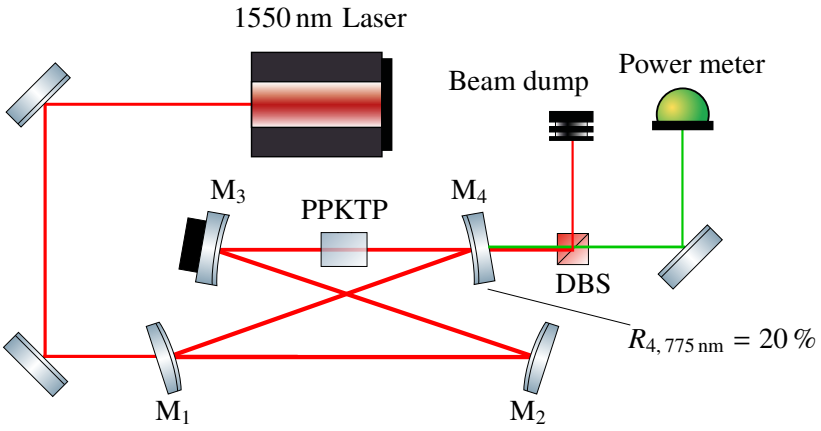

Figure 2.23: Simplified experimental setup for measuring the SHG conversion. 8 mW 1550 nm light were injected into the bow-tie resonator while the temperature of the PPKTP crystal was changed with a Peltier element. Excess 1550 nm light was reflected by a dichroic beam splitter (DBS) and the transmitted 775 nm power was detected with a power meter.

bow-tie FSR and also the verification measurement for Kerr squeezing. Additionally, my thesis presents Kerr squeezing measurements at the first and third bow-tie FSR as a function of the fundamental pump power.

2.5.1 Measurement of the SHG conversion minima

In this experiment the Erbium-doped continuous-wave single frequency 1550 nm fiber seed laser *Koheras AdjustiK* (model E15) was used as laser source. It exhibited low frequency noise and a maximum output power of 2 W. The output power of the seed laser was intensified to a maximum of 5 W by the external amplifier *Koheras BoostiK*. Both, seed laser and amplifier were manufactured by *NKT Photonics*.
As pointed out by equation (2.14), the nonlinear phase shift due to the cascaded optical Kerr effect is maximized in the first upper and lower SHG conversion minimum. To measure the conversion of the 1550 nm fundamental light to the 775 nm SHG light as a function of the wavevector mismatch, the temperature of the PPKTP crystal was scanned in the range between 20 °C and 88 °C with a Peltier element. During the measurement, a power of 8.8 mW 1550 nm s-polarized pump light was injected into the bow-tie resonator. As shown in figure 2.23, 80 % of the frequency doubled 775 nm light was transmitted through mirror M_4 of the bow-tie resonator. Before the detection with a power meter, the 775 nm light was separated

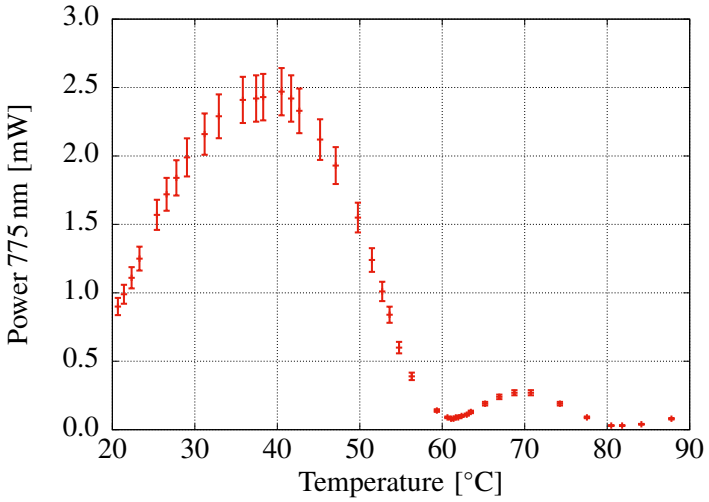

Figure 2.24: Conversion of 1550 nm to 775 nm. The temperature of the PPKTP crystal was changed within the temperature range between 20 °C and 88 °C and a light power of 8.8 mW was incident onto the bow-tie resonator. For each measurement point, the bow-tie resonator was length-stabilized to be resonant for the 1550 nm light. A conversion maximum was detected at 40.5 °C. The first conversion minimum was observed at a temperature of 61.2 °C and the second at 81.8 °C. The error bars are due to the 7% measurement error of the power sensor.

from excess 1550 nm light by a dichroic beam splitter (DBS) which reflected the fundamental light and transmitted the frequency doubled light. Figure 2.24 shows the power of the detected 775 nm light with the 7% measurement error bar of the power sensor plotted against the crystal temperature. For each measurement point, the length of the bow-tie resonator was stabilized on resonance with the Pound-Drever-Hall (PDH) technique [29] and the transmitted 775 nm light was measured. A conversion maximum was observed at a crystal temperature of 40.5 °C while the first and the second conversion minimum were measured at 61.2 °C and 81.8 °C.

2.5.2 Observation and verification of the cascaded optical Kerr effect

As numerically simulated in figure 2.4, the intensity-dependent phase shift of the cascaded optical Kerr effect results in a deformation of the cavity resonance peaks. To experimentally observe this deformation, the temperature of the PPKTP crystal was adjusted to 61.2 °C, the first SHG conversion minimum, and a 1550 nm pump power of 80 mW was used. The resonance peak was detected in transmission of the bow-tie resonator with a photo diode while its round-trip length was linearly scanned with a PZT. The blue graph in figure 2.25 shows the observed resonance peak deformation for an external increase of the resonator

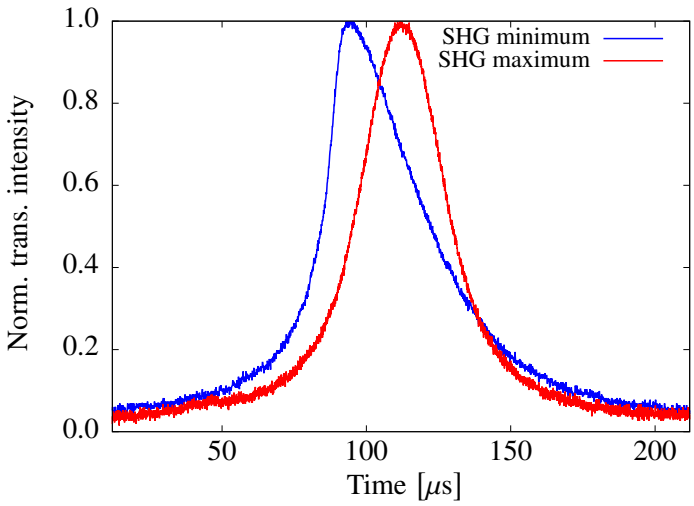

Figure 2.25: Comparison of the measured and normalized bow-tie resonance peaks. In the SHG conversion maximum at 40.5 ° C, a resonance peak without deformation (red graph) was detected in transmission of the bow-tie resonator. After changing the crystal temperature to 61.2 ° C, the first conversion minimum, a resonance peak deformation (blue graph) induced by the nonlinear phase shift of the cascaded Kerr effect was observed. For both measurements, a light power of 80 mW was modematched into the bow-tie resonator.

round-trip length. Furthermore, the temperature of the PPKTP crystal was tuned to 40.5 °C, the SHG conversion maximum, and again 80 mW 1550 nm light were injected into the bow-tie resonator. As predicted by theory, the measured resonance peak did not show any deformation because the intensity-dependent phase shift of the Kerr effect vanishes in the SHG conversion maximum. This is shown by the red graph in figure 2.25.

To verify that the reason for the resonance peak deformation was the cascaded Kerr effect, a differentiation from thermally-induced resonance distortions was necessary. The latter were suppressed by fast scans of the resonance peak. For this purpose, a triangle-wave voltage with an amplitude of 3 Volt and a frequency of 500 Hz was applied to the piezo-actuator. A power of 226 mW was injected into the bow-tie resonator and the temperature of the PPKTP crystal was adjusted to the first conversion minimum. The resonance peaks for external lengthening as well as for external shortening of the round-trip length were measured in transmission of the bow-tie resonator. For external lengthening, the full width at half maximum of the resonance was scanned within 3.7 μs and for external shortening in 5.5 μs. As depicted in figure 2.26, in both cases, the characteristic shape of the resonance peaks, displaying a steep and a shallow slope, remained. Thus, the observed resonance peak deformation was caused by the nonlinear phase shift of the cascaded optical Kerr effect and not by thermal effects.

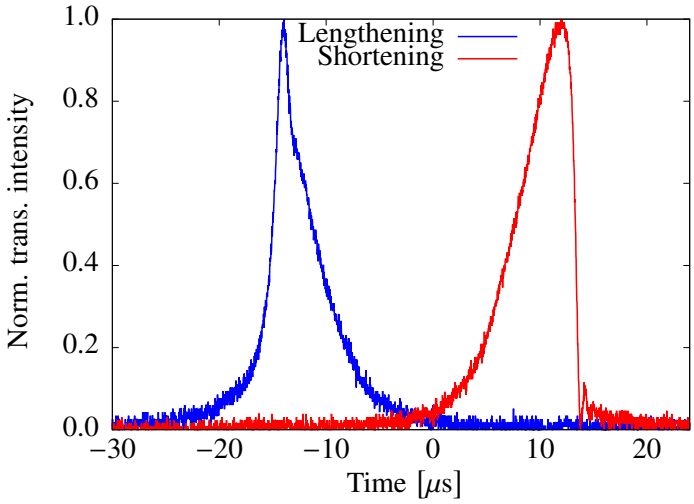

Figure 2.26: Fast scan of the bow-tie resonance. To verify that the observed resonance peak deformation is caused by the intensity-dependent phase shift of the cascaded Kerr effect and not by thermal distortions, fast resonance scans were applied. For external lengthening (blue graph), the full width at half maximum of the bow-tie resonance was scanned in 3.7 μs and for external shortening (red graph) within 5.5 μs. Since each resonance peak maintained its characteristic shape, showing one steep and one shallow slope, a Kerr-induced deformation was observed.

To prove the intensity-dependence of the Kerr-induced resonance peak deformation which was numerically simulated in figure 2.4, the temperature of the PPKTP crystal was again tuned to 61.2 °C. Resonance peaks for external lengthening and for external shortening were detected in transmission of the bow-tie resonator, using different 1550 nm pump powers in a range between 77.8 mW and 102.2 mW. As illustrated in figure 2.27, the resonance peak deformation increased with larger pump power for external lengthening as well as for external shortening.

2.5.3 Matching the free spectral ranges of the bow-tie resonator and the output mode cleaner resonator

As emphasized in section 2.4.1 it was crucial that the FSR of the OMC ring resonator, that was employed to separate the carrier light and the squeezed sidebands, has twice the FSR of the bow-tie squeezing resonator. With regard to laser power fluctuations, an optical resonator acts as a low pass with a corner frequency at half of the FWHM. The transfer function of the bow-tie resonator is given by ([73], p. 419)

$$H_{\mathrm{T}}(f) = \frac{1 - \sqrt{R_1 R_2 R_3 R_4}}{1 - \sqrt{R_1 R_2 R_3 R_4}\exp\left(\mathrm{i}2\pi f/\Delta f\right)}. \tag{2.128}$$

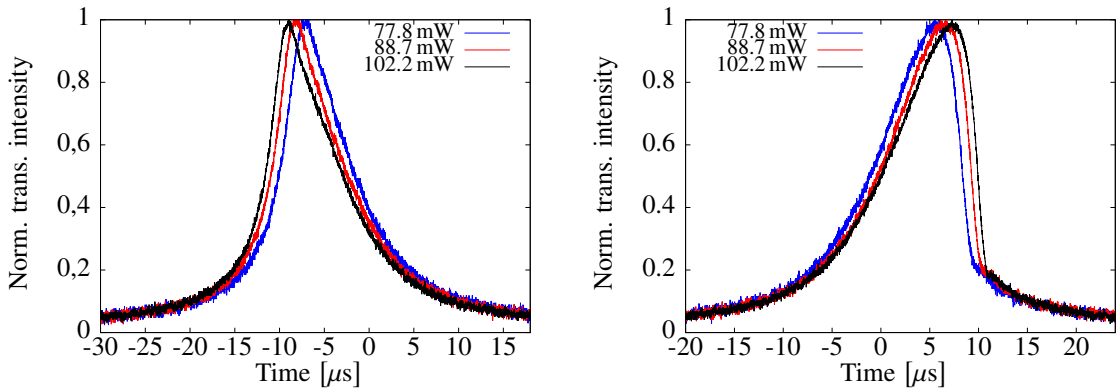

(a) External lengthening (b) External shortening

Figure 2.27: Power dependence of the cascaded optical Kerr effect. The resonance peaks were recorded in the first SHG conversion minimum for three different input powers and for external lengthening (a) of the bow-tie resonator as well as for external shortening (b). As predicted by theory, the intensity-dependent phase shift due to the cascaded Kerr effect increased with laser power. This resulted in a larger resonance peak deformation for higher laser power.

Here R_1, R_2, R_3 and R_4 are the mirror power reflectivities, f is the frequency, and Δf is the free spectral range. The absolute value of $H_\mathrm{T}(f)$ is plotted in figure 2.28 using the design values of the bow-tie resonator from section 2.4.1. Transmitted laser power fluctuations are attenuated by 3 dB at 303 kHz. While maximum attenuation takes place at multiple integers of $\Delta f_{\text{bow-tie}}/2$, the bow-tie resonator again transmits power fluctuations at multiple integers of its FSR. This behavior was used to measure the exact FSR of the bow-tie resonator by transmitting excess intensity noise of the fiber laser. Before the measurement, all mode cleaner resonators, providing a suppression of laser power noise, were removed. The temperature of the PPKTP crystal was adjusted to the first SHG conversion minimum and the length of the bow-tie resonator was stabilized with the Pound-Drever-Hall technique to be resonant for the fundamental 1550 nm light. A light power of 140 mW was injected into the bow-tie resonator and the transmitted laser noise was detected in transmission with a large-bandwidth photo diode, see figure 2.29. A spectrum analyzer evaluated the residual laser power noise within the frequency range between 355 MHz and 361 MHz using a resolution bandwidth (RBW) of 100 kHz, a video bandwidth (VBW) of 2 Hz and a sweep time of 60 s. The detected, dark noise corrected and linearized transmission peak is plotted in figure 2.30. A fit with a Lorentzian function yielded a center frequency of about 358.265 MHz, which corresponded to first FSR of the bow-tie resonator. Thus, its optical round-trip length was 0.8368 m.

In an iterative process, the geometrical length of the OMC resonator was adjusted and the

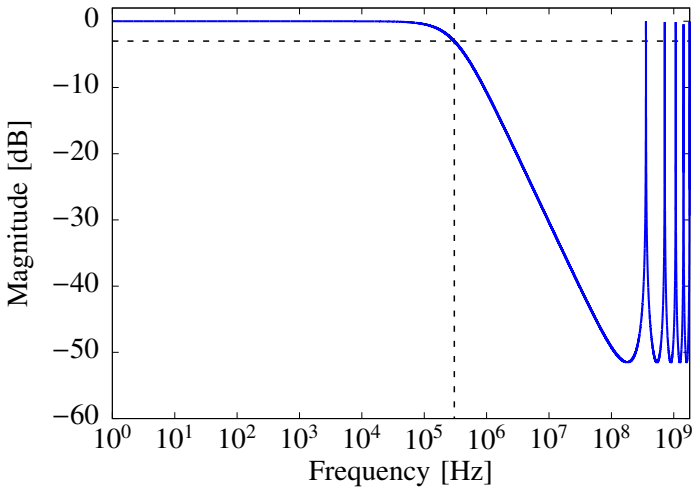

Figure 2.28: Simulated absolute value of the bow-tie resonator transfer function $H_T(f)$. Laser power fluctuations are suppressed by 3 dB at 303 kHz while maximum attenuation takes place at the half FSR of the bow-tie resonator. At multiple integers of the FSR, power fluctuations are again transmitted.

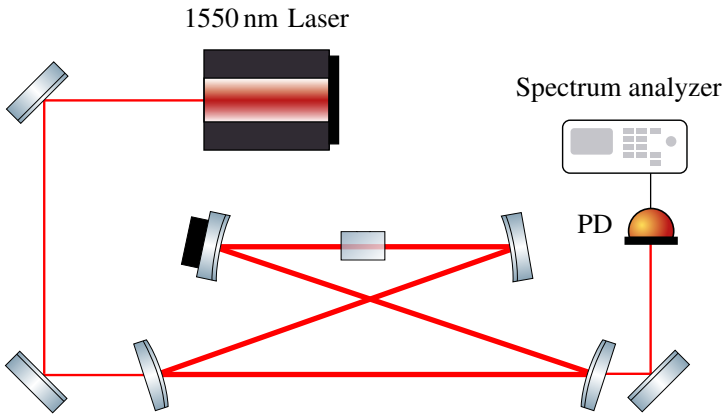

Figure 2.29: Simplified experimental setup for measuring the free spectral range of the bow-tie squeezing resonator. The length of the bow-tie resonator was stabilized to be resonant for the 1550 nm light using the Pound-Drever-Hall technique. A measurement of the transmitted laser power noise was performed with a large-bandwidth photo detector (PD). The measured spectrum was evaluated with a spectrum analyzer.

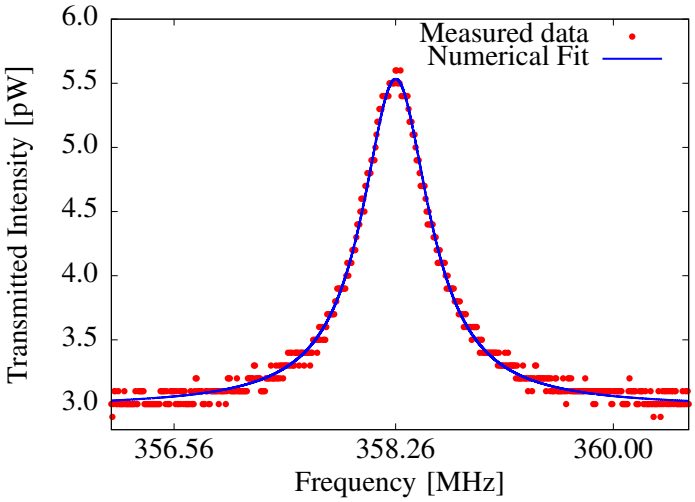

Figure 2.30: Bow-tie resonator laser power fluctuation transmission peak. High frequency power fluctuations of the 1550 nm fiber laser (red dots) were transmitted by the bow-tie resonator, recorded with a photo diode and evaluated with a spectrum analyzer using a RBW of 100 kHz, a VBW of 2 Hz and a sweep time of 60 s. The measured data was dark noise corrected and linearized. A Lorentzian fit yielded a center frequency of 358.265 MHz which corresponded to the first FSR of the bow-tie resonator.

corresponding transmission peak was measured with a similar setup, as the one shown in figure 2.29. Finally, the FSR of the OMC resonator was determined by measuring the transmitted laser power fluctuations within the frequency range between 710 MHz and 723 MHz. For this measurement, a RBW of 100 kHz, a VBW of 10 Hz and a sweep time of 26 s were used. A fit with a Lorentzian function yielded $\Delta f_{\mathrm{MC}} = 716.343\,\mathrm{MHz}$. Compared to $2 \cdot 358.265\,\mathrm{MHz} = 716.53\,\mathrm{MHz}$ a residual deviation of about 187 kHz remained.

2.5.4 Experimental setup for the generation of squeezed vacuum states by means of the cascaded optical Kerr effect

A simplified schematic of the experimental setup used to generate squeezed states of light with the cascaded optical Kerr effect is presented in figure 2.32. As already described in section 2.5.1, the utilized laser source consisted of an Erbium-doped continuous-wave single frequency 1550 nm fiber seed laser and an amplifier, providing laser radiation with a maximum output power of 5 W. A three mirror traveling-wave resonator filtered the 1550 nm laser light from high frequency intensity- and phase noise and provided a spatially cleaned TEM_{00} mode. This mode was then split into two parts, one serving as local oscillator for the homodyne detection and one acting as pump field for the bow-tie resonator. The length of the bow-tie resonator was stabilized with the Pound-Drever-Hall technique

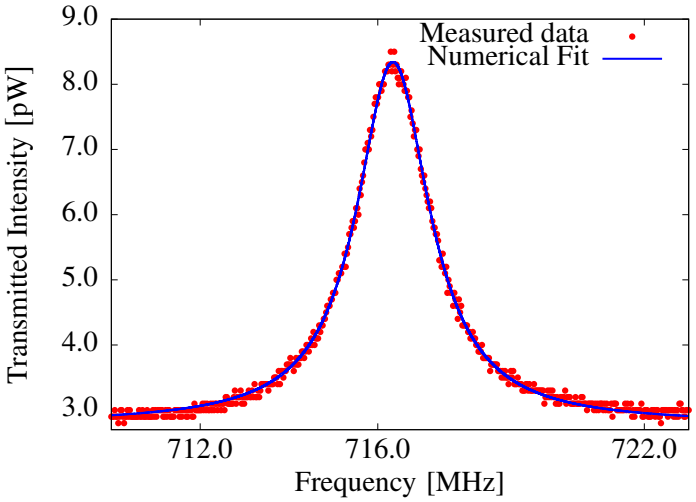

Figure 2.31: Power fluctuation transmission peak of the OMC resonator. High frequency power fluctuations of the 1550 nm fiber laser (red dots) were transmitted through the OMC, measured with a photo diode and evaluated with a spectrum analyzer using a RBW of 100 kHz, a VBW of 10 Hz and a sweep time of 26 s. The data was linearized and the electronic dark noise was subtracted. A Lorentzian fit yielded a center frequency of 716.363 MHz which corresponded to the first FSR of the mode cleaner resonator.

[29] using phase modulated sidebands at a frequency of 101 MHz that were generated by an EOM. After interacting with the nonlinear PPKTP crystal, the carrier (red solid line) as well as the squeezed vacuum (red dashed line) left the bow-tie resonator in reflection. To prevent damage of the homodyne detector photo diodes, the OMC ring resonator reflected the carrier light into a beam dump and transmitted the squeezed vacuum. Both, local oscillator and squeezed vacuum were superimposed on a 50/50 beam splitter. A homodyne detector with a bandwidth of 2 GHz and high-efficiency photo diodes was used to measure Kerr squeezing at sideband frequencies of 358.26 MHz (first FSR of the bow-tie resonator) and 1074.78 MHz (third FSR of the bow-tie resonator).

2.5.5 Kerr squeezing measurement at the first free spectral range of the bow-tie resonator

A first measurement was carried out to observe Kerr squeezing at a sideband frequency of 358.26 MHz. The temperature of the PPKTP crystal was tuned to 61.2 °C and the length of the bow-tie resonator was stabilized with the Pound-Drever-Hall technique in order to be resonant for the incident 1550 nm light. 85 mW s-polarized light were incident onto the bow-tie resonator. The carrier light as well as the squeezed vacuum emerged from the bow-tie resonator in reflection. The OMC for the separation of the bright carrier and

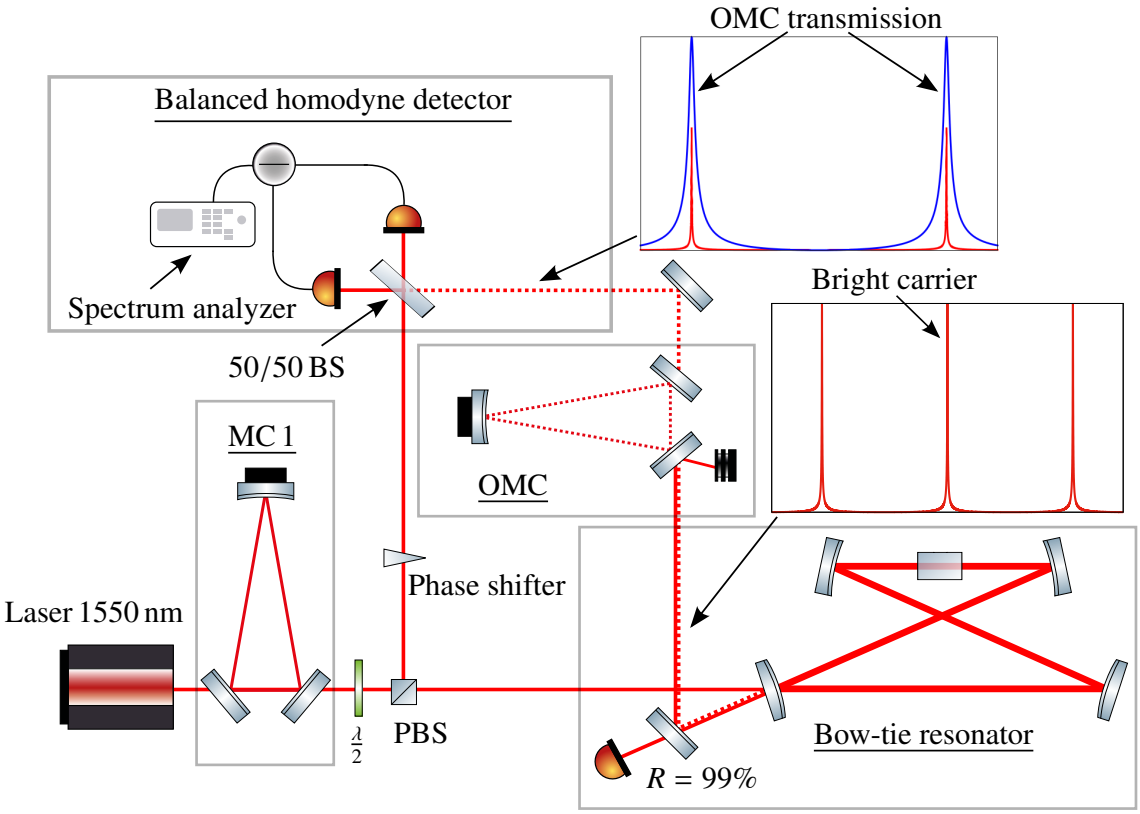

Figure 2.32: Schematic of the experimental setup for the generation of squeezed states via the cascaded optical Kerr effect. The laser light of the continuous-wave 1550 nm laser was spatially cleaned by the mode cleaner MC 1 which also acted as optical low pass on power and frequency noise. A combination of half-wave plate and polarization beam splitter (PBS) divided the laser power. One part served as local oscillator during the balanced homodyne detection, the other part acted as pump field for the bow-tie resonator. An electro-optical modulator imprinted phase modulated sidebands onto the laser light which were used to stabilize the bow-tie resonator length via the Pound-Drever-Hall technique to be resonant for the 1550 nm light. The bow-tie resonator produced squeezed vacuum (red dashed line) which left in reflection together with the bright carrier pump light (solid red line). In order to protect the photo diodes of the homodyne detector from damage, both fields were spatially separated by the OMC, which reflected the carrier light and transmitted the squeezed vacuum. The resonance peak in the middle of the red bow-tie transmission profile denotes the bright carrier light, which is suppressed by the blue transmission profile of the OMC. The transmitted squeezed vacuum was superimposed with a local oscillator on a 50/50 beam splitter and was measured with a homodyne detector.

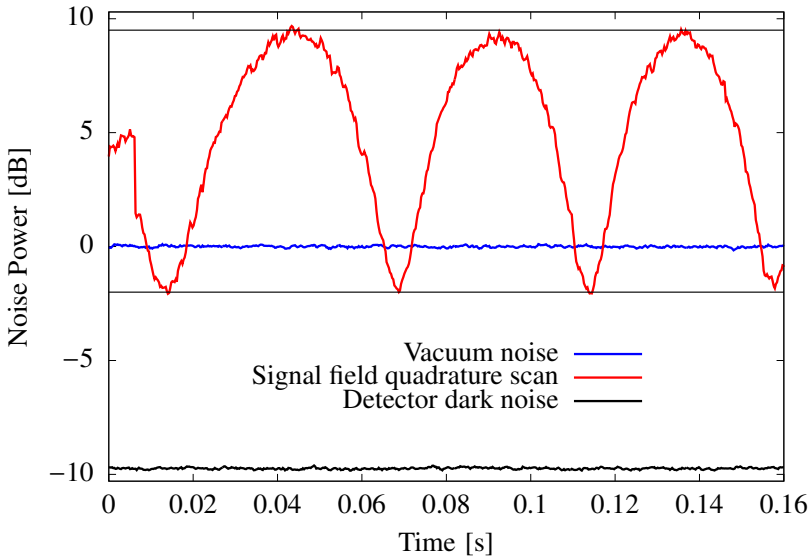

Figure 2.33: Kerr squeezing measurement at a sideband frequency of 358.26 MHz using 85 mW pump light at 1550 nm. A non-classical noise reduction of (-2.0 ± 0.1) dB below the vacuum noise was detected using 4 mW local oscillator power while the anti-squeezed variance was (9.5 ± 0.1) dB. During the measurement, a resolution bandwidth of 500 kHz and a video bandwidth of 200 Hz were used.

the squeezed sidebands was manually length-tuned until the carrier was reflected and the squeezed vacuum was transmitted. For the Kerr squeezing measurement, the balanced homodyne detection introduced in section 2.3.9 was employed. The variance of the signal field was evaluated by means of a zero-span measurement. Here, the spectrum analyzer detected the noise power of the signal field at a certain sideband frequency as a function of the measurement time. During the measurement, the phase between the signal field and the LO was scanned with a piezo-driven mirror which was located in the path of the LO field. Thus, the variance of the signal field in all quadratures was observed. Before the squeezing measurement, the signal path was blocked and the vacuum noise corresponding to 4 mW local oscillator power was recorded. It was normalized to 0 dB and is shown in figure 2.33 by the blue graph. After opening the signal path, the variance of the signal field oscillated between a squeezed variance of (-2.0 ± 0.1) dB and an anti-squeezed variance of (9.5 ± 0.1) dB, depicted by the red curve in figure 2.33, which was dark noise corrected and normalized to the vacuum. The distance between the detector dark noise and the vacuum noise was 9.7 dB. For the zero-span measurement, a resolution bandwidth of 500 kHz, a video bandwidth of 200 Hz and a measurement time of 0.165 s were used.
Based on the (anti-)squeezing values of (-2.0 ± 0.1) dB and (9.5 ± 0.1) dB, the total optical

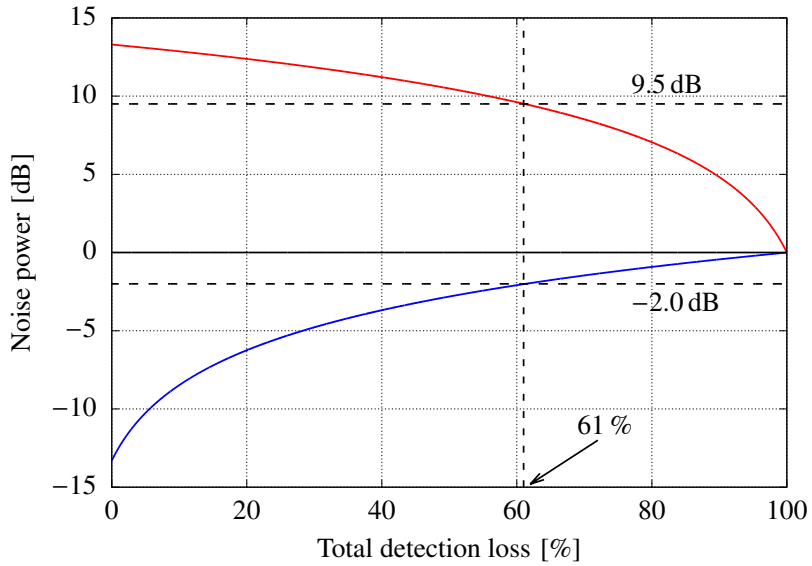

Figure 2.34: Simulated total optical loss for the squeezing measurement at 358.26 MHz. The observed squeezing value of (-2.0 ± 0.1) dB and the anti-squeezing value of (9.5 ± 0.1) dB correspond to a total loss of 61%. In this simulation, an initial loss-free (anti-)squeezing of ±13.3 dB was assumed.

loss that the signal field has experienced, can be estimated with equation (2.124). For the loss simulation initial loss-free (anti-)squeezing values of ±13.3 dB were assumed. Figure 2.34 shows both, squeezing (blue curve) and anti-squeezing (red curve) as a function of the optical loss. The measured values of (-2.0 ± 0.1) dB and (9.5 ± 0.1) dB correspond to a total optical loss of 61% or an overall detection efficiency of $\eta_{\text{tot}} = 0.39$. The following list provides an overview about the different loss sources of the experimental setup and estimates their contribution to the total optical loss.

1. **Bow-tie resonator:**
   The escape efficiency of the bow-tie resonator is given by [79]

$$\eta_{esc} = \frac{T_1}{T_1 + L}, \tag{2.129}$$

   where T_1 is the transmission of the coupling mirror and L are the round-trip losses (excluding T_1). The design value of the bow-tie resoantor coupling mirror was $T_1 = 0.01$ at 1550 nm. To estimate the residual round-trip losses, the reflectivity of the coupling mirror was fixed to the design value of $R_1 = 1 - T_1 = 0.99$ and a two-mirror resonator was simulated using a second mirror with an effective reflectivity of $R_2 = 0.9983$. This resonator reproduced the measured signal in reflection on

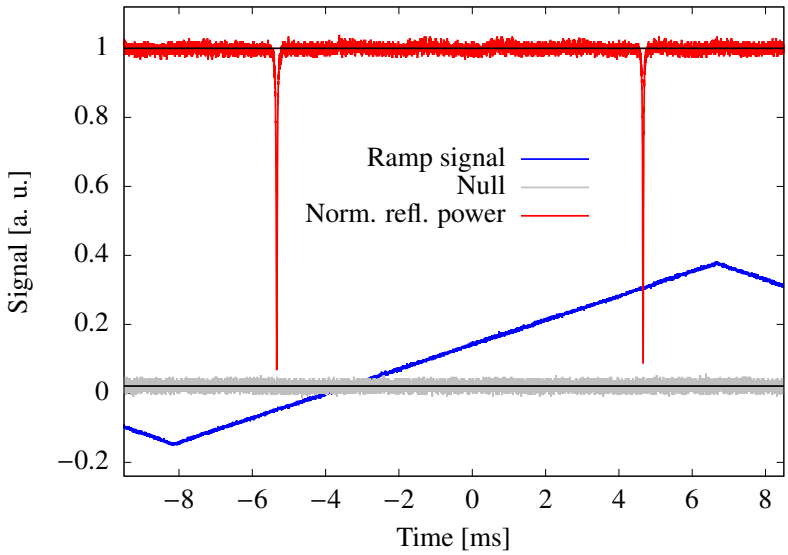

Figure 2.35: Normalized reflected power from OMC. The OMC ring resonator that was employed for separation of the bright carrier light and the squeezed sidebands reflected on resonance 6 % of the incident light power. The squeezed light experienced the same amount of loss.

resonance, where about 50.6 % of the injected light power got reflected. Thus, the round-trip losses were $L = 1 - R_2 = 0.0017$, resulting in an escape efficiency of

$$\eta_{\mathrm{esc}} \approx 0.85. \tag{2.130}$$

The largest contribution to the round-trip loss was residual conversion to the second harmonic light. Other loss sources were transmission and scattering at the bow-tie mirrors M_2, M_3 and M_4 and scattering and absorption of the PPKTP crystal. The latter was measured to be (84 ± 40) ppm/cm [76]. The power reflectivities $R_1 = 0.99$ and $R_2 = 0.9983$ resulted in a FWHM of 652 kHz and a finesse of about 549.

2. **OMC resonator**:

   The OMC ring resonator that was used to separate the carrier light and the squeezed vacuum also contributed to the overall optical loss. On resonance, it reflected 6 % of the injected light power due to mode mismatch (2 %) and because of impedance mismatch (4 %). This is depicted in figure 2.35. The squeezed sidebands experienced the same amount of loss. Another loss source was the non perfect matching of the FSRs of the bow-tie resonator and the OMC. This loss was simulated to be 3 %. Thus, the detection efficiency of the OMC was

$$\eta_{\mathrm{OMC}} \approx 0.91. \tag{2.131}$$

3. **Homodyne efficiency:**
   For the squeezing measurement with the balanced homodyne detection, both, signal field and local oscillator were spatially overlapped on a 50/50 beam splitter. The quality of the overlap is described by their interference. To determine the quality of their interference, a bright auxiliary field was superimposed with the local oscillator on the 50/50 beam splitter. Both fields had the same light power, polarization and almost the same spatial shape. The relative phase between both fields was periodically changed by a piezo-actuated mirror and the signal in one output port of the 50/50 beam splitter was monitored. A single photo diode measured a sinusoidal interference pattern which had the maximum and minimum intensities $I_{\max}$ and $I_{\min}$. The quality of the interference between signal field and local oscillator was determined by calculating the interference contrast ([78], p. 48)

$$K = \frac{I_{\max} - I_{\min}}{I_{\max} + I_{\min}} = 0.986. \tag{2.132}$$

   The homodyne efficiency is given by the square of the interference contrast

$$\eta_K = K^2 \approx 0.97, \tag{2.133}$$

   leading to a loss of 3 %.

4. **Quantum efficiency:**
   Another contribution to the total loss is given by the quantum efficiency of the homodyne detector's photo diodes. The quantum efficiency η_{QE} of a photo diode is a quantity which describes the probability that the incident light is transformed into a detectable signal. A single photon is absorbed by the active area of the photo diode. If its energy $E = hf$ is larger than the binding energy of an electron, an electron is excited from the valance to the conduction band. Thus, a photo current can be measured. The quantum efficiency can be computed with the equation [61]

$$\eta_{\mathrm{QE}} = R_\lambda \frac{hc}{\lambda e}. \tag{2.134}$$

   $R_\lambda = I_{\mathrm{p}}/P$ is the so-called responsivity of a photo-diode at a wavelength λ. It is the ratio of the photo current I_{p} that is measured when light with power P is incident onto the photo diode. h is the Planck constant, c the speed of light in vacuum, λ the laser wavelength in nm and e is the electron charge. By measuring the incident light power P and the corresponding photo current I_{p}, the quantum efficiency of our custom made photo diodes was estimated to

$$\eta_{\mathrm{QE}} \approx 0.94. \tag{2.135}$$

5. **Residual losses:**
   The remaining losses were about 44.7 %, resulting in an escape efficiency of

$$\eta_{\text{res}} \approx 0.553. \tag{2.136}$$

   These residual losses included optical round-trip losses due to scattering and absorption on mirrors and lenses. However, their loss contribution of about 10 % cannot explain the remaining losses completely. The maximum amount of measurable squeezing is not only limited by optical losses, but also by phase noise. In homodyne detection, the quadrature in which the squeezing is measured is determined by the relative phase between the LO and the signal field. If the period of the phase fluctuation is shorter than the time the spectrum analyzer needs to measure a single data point, than the squeezing measurement will not only be a measurement of one quadrature angle ϑ, rather of a range of quadrature angles $\vartheta \pm \delta\vartheta$ ([86], pp. $41-43$), as shown in figure 2.36 for an amplitude quadrature squeezed vacuum state. Part a.) of this figure shows a normal squeezing measurement without phase noise. Part b.) visualizes the case of phase noise. The change in the readout quadrature leads to a coupling from the anti-squeezed quadrature into the detected squeezing. Thus, the observed squeezing value is decreased. This phase noise can occur due to mirror motions. Since the mirrors of the bow-tie squeezing resonator were placed in mounts that were screwed to a large aluminum spacer, they were exposed to acoustically-induced vibrations. These vibrations of the mirrors could led to phase noise.

All loss contributions are summarized in table (2.1).
Furthermore, the linearity of the employed GHz-bandwidth homodyne detector was investigated. The measurement is shown in appendix A. A local oscillator power of 2 mW was incident onto the homodyne detector and the difference photo current was evaluated with a spectrum analyzer, while the signal input was blocked. Then, the light power was doubled to 4 mW and the spectrum of the difference photo current was recorded again. The measured increase of the noise power level was 3 dB, which demonstrated that the measurement was vacuum noise limited. Also, the linear performance of the homodyne detector was shown.

2.5.6 Experimental confirmation of Kerr squeezing

To verify that the observed squeezing at the fundamental wavelength of 1550 nm was generated by the cascaded Kerr effect, a differentiation from squeezing of the fundamental field

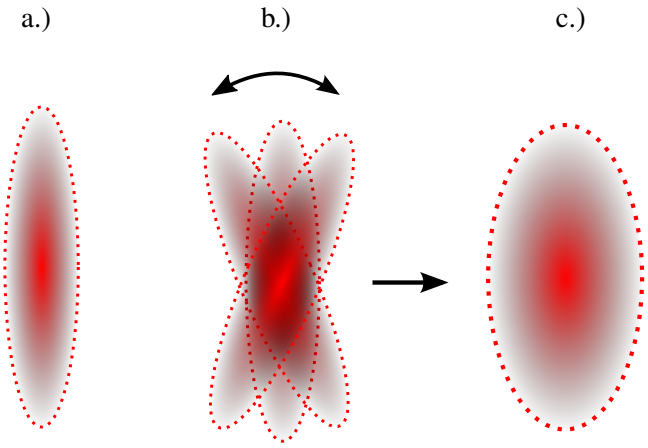

Figure 2.36: Effect of phase noise on an amplitude quadrature squeezed vacuum state. a.) shows the state without phase noise. Here, a squeezing measurement corresponds to the true squeezing value. b.) depicts the case of phase noise. Due to the fluctuation of the squeezing ellipse, the read-out quadrature changes during the measurement process. Thus, a part of the anti-squeezed quadrature is coupled to the squeezed quadrature, resulting in a decreased observed squeezing strength, which is depicted in figure c.).

Contribution	1-Loss
Bow-tie resonator	0.85
OMC	0.91
Contrast BHD	0.97
PD quantum efficiency	0.94
Residual	0.553
Total	0.39

Table 2.1: List of the optical loss contributions for the Kerr squeezing measurement at a sideband frequency of 358.26 MHz, calculated as detection efficiencies. The product of all efficiencies leads to the total detection efficiency of 0.39.

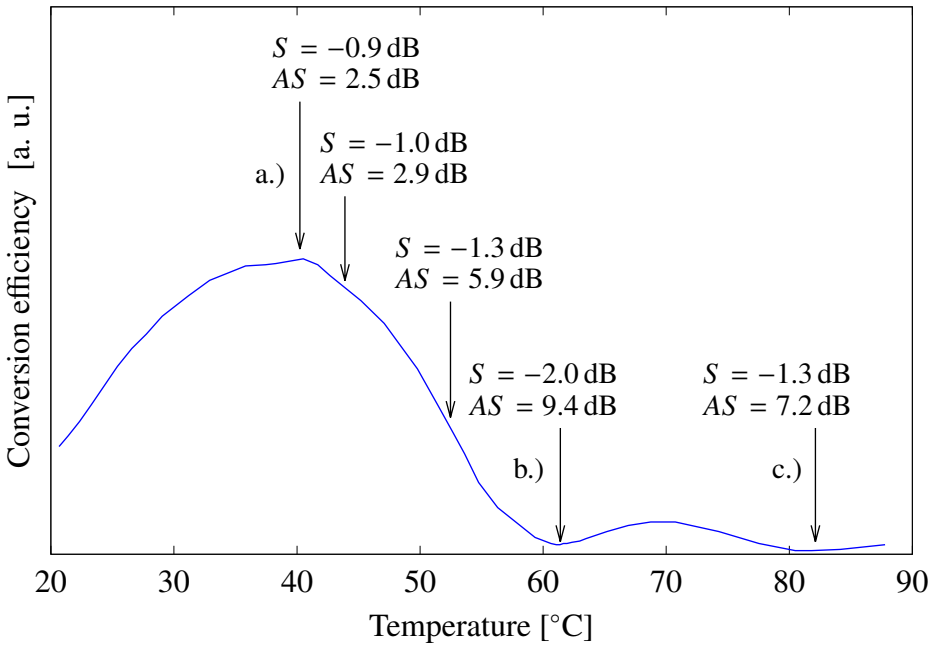

Figure 2.37: Confirmation of Kerr squeezing. As predicted by theory, the squeezing produced by the cascaded Kerr effect shows a maximum of −2.0 dB in the first SHG conversion minimum at 61.2 °C (denoted by b.)) and decreases in the second minimum at 81.8 °C to −1.3 dB (labeled c.)). The occurrence of the Kerr-induced resonance peak deformation was observed in both minima. On the contrary, no resonance peak deformation was monitored in the SHG conversion maximum at 40.5 °C (denoted by a.)). Therefore, the detected squeezing of −0.9 dB was produced by the SHG process. All measurements were performed at a sideband frequency of 358.26 MHz.

caused by the SHG process (see section 2.3.7) was necessary. As derived by Li and Kumar [53], the squeezing of the fundamental wavelength in the SHG conversion maximum is only produced by the SHG process. The nonlinear phase shift vanishes (see equation 2.12) and consequently no squeezing is produced by means of the cascaded Kerr effect in the SHG conversion maximum. As shown in figure 2.14, the squeezing of the fundamental field decreases with lower SHG conversion efficiencies (larger wave vector mismatch) For wave-vector mismatches $\Delta k \neq 0$, the nonlinear phase shift starts to build up and exhibits a maximum in the first SHG conversion minimum. It decreases in higher order SHG conversion minima. However, Li and Kumar assumed a non-poled single crystal in their considerations. References [55] and [59] extended them to be valid for periodically poled second-order nonlinear media. Maeda et al. calculated, that in case of perfect quasi-phase matching, the SHG process yields to squeezing of the fundamental field. Arbitrary high squeezing values can be achieved, using sufficiently high fundamental pump powers. This squeezing mechanism disappears for large phase mismatch [55]. Noirie et al. [59] have shown, that the squeezing of the fundamental field in a periodically poled quasi-phase mismatched medium is caused by its intensity-dependent phase shift. This effect vanishes in the conversion maximum.

To validate that the measured squeezing was generated by the cascaded Kerr effect, several squeezing measurements at different temperatures of the PPKTP crystal, corresponding to different wave-vector mismatches Δk, were performed using a 1550 nm pump power of 85 mW. This is illustrated in figure 2.37. In the SHG conversion maximum at 40.5 °C, squeezing and anti-squeezing of (-0.9 ± 0.1) dB and (2.5 ± 0.1) dB were detected (labeled with a.)). As depicted in figure 2.25, no resonance peak deformation due to the nonlinear phase shift occurred. Thus, it can be concluded that the squeezing in the SHG conversion maximum was produced by the SHG process and not by the cascaded Kerr effect. In the first SHG conversion minimum at 61.2 °C, a squeezing of (-2.0 ± 0.1) dB and an anti-squeezing of (9.4 ± 0.1) dB were observed, labeled with b.) in figure 2.37. As shown in figure 2.25, the measured resonance peak displayed a deformation due to the nonlinear phase shift of the cascaded Kerr effect. Consequently, the squeezing measured at 61.2 °C was produced by the cascaded Kerr effect. As described by equation (2.14), the Kerr-induced intensity-dependent phase shift decreases in higher-order conversion minima. Thus, also the observed squeezing should be smaller than in the first conversion minimum. This was experimentally confirmed by a squeezing measurement in the second conversion minimum at 81.8 °C. A squeezing value of (-1.3 ± 0.1) dB and an anti-squeezing value of (7.2 ± 0.1) dB were detected (labeled with c.)). Additionally, the Kerr-induced resonance

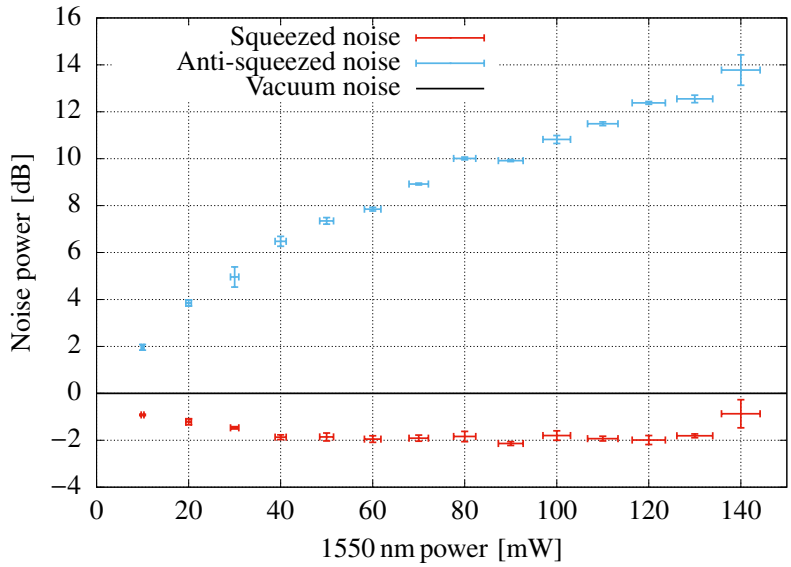

Figure 2.38: Kerr anti-squeezed and squeezed noise as a function of the fundamental pump power at a sideband frequency of 358.26 MHz. A maximum squeezed variance of (2.1 ± 0.1) dB below the vacuum noise level was detected with a fundamental power of 90 mW. Due to phase noise and optical losses, no stronger non-classical noise reduction could be achieved. The maximal anti-squeezed variance of (13.8 ± 0.7) dB was measured for a pump power of 140 mW.

peak deformation was also observed in the second conversion minimum. All squeezing measurements were performed at a sideband frequency of 358.26 MHz.

2.5.7 Kerr squeezing as a function of the fundamental pump power

To further characterize the bow-tie squeezing resonator, squeezing measurements in the first conversion minimum at 61.2 °C were performed as a function of the fundamental 1550 nm pump power. This is depicted in figure 2.38 for a sideband frequency of 358.26 MHz. The pump power was varied within the range between 10 mW and 140 mW and for each pump power value, a zero-span measurement was performed. The largest value of the squeezed quadrature of (2.1 ± 0.1) dB was measured with a pump power of 90 mW. Due to phase noise and optical losses, no larger non-classical noise reduction below the vacuum noise level could be detected. The largest anti-squeezed variance of (13.8 ± 0.7) dB was observed for a pump power of 140 mW.

A similar measurement was performed at a sideband frequency of 1074.78 MHz using again pump powers between 10 mW and 140 mW and a crystal temperature of 61.2 °C. A maximum non-classical noise reduction below the vacuum noise level of (2.5 ± 0.1) dB

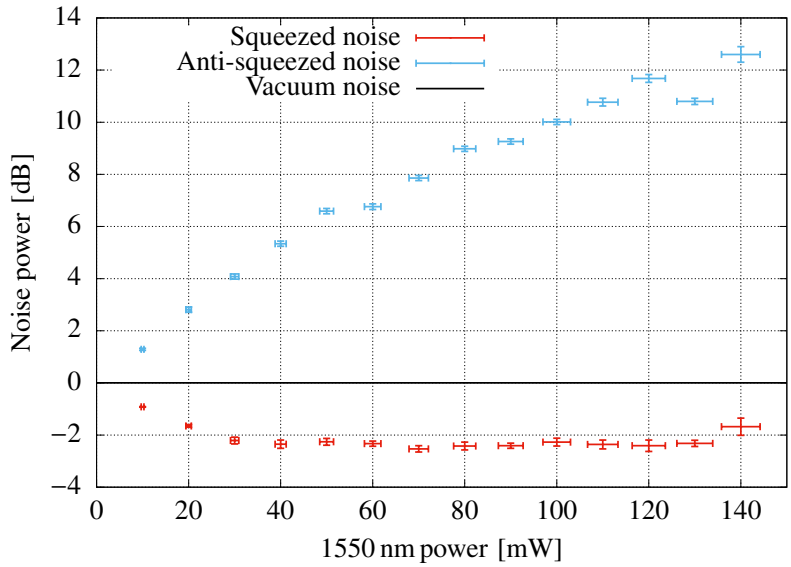

Figure 2.39: Kerr anti-squeezed and squeezed noise as a function of the fundamental pump power at a sideband frequency of 1074.78 MHz. A maximum squeezed variance of (2.5 ± 0.1) dB below the vacuum noise level was detected with a fundamental power of 70 mW. The largest anti-squeezed variance of (12.6 ± 0.3) dB was measured with a pump power of 140 mW.

was observed for a fundamental pump power of 70 mW (see figure 2.40) and (2.4 ± 0.2) dB were measured using a pump power of 120 mW. The largest detected anti-squeezed variance of (12.6 ± 0.3) dB was measured with a pump power of 140 mW. The reason for the slightly increased squeezing values measured at 1074.78 MHz was probably less phase noise or less SHG conversion in the bow-tie resonator.

2.6 Summary and conclusion

In this chapter, the first generation of squeezed vacuum states by means of the second-order cascaded optical Kerr effect, using continuous-wave laser light is demonstrated. The squeezed vacuum states were generated at a wavelength of 1550 nm with a four-mirror bow-tie resonator that contained a PPKTP crystal. First, the conversion from the fundamental 1550 nm light to the SHG light was measured and two conversion minima at 61.2 °C and 82.8 °C were detected. The occurrence of the cascaded optical Kerr effect was observed in both SHG conversion minima by measuring the deformed resonance peaks in transmission of the bow-tie resonator. To exclude a thermally-induced resonance peak deformation, the resonance of the bow-tie cavity was scanned in times of 3.7 μs and 5.5 μs. During these

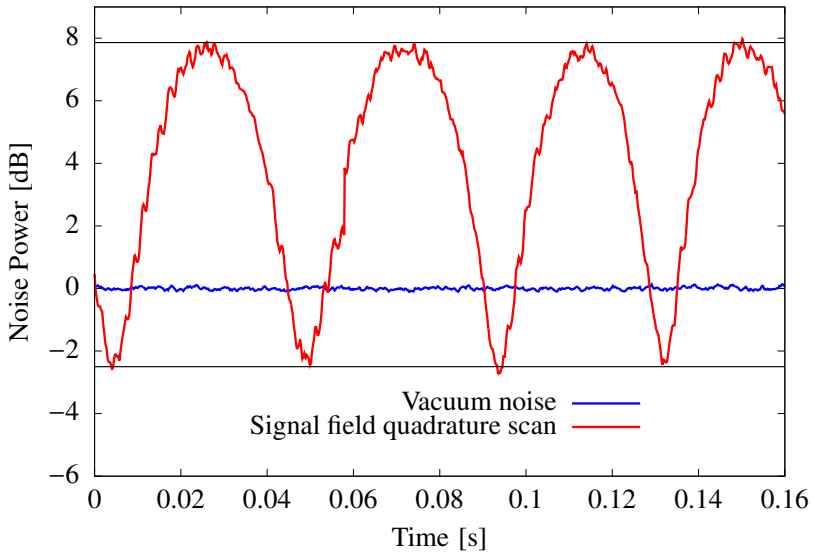

Figure 2.40: Kerr squeezing measurement at a sideband frequency of 1074.78 MHz using 70 mW pump light. A non-classical noise reduction of (2.5 ± 0.1) dB below the vacuum noise was detected using 4 mW local oscillator power. The anti-squeezed variance was (7.8 ± 0.1) dB. During the measurement, a resolution bandwidth of 500 kHz and a video bandwidth of 200 Hz were used.

fast scans, the resonance peak deformation maintained and thus, was not caused by thermal effects. Furthermore the dependence of the resonance peak deformation on the fundamental pump power was observed, using light powers between 77.8 mW and 102. mW. For larger light power, the resonance peak deformation increased. A non-classical noise reduction below the vacuum noise of (2.0 ± 0.1) dB at a sideband frequency of 358.26 MHz was detected in the first SHG conversion minimum using 85 mW pump power. A squeezed variance of (2.5 ± 0.1) dB was observed at a sideband frequency of 1074.78 MHz with a pump power of 70 mW. The main reasons that prevented the measurement of larger squeezing values were phase noise and optical losses. Phase noise was mainly caused by the acoustically-induced motion of the bow-tie resonator mirrors. To decrease phase noise in future experiments, the Kerr-squeezing resonator should be placed on a damping stage and should be operated under vacuum. The optical losses can be reduced by using superpolished optics, by increasing the interference contrast at the homodyne detector and by an even better matching of the bow-tie resonator and the OMC FSRs. However, observed anti-squeezing values of up to (13.8 ± 0.7) dB at 358.26 MHz demonstrate that the cascaded optical Kerr effect is a promising process for the generation of squeezed vacuum states.

Chapter 3

Absorption measurements on AlGaAs coatings at 1064 nm and 1550 nm

3.1 Introduction

According to Einsteins theory of general relativity, mass distributions induce the curvature of space time. An accelerated motion of a mass will cause ripples in the curvature of space time, which propagate with the velocity of light, the so called gravitational waves. Gravitational waves are transverse quadrupole waves, which have two kinds of polarizations, denoted by '+' and '×', and a period of T_{gw} ([6], p. 122). They expand and compress the space time perpendicular to their propagation direction and thus, act as a tidal force. Figure 3.1 shows this effect for a ring of free falling test masses for both polarizations for a gravitational wave, moving into the plane of the paper. If the distance between two test masses is l, a gravitational wave will cause a change of δl. On earth, the expected relative length changes $h = 2\delta l/l$ [13], also called strain, are in the order of up to $\sim 10^{-21}$. These relative length changes are caused by extremely energetic cosmic events, such as the merging of two black holes or two neutron stars ([15], pp. 26 – 29).

An appropriate measurement device for detecting small relative length changes between free falling test masses is a Michelson interferometer [13], which is depicted in figure 3.2. In its simplest version, it consists only of a 50/50 beam splitter and two end mirrors, named $\mathrm{ETM_N}$ and $\mathrm{ETM_E}$. A laser beam impinges on the 50/50 beam splitter and is divided into two beams. One beam propagates along the north arm and gets reflected back by the end test mass $\mathrm{ETM_N}$. The other beam propagates in direction of the east arm and is reflected back by test mass $\mathrm{ETM_E}$. Both beams are recombined at the beam splitter and their interference pattern is observed at the interferometer's output with the photo diode $\mathrm{PD_S}$. A gravitational wave with '+' polarization, propagating into the plane of the paper, alters

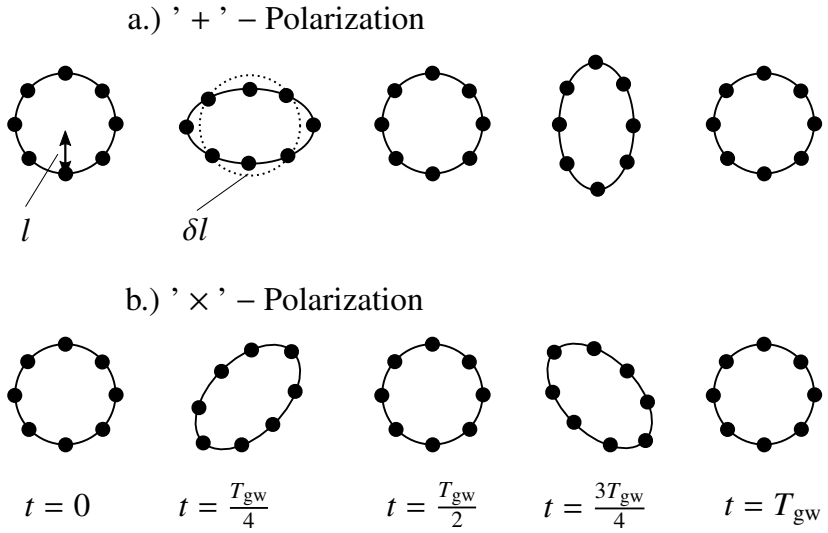

Figure 3.1: Effect of a gravitational wave moving into the plane of the paper on a ring of free falling test masses. A gravitational wave expands and compresses the space time perpendicular to its direction of propagation and acts as a tidal force. a.) depicts the effect of a gravitational wave for the '+'-polarization while b.) shows the impact of the '×'-polarization. Adapted from ([6], p. 122).

the distance between the beam splitter and the end test masses in both orthogonal interferometer arms by the same amount δl, but with different sign [13]. Both beams acquire a differential phase shift, resulting in a change of the detected intensity at PD_S.

To increase the signal-to-noise ratio and to minimize the relative shot noise (([15], p. 294), high circulating light power in the interferometer is required. It can be obtained by using the technique of power-recycling ([15], pp. 70 – 72). During its operation, the interferometers south port is almost kept dark and the light returns to the laser, the interferometer acts as a mirror. Placing a power-recycling mirror (PRM) at the west port forms an effective two-mirror cavity and almost the full light is reflected back into the interferometer and a high circulating light power is achieved.

A gravitational wave induces a phase modulation onto the circulating light and consequently, sidebands are created. While the carrier light is reflected towards the west interferometer port, the sidebands propagate to the south port. A signal-recycling mirror (SRM) placed at the south port forms a signal-recycling cavity with the rest of the interferometer and amplifies the generated sidebands ([15], pp. 73 – 78). Thus, the sensitivity of the gravitational-wave detector can be enhanced in a certain and tunable frequency range.

To increase the interaction time of the light and the gravitational wave and thus, to increase the gained phase shift ([15], pp. 67 – 68), both interferometer arms have implemented arm

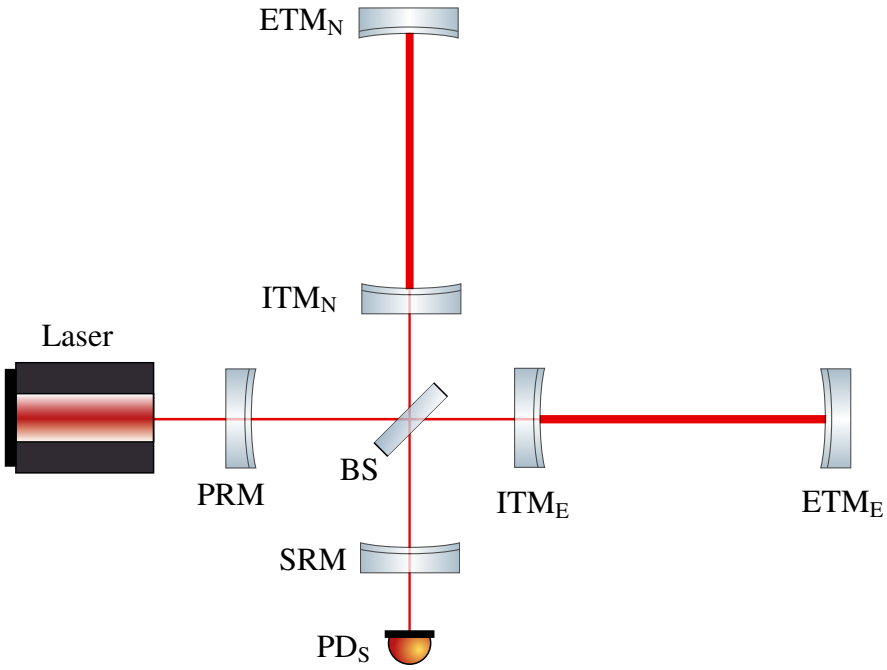

Figure 3.2: Dual-recycled Michelson interferometer with arm cavities. The Michelson interferometer's south port is almost kept dark and nearly the full light power is reflected back towards the west port. The power-recycling mirror (PRM), positioned at the west port, reflects the power back into the interferometer. The power-recycling technique is used to reduce the relative-shot noise and thus, to increase the signal-to-noise ratio. Placing a signal-recycling mirror at the south port of the interferometer leads to an enhancement of the sidebands, induced by the gravitational wave. To enlarge the interaction time between the light and the gravitation wave, resonators in both interferometer arms are implemented. Adapted from ([15], p. 11).

resonators. They are formed between the input test masses (ITM) and the end test masses (ETM).

On 14th September 2015, the first gravitational wave was measured by the two detectors of the Advanced Laser Interferometer Gravitational Wave Observatory (Advanced LIGO). The gravitational wave was caused by the inspiral and merger of two black holes as well as by the ring down of the final single black hole. The initial black holes had masses of 36 and 29 times the solar mass. The final black hole mass corresponded to 62 times the solar mass and a gravitational wave with the energy of 3 solar masses was radiated. The observed gravitational wave signal had a maximum strain of $1.0 \cdot 10^{-21}$ and swept within a frequency range between 35 and 250 Hz [3]. Further detections of gravitational waves produced during the coalescence of two black holes are described in [1, 2, 30]. The first three-detector observation (two Advanced LIGO detectors and the Advanced VIRGO detector) of a bi-

nary black hole merger improved the localization of the gravitational-wave source in the sky [4]. The first detection of a gravitational wave generated during a binary neutron star merger, was achieved on the 17th August 2017. This observation was supported by the 'Gamma-ray Burst Monitor' of the Fermi satellite, which measured a gamma-ray burst two seconds after the gravitational wave [5].

The limiting noise source of state of the art gravitational-wave detectors like Advanced LIGO within the frequency range between 30 Hz and 100 Hz is coating thermal noise [63]. Coating thermal noise is caused by the motion of the thermally excited atoms of the mirror surface. Their averaged motion results in a displacement noise that is detected by the laser beam and consequently, can mimic a gravitational wave. The coatings used on the input and end test masses of Advanced LIGO are ion-beam sputtered dielectric multilayer coatings. They consist of thickness-optimized alternating quarter-wave layers of low-index silica (SiO_2) and high-index tantalum pentoxide (TaO_5). The latter is doped with 25 % titanium dioxide, to reduce coating thermal noise. While they show superb optical qualities such as low absorption loss (0.5 ppm) and low scatter loss ($\sim$ 20 ppm), their Brownian motion is a limiting noise source [23]. Origin of the Brownian motion is in the large mechanical loss ($3 \cdot 10^{-4}$ to $4 \cdot 10^{-4}$) of the high-index tantalum pentoxide layers ([15], p. 242). The frequency dependent displacement power spectral density of coating thermal noise is given by ([38], p. 38)

$$S_x(f) = \frac{2k_B T}{\pi^2 f Y} \frac{d}{w_m^2} \left(\frac{Y'}{Y} \Phi_{\parallel} + \frac{Y}{Y'} \Phi_{\perp} \right). \tag{3.1}$$

Here k_B is Boltzmann's constant, T is the temperature, d is the coating thickness, f is the frequency, Y is Young's modulus of the mirror substrate, Y' is Young's modulus of the coating and w_m is the radius of the laser beam, impinging on the mirror coating. $\Phi_{\parallel}$ and $\Phi_{\perp}$ are the values of the coating mechanical loss angle parallel and orthogonal to the coating surface. They depend on the thicknesses, mechanical losses and on the Young's modulus of both employed coating materials. To decrease the coating thermal noise, a mirror can be cooled down to cryogenic temperatures [33], larger laser beam sizes or different beam shapes can be employed, ([38], pp. 196 – 215), or the coating thickness can be optimized [63].

3.2 AlGaAs coatings

An alternative approach to reduce coating Brownian noise is the use of crystalline AlGaAs coatings. It was experimentally shown, that these coatings yield to a reduction of coating thermal noise by a factor of ten within the frequency range between 1 Hz and 100 Hz

a.) 1064 nm

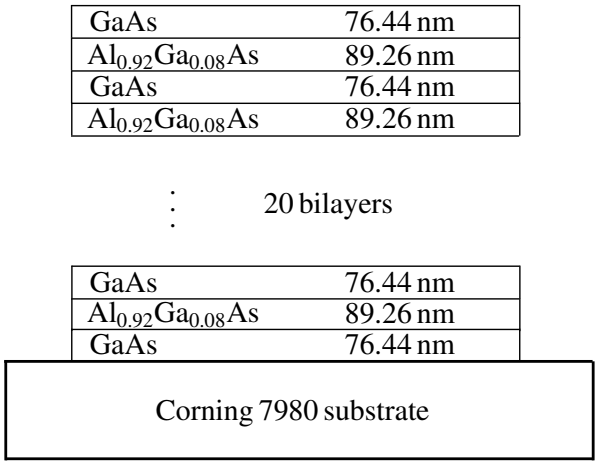

b.) 1550 nm

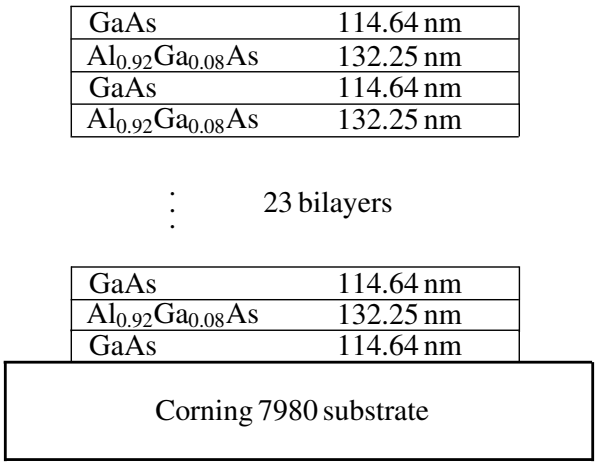

Figure 3.3: Design of the AlGaAs coatings with a power reflectivity of (99.96 ± 0.01) %. As shown in a.), the AlGaAs coating at 1064 nm consisted of 23.5 bilayers, made of the high-index GaAs and the low-index $Al_{0.92}Ga_{0.08}As$. The quarter-wave GaAs layers had a geometrical thickness of 76.44 nm and the quarter-wave $Al_{0.92}Ga_{0.08}As$ layers were 89.26 nm thick, resulting in a total coating thickness of 3.9 μm. The AlGaAs coating specified for a center wavelength of 1550 nm was made of 26.5 bilayers. The quarter-wave GaAs layers were 114.64 nm thick and the quarter-wave $Al_{0.92}Ga_{0.08}As$ layers had a thickness of 132.25 nm. Both coatings were bonded to a Corning 7980 substrate.

[26]. AlGaAs coatings consist of alternating quarter-wave gallium arsenide (GaAs) and aluminum gallium arsenide ($Al_xGa_{1-x}As$), layers. Here, x denotes the aluminum contribution with $0 \leq x \leq 1$ and is set to 0.92 [26]. GaAs is the high-index material ($n_{GaAs} = 3.48$ [26]) and $Al_{0.92}Ga_{0.08}As$ is the low-index material ($n_{Al_{0.92}Ga_{0.08}As} = 2.977$ [26]).
As shown in the next section, optical absorption of multilayer coatings is a crucial parameter in high-power laser applications like gravitational-wave detectors. Thus, the goal of this work was to measure the optical absorption of AlGaAs coatings at 1064 nm and 1550 nm. The investigated coatings at both wavelengths had a design power reflectivity of (99.96 ± 0.01) %. The coating for the absorption measurement at 1064 nm was made of 23.5 $GaAs/Al_{0.92}Ga_{0.08}As$ bilayers, resulting in a total geometrical thickness of 3.9 μm (see figure 3.3a). The AlGaAs coating specified for 1550 nm consisted of 26.5 bilayers, yielding to a total geometrical thickness of 6.5 μm (see figure 3.3b). Each coating was bonded to a mirror substrate fabricated of Corning 7980 glass. The AlGaAs coatings had a diameter of 8 mm. The substrate had a thickness of $L_s = 6.35$ mm and a radius of $R_s = 12.7$ mm. Both AlGaAs coatings were manufactured in 2014 by the company 'Crystalline Mirror Solutions'.

3.3 Thermal effects due to coating absorption

3.3.1 Thermal effects in optical resonators

An optical two-mirror resonator, as shown in figure 3.4, consists of the mirrors M_1 and M_2 that are separated by the geometrical distance L. In an ideal and stable resonator, the wave front curvature of an injected Gaussian beam matches the radii of curvature of mirrors ρ_1 and ρ_2 at their geometric positions along the optical axis. In this case, the Gaussian beam is reflected back on itself with an inverted wavefront curvature. In order to define a stability criterion for optical resonators, the g-parameters ([73], p. 746)

$$g_1 = 1 - \frac{L}{\rho_1} \tag{3.2}$$

and

$$g_2 = 1 - \frac{L}{\rho_2} \tag{3.3}$$

are used. An optical resonator is stable, if the g-parameters satisfy ([73], p. 747)

$$0 \leq g_1 g_2 \leq 1. \tag{3.4}$$

The resonator waist size w_0 as well as the waist sizes w_1 and w_2 at the mirror positions z_1 and z_2 are defined with the g-parameters ([73], p. 747)

$$w_0 = \left(\frac{L\lambda}{\pi} \sqrt{\frac{g_1 g_2 (1 - g_1 g_2)}{(g_1 + g_2 - 2g_1 g_2)^2}} \right)^{1/2} \tag{3.5}$$

$$w_1 = \left(\frac{L\lambda}{\pi} \sqrt{\frac{g_2}{g_1 (1 - g_1 g_2)}} \right)^{1/2} \tag{3.6}$$

$$w_2 = \left(\frac{L\lambda}{\pi} \sqrt{\frac{g_1}{g_2 (1 - g_1 g_2)}} \right)^{1/2} \tag{3.7}$$

$$z_1 = \frac{g_2 (1 - g_1)}{g_1 + g_2 - 2g_1 g_2} L \tag{3.8}$$

$$z_2 = \frac{g_1 (1 - g_2)}{g_1 + g_2 - 2g_1 g_2} L. \tag{3.9}$$

A change of the radii of curvature ρ_1 and ρ_2 or the geometrical mirror spacing L modifies the g-parameters. This yields to a transformation of w_0, w_1, w_2, z_1 and z_2 and thus, to a change of the resonator eigenmode. Furthermore, the g-parameters determine the Guoy phase shift of the different Hermite-Gaussian TEM_{mn} modes of the order (m,n) ([73], p. 762)

$$\Psi_{\mathrm{guoy}} = (n + m + 1) \cos^{-1} \left(\sqrt{g_1 g_2} \right) \tag{3.10}$$

within one FSR and thus, the mode spacing of an optical resonator.

Now, thermal effects in an optical two-mirror resonator due to absorption of light power taking place in the mirror coatings will be explained. The black resonator mode in figure 3.4 depicts the cold resonator eigenmode with beam waist $w_{0,\,\mathrm{cold}}$, where no laser light is injected and absorbed. In the case of a circulating intra-cavity field, the mirror coatings of M_1 and M_2 absorb a small part of the light power. The dissipated light power is transformed into heat and transferred to the mirror substrates. Due to the Gaussian intensity distribution of the laser beam, the resulting temperature distributions inside of the mirror substrates are non-uniform, exhibiting a maximum at the optical axis. The induced temperature distributions result in two effects. First, they cause a non-uniform thermal expansion of the mirror substrates. In the case of two concave mirrors, their radii of curvature are decreased, yielding to an increase of the g-factors, given by equations (3.2) and (3.3). The blue resonator mode in figure 3.4 depicts the corresponding hot resonator eigenmode. Compared to the beam waist $w_{0,\,\mathrm{cold}}$ of the cold resonator mode, the waist size of the hot eigenmode $w_{0,\,\mathrm{hot}}$

is increased. Furthermore, the diameter of the resonator mode at the positions z_1 and z_2 of the mirror surfaces, determined by equations (3.6) and (3.10), is decreased ([17], pp. 145 – 147). Second, the non-uniform temperature distribution inside of the substrate of the in-coupling mirror M_1 will result in an index of refraction gradient because of $\beta = dn/dT$. The laser beam coupled into the resonator has to pass the mirror substrate M_1 and gets dephased by the refractive index profile. The temperature rise and thus, the refractive index change has its maximum value at the optical axis for positive β. Consequently, the phase delay peaks at the optical axis, and drops at the outer regions (in radial direction) [92]. Thus, the refractive index gradient can approximately be modeled by a spherical lens which alters the spatial shape of the in-coupled laser mode. This process is called thermal lensing and is illustrated by the red resonator mode in figure 3.4. The spatial shape of the incoming Gaussian laser beam propagating through the thermal lens is altered and does not match the resonator eigenmode anymore. Consequently, a (small) part of the incoming light is scattered from the fundamental TEM_{00} mode into higher-order modes. These higher-order modes are reflected off the resonator, decreasing the power coupling of the incident laser beam into the resonator ([15], pp. 267 – 268).

3.3.2 Thermal effects in gravitational wave detectors

In Advanced LIGO, the light power stored in the arm cavities will reach up to 800 kW [23] at full design power. Because of the non-vanishing coating absorptions of the ITMs and ETMs (see figure 3.2), a part of the circulating light power will be absorbed. Thus, thermal expansion changes the radii of curvature of the ITM and ETM substrates, resulting in altered cavity modes of both arm resonators. The induced thermal lenses in both ITM substrates have the strongest effect on the interferometer operation. They modify the spatial shape of the laser beam injected into the arm resonators and thus, the power coupling between the power-recycling cavity and the arm resonators is decreased. This reduces the light power circulating inside of the arm resonators and consequently also the detector sensitivity. Different thermally-induced wave-front deformations of the laser beams returning from the interferometer arms also reduce the interference contrast at the beam splitter and a part of the light leaves the interferometer in direction of the dark (south) port and is lost. To control thermal effects, gravitational-wave detectors like Advanced LIGO employ thermal compensation systems [10, 64].

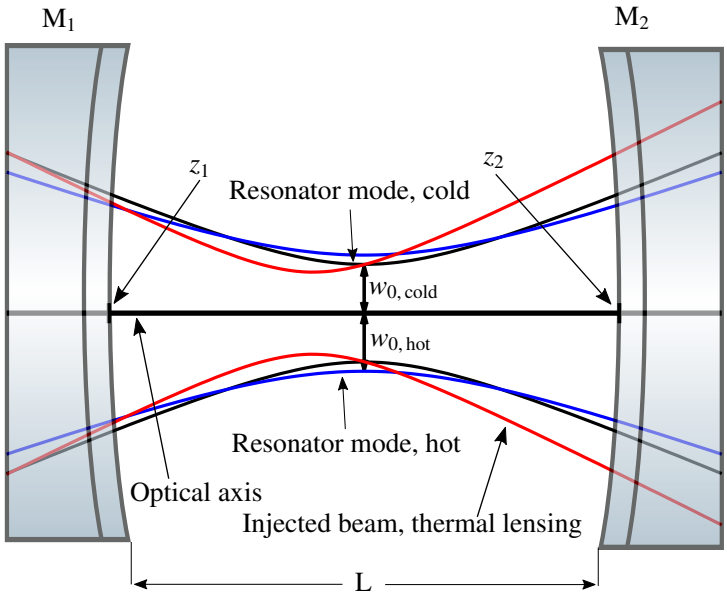

Figure 3.4: Thermally-induced changes of an optical two-mirror resonator. The black resonator eigenmode depicts the 'cold' case, where no light is injected into the resonator. The corresponding beam waist is called $w_{0,\mathrm{cold}}$. The blue resonator mode illustrates the 'hot' case, where laser light is circulating inside the resonator. A small part of the intra-cavity power gets absorbed by the coatings of M_1 and M_2 and is transformed into heat, which is conducted to the mirror substrates. Due to thermal expansion, the radii of curvature of both mirrors are decreased, resulting in the blue resonator mode. The latter exhibits an increased waist size $w_{0,\mathrm{hot}}$. The largest thermal aberration is caused by thermal lensing inside of the substrate of M_1. The non-uniform temperature distribution in M_1 yields to an index of refraction gradient, which has the same effect as a spherical lens. Thus, the in-coupled laser mode is changed, which is illustrated by the red graph. Both, thermal expansion and thermal lensing result in an increased coupling from the fundamental TEM_{00} mode to higher-order modes and less power is coupled into the resonator. Adapted from ([17], p. 147).

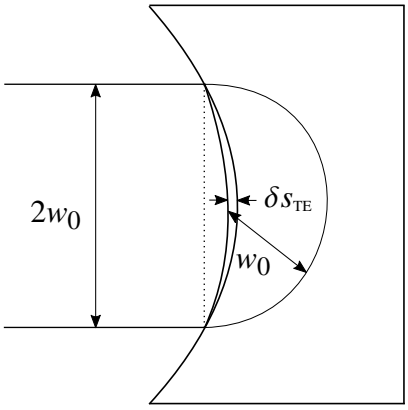

Figure 3.5: Temperature distribution and thermal expansion in the Winkler model. Coating absorption of the laser beam with diameter $2w_0$ yields to a hemispherical temperature gradient inside of the mirror substrate. Thermal expansion induces the mirror curvature depth change δs_{TE}. Adapted from [92].

3.4 Calculation of the temperature profile and the thermally-induced optical path length change

3.4.1 The Winkler model

A simple analytical estimation of the temperature rise due to coating absorption and the resulting optical path length change in the mirror substrate is given by the Winkler model [92]. As shown in figure 3.5, a laser beam with radius w_0 impinges on the mirror coating and a small part of the light power is absorbed and transformed into heat. The heat is transported from the reflection spot via heat conduction. The heated volume inside of the mirror substrate is approximated by a hemisphere with radius w_0 around the reflection spot. The largest temperature gradient is located within this hemisphere. The resulting temperature difference between the center and the outer parts of the hemisphere at w_0 is given by [92]

$$\delta T \approx \frac{P_{\mathrm{a}}}{2\pi k_{\mathrm{th}} w_0}, \tag{3.11}$$

where P_{a} is the absorbed light power and k_{th} is the heat conductivity of the substrate material. Increasing absorption as well as a smaller beam radius yield to a larger temperature increase. Due to the coefficient of thermal expansion, a_{th}, the heated mirror expands, resulting in a change δs_{TE} of the curvature depth of the mirror which can be estimated as [92]

$$\delta s_{\mathrm{TE}} \approx \frac{a_{\mathrm{th}}}{4\pi k_{\mathrm{th}}} P_{\mathrm{a}}. \tag{3.12}$$

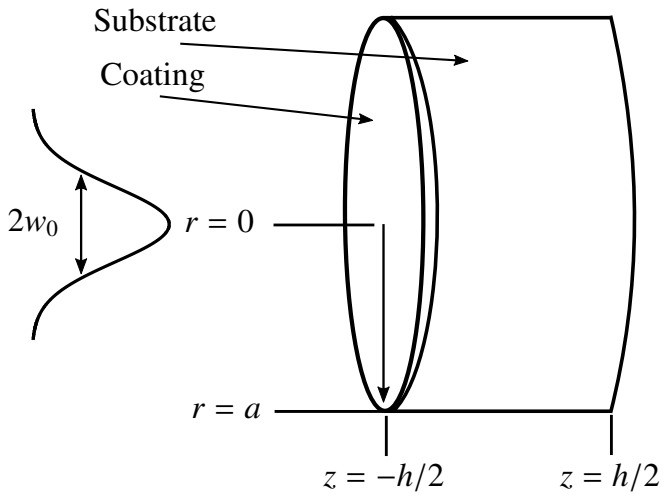

Figure 3.6: Geometry in the Hello and Vinet model. A laser beam with Gaussian intensity distribution impinges onto a mirror coating and a small part of the light power gets absorbed. The mirror substrate has the thickness h and the radius a and looses heat by thermal radiation. Adapted from ([20], p. 18), [40].

The wavefront curvature of a beam transmitted through the heated substrate is deformed by thermal lensing. The optical path length difference (OPD) between the center and the outer parts of the heated hemisphere is [92]

$$\delta s_{\mathrm{TR}} \approx \frac{\beta}{4\pi k_{\mathrm{th}}} P_{\mathrm{a}}, \tag{3.13}$$

where $\beta = \mathrm{d}n/\mathrm{d}T$ is the thermorefractive coefficient.
A more accurate computation of thermally-induced distortions, taking into account the non-uniform intensity distribution of a Gaussian beam, is provided by the model from Hello and Vinet, which is presented in the next section.

3.4.2 The Hello & Vinet model

A comprehensive analytical model for the calculation of the non-uniform temperature distribution inside of the mirror substrate, induced by coating absorption of a Gaussian laser beam, is provided by Hello and Vinet [40]. As depicted in figure 3.6, the mirror substrate is described by a cylinder located at the radial coordinates $0 \leq r \leq a$ and the axial coordinates $-h/2 \leq z \leq h/2$. Because the coating is much thinner than the mirror substrate, it is treated as an inward heat flux, applied at $z = -h/2$, and its material parameters are neglected. Therefore, the computation of the temperature distribution only depends on the substrate material parameters.

The heat equation describing the time evolution of the temperature field $T(r, z, t)$ is ([24], p. 286)

$$\rho c_{\mathrm{w}} \frac{\partial T(r,z,t)}{\partial t} - k_{\mathrm{th}} \Delta T(r,z,t) = p(r,z,t), \tag{3.14}$$

where ρ is the density, c_{w} the specific heat and k_{th} the thermal conductivity of the mirror substrate material. $p(r, z, t)$ describes an internal heat source inside of the mirror substrate. z is the longitudinal coordinate and r the distance from the optical axis. For the stationary case where no internal heat source exists, equation (3.14) becomes the Laplace equation

$$\Delta T(r,z) = \left(\frac{\partial^2}{\partial r^2} + \frac{1}{r}\frac{\partial}{\partial r} + \frac{\partial^2}{\partial z^2} \right) T(r,z) = 0, \tag{3.15}$$

which can be solved by the function ([24], p. 289)

$$T(r,z) = J_0(mr)\left(Ae^{mz} + Be^{-mz}\right). \tag{3.16}$$

m, A and B are constants and J_0 is the zero-order Bessel function. In the steady state, the mirror substrate looses its heat to the environment by surface radiation. The surface heat loss is described by ([24], p. 287)

$$F = \sigma_{\mathrm{c}}[T^4 - T_0^4], \tag{3.17}$$

where $\sigma_{\mathrm{c}} = \epsilon\sigma_{\mathrm{SB}}$ is the emissivity-corrected Stefan Boltzmann constant. ϵ is the emissivity and σ_{SB} is the Stefan Boltzmann constant. T is the temperature of the substrate and T_0 the temperature of the environment. In the case of low absorption, the temperature increase in the mirror substrate is very small, $\delta T = T - T_0 \ll T_0$, and equation (3.17) can be linearized and becomes

$$F \approx 4\sigma_{\mathrm{c}} T_0^3 \delta T. \tag{3.18}$$

The boundary condition at $z = -h/2$ is ([24], p. 288)

$$-k_{\mathrm{th}} \frac{\partial T}{\partial z}(r, -h/2) = -4\sigma_{\mathrm{c}} T_0^3 T(r, -h/2) + \alpha_{\mathrm{c}} I(r). \tag{3.19}$$

The product $\alpha_{\mathrm{c}} I(r)$ is the dissipated light power in the coating, α_c is the coating absorption coefficient and $-4\sigma_{\mathrm{c}} T_0^3 T(r, -h/2)$ the radiative heat loss in $-z$ direction. $I(r)$ is the intensity distribution of the fundamental TEM_{00} mode [40]

$$I(r) = \frac{2P}{\pi w_0^2} \exp\left(\frac{-2r}{w_0^2}\right). \tag{3.20}$$

Here, P is the power of the impinging laser beam and w_0 is its waist size. The boundary conditions at $z = h/2$ and $r = a$, which only describe radiative heat losses, are ([24], pp. 287 – 288)

$$-k_{\mathrm{th}} \frac{\partial T}{\partial z}(r, h/2) = 4\sigma_{\mathrm{c}} T_0^3 T(r, h/2) \tag{3.21}$$

and

$$-k_{\mathrm{th}} \frac{\partial T}{\partial z}(a, z) = 4\sigma_{\mathrm{c}} T_0^3 T(a, z). \tag{3.22}$$

To obtain the value m, the solution (3.16) is inserted into boundary condition (3.22), leading to

$$k_{\mathrm{th}} m J_1(ma) = 4\sigma_{\mathrm{c}} T_0^3 J_0(ma), \tag{3.23}$$

where J_1 is the first-order Bessel function. With the reduced radiation constant $\chi_{\mathrm{r}} = 4\sigma_{\mathrm{c}} T_0^3 a/k_{\mathrm{th}}$ and $\zeta = ma$, equation (3.23) becomes ([24], p. 289)

$$\zeta J_1(\zeta) - \chi_{\mathrm{r}} J_0(\zeta) = 0, \tag{3.24}$$

which has an infinite and discrete number of solutions, given as $\{\zeta_j \,;\, j = 1, 2, ...\}$. Thus, the values m become $m_j = \zeta_j/a$ and equation (3.16) can be rewritten as the sum

$$T(r, z) = \sum_j \left(A_j e^{m_j z} + B_j e^{-m_j z} \right) J_0(m_j r). \tag{3.25}$$

The orthogonal and complete functions $\{J_0(m_j r/a) \,;\, j = 1, 2, ...\}$ form a basis and have the normalization constants

$$c_j = \frac{2\zeta_j^2}{a^2 \left(\chi_{\mathrm{r}}^2 + \zeta_j^2 \right) J_0(\zeta_j)^2}. \tag{3.26}$$

Furthermore, the laser intensity $I(r)$ can be expanded in the $\{J_0(m_j r/a)\}$ basis

$$I(r) = \sum_{j=0} p_j J_0(m_j r/a), \tag{3.27}$$

where the coefficients p_j are given by

$$p_j = \frac{P}{\pi a^2} \frac{\zeta_j^2}{(\zeta_j^2 + \chi_{\mathrm{r}}^2) J_0(\zeta_j)^2} \exp\left(\frac{w_0^2 \zeta_j^2}{8a^2} \right). \tag{3.28}$$

Inserting the equations (3.27) and (3.25) into the boundary conditions (3.19) and (3.21) and defining $\Gamma_i = \exp\left(-\zeta_j h/2a\right)$ leads to the linear system of equations

$$(\zeta_j - \chi_\mathrm{r})\Gamma_j^2 A_j - (\zeta_j + \chi_\mathrm{r})B_j = -\frac{\alpha_\mathrm{c} p_j a \Gamma_j}{k_\mathrm{th}} \tag{3.29}$$

$$(\zeta_j + \chi_\mathrm{r})A_j - (\zeta_j - \chi_\mathrm{r})\Gamma_j^2 B_j = 0. \tag{3.30}$$

From this system, the amplitudes A_j and B_j of the temperature distribution (3.25) are computed to

$$A_j = \frac{\alpha_\mathrm{c} p_j a}{k_\mathrm{th}} \exp\Big(-3\zeta_j h/2a\Big) \frac{(\zeta_j - \chi_\mathrm{r})}{(\zeta_j + \chi_\mathrm{r})^2 - (\zeta_j - \chi_\mathrm{r})^2 \exp\Big(-2\zeta_j h/a\Big)} \tag{3.31}$$

and

$$B_j = \frac{\alpha_\mathrm{c} p_j a}{k_\mathrm{th}} \exp\Big(-\zeta_j h/2a\Big) \frac{(\zeta_j + \chi_\mathrm{r})}{(\zeta_j + \chi_\mathrm{r})^2 - (\zeta_j - \chi_\mathrm{r})^2 \exp\Big(-2\zeta_j h/a\Big)}. \tag{3.32}$$

With (3.31) and (3.32), equation (3.25) finally becomes ([24], p. 290)

$$T(r,z) = \sum_j \frac{\alpha_\mathrm{c} p_j a}{k_\mathrm{th}} \exp\Big(-\zeta_j h/2a\Big) \times \left[\frac{(\zeta_j - \chi_\mathrm{r}) \exp\Big(-\zeta_j (h-z)/a\Big) + (\zeta_j + \chi_\mathrm{r}) \exp\Big(-\zeta_j z/a\Big)}{(\zeta_j + \chi_\mathrm{r})^2 - (\zeta_j - \chi_\mathrm{r})^2 \exp\Big(-2\zeta_j h/a\Big)}\right] J_0(m_j r). \tag{3.33}$$

Equation (3.33) describes the temperature distribution inside of a cylindrical mirror substrate in the steady state that is caused by coating absorption.

3.5 Measurement method and data analysis

In our measurement method [77], high laser powers are used to determine small coating absorptions. The coating under investigation is used as the in-coupling mirror M_1 of an optical resonator with a large power build up. The resonator's round-trip length is externally modulated with a piezo-actuator (PZT), which periodically changes the position of the end mirror M_2. The corresponding round-trip phase change $\delta(t)$ can either be positive or negative. When the round-trip length is altered and the cavity resonance is approached, the intra-cavity power increases and both mirror coatings start to absorb a small part of the circulating light power. The heat is transferred to the mirror substrates. This results in a time-dependent temperature profile in the substrate of the in-coupling mirror M_1, which has two consequences. First, due to the non-vanishing and positive coefficient of thermal expansion a_th, both mirrors expand into the cavity. This effect is denoted by the dashed

lines in figure 3.7. Because the mirrors are clamped to an aluminum spacer, this results in a reduction of the cavity round-trip length or the cavity round-trip phase $\Phi_{\mathrm{cav}}(t)$, respectively. The second effect is related to the in-coupled laser beam, which propagates through the in-coupling mirror into the resonator. The time-dependent temperature profile in mirror M_1 leads to an increase of the optical path length due to thermal expansion and because of a non-vanishing and positive thermorefractive coefficient $\mathrm{d}n/\mathrm{d}T$. Thus, the in-coupled beam propagating through M_1 is delayed by a time-dependent phase $\Phi_{\mathrm{in}}(t)$ with respect to the field, circulating inside of the resonator. From the in-coupled beams point of view, the phase delay corresponds to a mirror M_1 that is moving farther away. This effect corresponds to a thermally-induced shortening of the resonator round-trip length, leading to a resonance peak deformation [77]. The phase delay due to $\mathrm{d}n/\mathrm{d}T$ is only caused by the in-coupling mirror M_1, while the phase shift due to thermal expansion is caused by both mirrors. An optical path length change due to substrate absorption in M_1 is negligible, because on resonance, the light power outside of the resonator is small compared to the intra-cavity power.

For an absorption measurement, the cavity round-trip length is externally altered by a PZT. Because of $(\alpha_{\mathrm{th}} + \mathrm{d}n/\mathrm{d}T) > 0$, the in-coupled light is delayed and the detected resonance peaks show a hysteresis. This is depicted in figure 3.8 for simulated resonance peaks in reflection of an optical resonator. External lengthening of the resonator round-trip length (blue graph) results in a larger width compared to a normal resonance peak without absorption (black dashed graph). External shortening of the resonator round-trip length results in a smaller width of the resonance peak (red graph). These thermally-induced resonance peak deformations are also called thermal Kerr effect. The resonance peaks in reflection of the resonator are detected with a photo-diode for both scan directions. They are numerically fitted with the program TkSim, which varies the power reflectivities R_1, $\widetilde{R_2}$ and the coating absorption coefficient α_{C} to minimize the deviation between the measured and the simulated data in order to gain a fit. $\widetilde{R_2}$ denotes the effective reflectivity of mirror M_2, that includes all resonator round-trip losses except of the transmission of M_1. TkSim was written by Nico Lastzka ([50], pp. 69 – 91) and is based on the theory from Hello and Vinet which was introduced in section 3.4.2 for the stationary case. However, in our measurement method, the cavity resonance was scanned in hundreds of micro-seconds which is far away from the steady state. Therefore, TkSim starts with an arbitrary resonator detuning and the steady state solution of the temperature field, given by equation (3.33), to obtain the time-dependent temperature distribution $T(t, r, z)$ with the theory shown in [40, 62]. After each round-trip, the program calculates the intra-cavity as well as the reflected field, which have both gained the thermal phase ([50], p. 76)

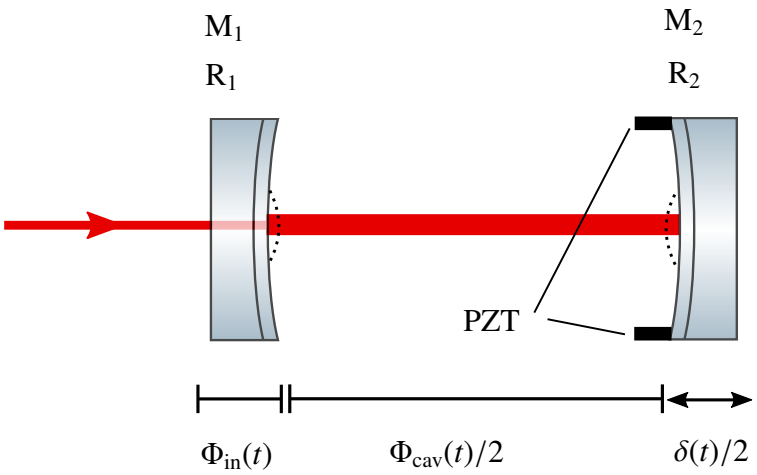

Figure 3.7: Photothermal-self-phase modulation technique. Laser light is injected into a two-mirror resonator, while its round-trip length is periodically scanned by the piezo-actuated mirror M_2. This results in a round-trip phase change of $\delta(t)$. If the resonance is approached, the circulating power starts to build up and both coatings on the mirrors M_1 and M_2 start to absorb a small part of the light power. Both mirror substrates are heated locally and non-uniformly. Due to the thermal expansion (illustrated by the black dashed lines) of both mirrors, the resonator round-trip length is decreased. Additionally, the temperature-induced and time-dependent refractive index change in M_1 causes a phase delay $\Phi_{in}(t)$ of the in-coupled beam. Adapted from [51].

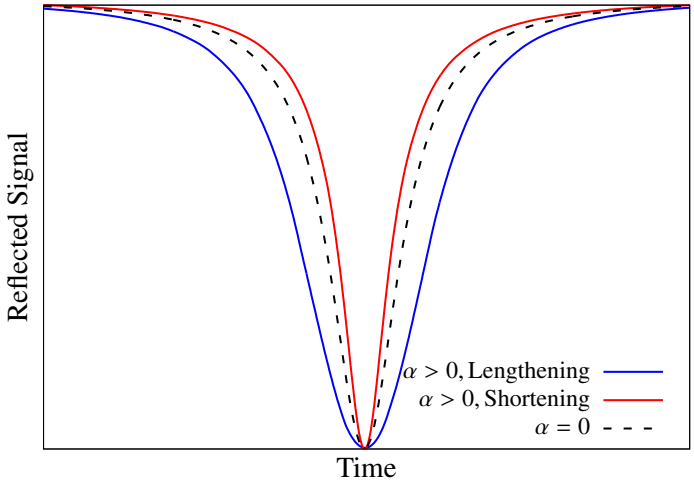

Figure 3.8: Simulated thermal deformation of the resonance peaks in reflection of an optical resonator. A non-vanishing absorption of laser power in the dielectric mirror coatings results in thermal expansion of both mirror substrates and thus, in a decrease of the resonator round-trip length. External lengthening of the round-trip length leads to a resonance peak with an increased width (blue graph). External shortening of the resonator round-trip length results in a faster resonance scan and thus, in a peak with a reduced width (red curve). For comparison, the dashed black graph depicts the case without coating absorption.

$$\Phi_{\mathrm{th}} = \frac{2\pi}{\lambda}\frac{\mathrm{d}n}{\mathrm{d}T}\int_{-h/2}^{h/2}[T(t,r,z)-T_0]\,\mathrm{d}z. \tag{3.34}$$

TkSim evaluates the thermal phase Φ_{th} at the optical axis, where $r = 0$.

3.6 Design of the two-mirror resonator

The optical resonator that was used to measure the absorption of the AlGaAs coatings consisted of the plane in-coupling mirror M_1 and the second mirror M_2, which had a radii of curvature of 1.0 m. The geometrical spacing between both mirrors was 9 mm, resulting in a stable resonator ($g_1 g_2 = 0.991$) with a FSR of 16.655 GHz. The design power reflectivity of the AlGaAs coatings at 1064 nm and 1550 nm was (99.96 ± 0.01) %. The coating of the second mirror was a dielectric multilayer coating made of silica and tantalum pentoxide and had a power reflectivity of about $R_2 = 99.97$ % at both wavelengths. Thus, the FWHM design value was 2 MHz, leading to a finesse of 8975. Both mirrors were clamped to an aluminum spacer. A PZT between the spacer and mirror M_2 was used to change the resonator round-trip length. The resonator beam waist w_0 at 1064 nm was 150 μm and 181 μm at 1550 nm.

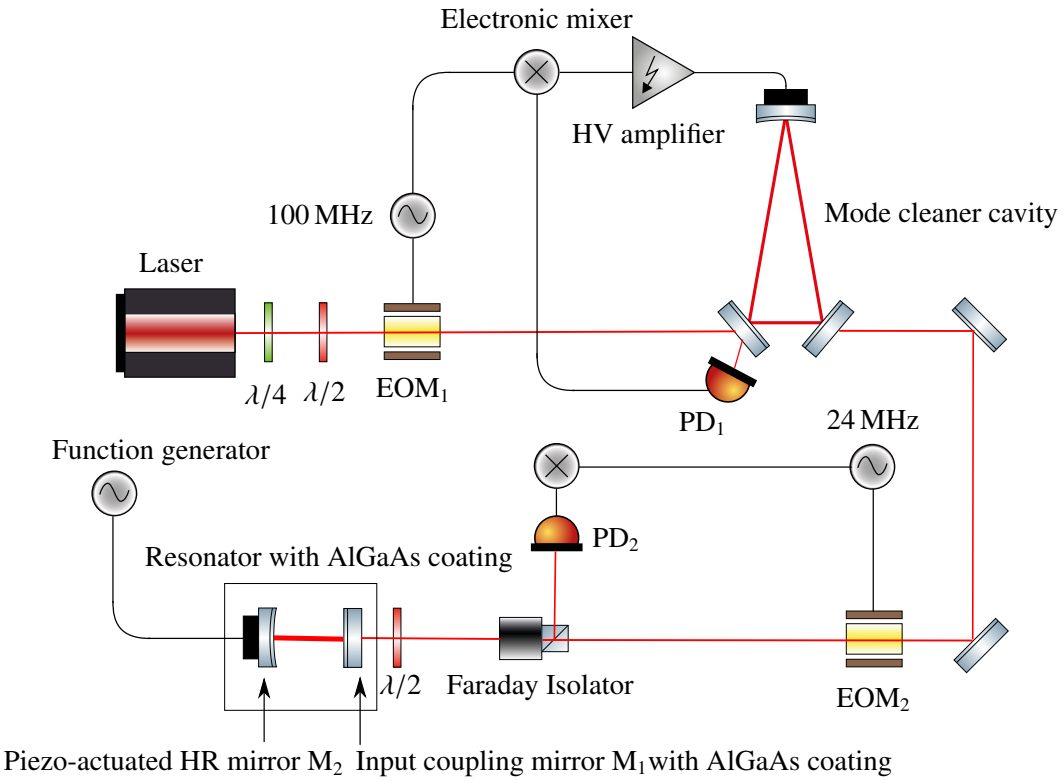

Figure 3.9: Schematic of the experimental setup for measuring the optical power absorption of the AlGaAs coatings. Excess circular polarization of the laser light was corrected with a quarter-wave plate and a half-wave plate accurately defined the light's polarization before entering EOM_1. A three-mirror mode-cleaner resonator, which was length-stabilized with the PDH-technique to be resonant for the incoming laser light, provided a temporal and spatially cleaned TEM_{00} mode. The length of the resonator containing the AlGaAs coating was periodically altered with a piezo-actuated end mirror and a function generator. Incoming and reflected beam were spatially separated with a Faraday isolator and the resonance peaks in reflection of the resonator were measured with PD_2. The combination of EOM_2 and PD_2 yielded an out-of-phase PDH-error signal, which was used for the calibration of the time axis of the detected resonance peaks.

3.7 Experimental setup

A schematic of the experimental setup for measuring the coating absorption of the AlGaAs coatings is shown in figure 3.9. The laser light (1064 nm or 1550 nm) was corrected for residual circular polarization with a quarter-wave plate. A half-wave plate properly defined the polarization of the light before passing through EOM_1, which imprinted phase modulated sidebands at a frequency of 100 MHz. These sidebands were used to stabilize the length of a three-mirror mode-cleaner ring resonator on resonance by using the Pound-Drever-Hall technique [29]. The mode-cleaner resonator provided a spatially and temporally filtered TEM_{00} laser mode. EOM_2 imprinted phase-modulated sidebands at a frequency of 24 MHz onto the laser light, which served as frequency markers for the absorption measurements, where they were used for the calibration of the time axis of the detected resonance peaks. The resonator used for the coating absorption measurements was formed by the mirrors M_1 and M_2. The AlGaAs coating was applied on the plane incoupling mirror M_1. To measure the resonance peaks in reflection with photo diode PD_2, the resonator round-trip length was periodically changed by applying a triangular-wave voltage to the piezo-actuated mirror M_2. To avoid any nonlinearities of the PZT, only a small part of the resonator's FSR was scanned and the measured resonance peak was kept away from the turning points of the triangular-wave voltage. The voltage was provided by a function generator. Incoming and reflected light beam were separated with a faraday isolator.

3.8 Important input parameters of the time-domain simulation TkSim

The computation of the temperature profile in TkSim only depends on the substrate material (Corning 7980) parameters, while the material parameters of the μm thick coating are neglected ([50], p. 71), ([75], pp. 28 – 29). This assumption holds for dielectric mirror coatings, which are made of silica and tantalum pentoxide, as pointed out by table 3.1 where the most important input parameters for TkSim are listed. Compared to TaO_5, the thermal conductivity k_{th} of Corning 7980 is a factor of 2.3 larger. The parameter, which dominates the thermal phase shift, is the thermorefractive coefficient $\mathrm{d}n/\mathrm{d}T$. As shown in table 3.1, Corning 7980 has a larger $\mathrm{d}n/\mathrm{d}T$ than TaO_5. This is also true for the coefficient of thermal expansion, a_{th}. Thus, the above assumption of neglecting the coating material parameters is valid. This changes when multilayer coatings made of GaAs and $Al_{0.92}Ga_{0.08}As$ on top of a Corning 7980 mirror substrate are used.

	Corning 7980	SiO_2	Ta_2O_5	$GaAs/Al_{0.92}Ga_{0.08}As$
k_{th} [W/mK]	1.38 [54]	1.38 [54]	0.6 [35]	63.0
c_w [J/kgK]	703 [54]	703 [54]	306 [35]	389.27
ρ [kg/m^3]	2203 [54]	2203 [54]	6850 [35]	4546.72
dn/dT [1/K]	$8.6 \cdot 10^{-6}$ [28]	$8.6 \cdot 10^{-6}$ [28]	$2.3 \cdot 10^{-6}$ [35]	$2.66 \cdot 10^{-4}$
a_{th} [1/K]	$5.2 \cdot 10^{-7}$ [25]	$5.2 \cdot 10^{-7}$ [25]	$3.6 \cdot 10^{-6}$ [35]	$5.47 \cdot 10^{-6}$

Table 3.1: List of the important material input parameters for TkSim for fused silica, silica (SiO_2), tantalum pentoxide (TaO_5) and $GaAs/Al_{0.92}Ga_{0.08}As$. The presented $GaAs/Al_{0.92}Ga_{0.08}As$ parameters are calculated in appendix C. k_{th}, c_w and ρ are used to compute the temperature profile in the in-coupling mirror M_1 and dn/dT and a_{th} are the parameters which determine the thermally-induced phase shift. In this table, dn/dT is shown for the wavelength of 1064 nm. Please note that Coning 7980 and SiO_2 are the same materials. They are shown in two separate columns to differentiate between coating and substrate parameters.

The last column in table 3.1 displays the material parameters for the AlGaAs coating at 1064 nm, which was investigated in this work (see appendix C.1 for the parameter calculation). First, the thermal conductivity of the AlGaAs coating is about 46 times larger than the one of Corning 7980. Consequently, the AlGaAs coating first spreads the heat in radial direction, leading to an effective temperature reduction along the optical axis (the z-direction in cylindrical coordinates). TkSim evaluates the temperature and the thermal phase shift inside of the mirror substrate along the optical axis at $r = 0$ in order to determine the coating absorption. Thus, to model the effect of the AlGaAs coating, the laser power in TkSim needs to be reduced. Secondly, the thermorefractive coefficient of AlGaAs is about 31 times larger than the dn/dT of Corning 7980. Furthermore, the coefficient of thermal expansion of AlGaAs is a factor 10.5 larger than a_{th} from Corning 7980. Thus, in the case of a non-vanishing absorption α_C, the coating dn/dT and a_{th} contribute to the thermally-induced time-dependent phase shift during a resonance scan and cannot be neglected. The complete input parameter list of TkSim is shown in appendix B.

To investigate the AlGaAs coating induced temperature reduction along the optical axis inside of the Corning 7980 mirror substrate as well as the weighting between coating and substrate material parameters, the method of finite element analysis (FEA) was used. Since the thermorefractive and the thermoelastic coefficient are the material parameters in TkSim which determine the optical coating absorption, the parameter-weighting only applies to them. The effect of the coating density, specific heat and thermal conductivity is modeled by the reduction of the laser power in TkSim. In this thesis, FEA calculations were carried out with the program COMSOL Multiphysics, version 5.2a.

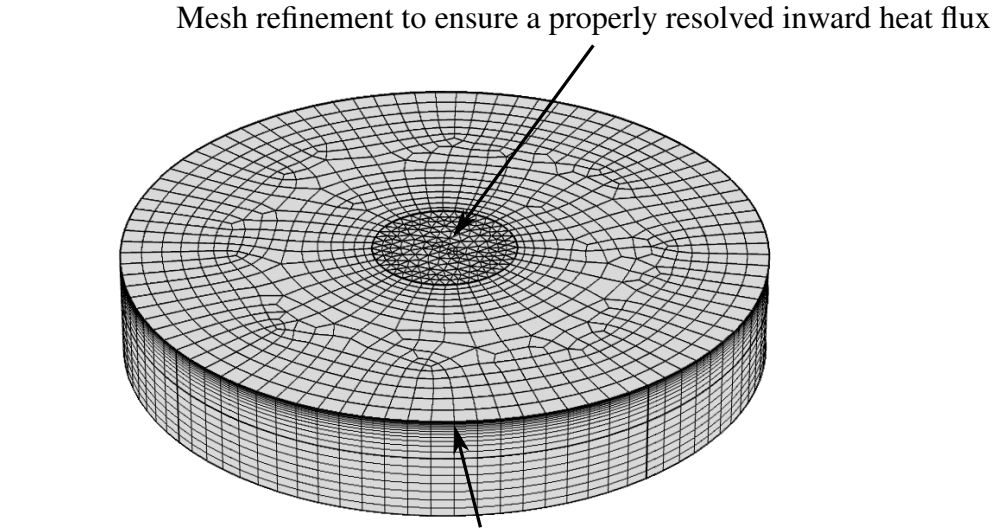

Figure 3.10: COMSOL model for the numerical simulation of the AlGaAs coating on top of the Corning 7980 substrate. The mirror substrate was represented by a cylinder with a radius of 2 mm and a thickness of 0.65 mm. The coating on top of the substrate was modeled as a cylinder with a radius of 2 mm and a thickness of 3.9 μm (1064 nm) and 6.5 μm (1550 nm), respectively. The mesh was locally refined to guarantee a smooth transition from the fine meshed coating to the coarser meshed substrate. To resolve the inward heat flux representing the laser beam which had a beam waist size of 150 μm (1064 nm) and 181 μm (1550 nm), respectively, the mesh in the center of the coating was refined with elements which had a maximum length of 75 μm.

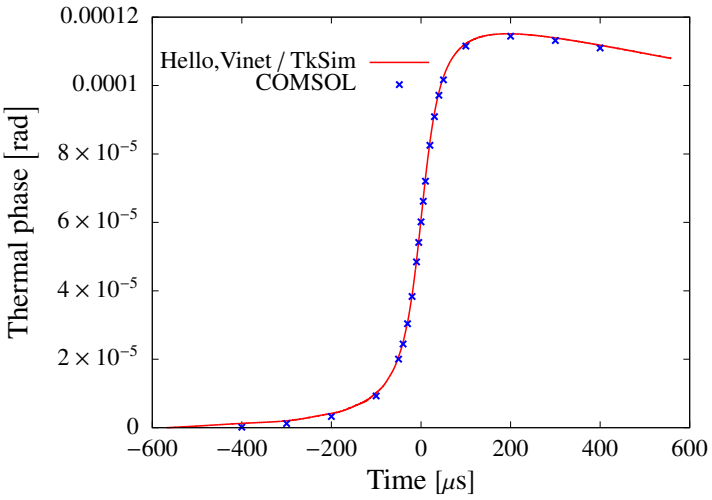

Figure 3.11: Comparison between the analytical model by Hello and Vinet, computed with TkSim (solid red line), and COMSOL (blue crosses). For the comparison both, the coating and the substrate parameters of the COMSOL model were set to the parameters of Corning 7980. The same time-dependent Lorentzian function and the same heat power were applied in TkSim and in COMSOL. Each program simulated the transient temperature profile and the corresponding thermally-induced phase shifts were computed, using equation (3.34). Both results were in excellent agreement.

3.9 The finite element model

The method of FEA can be used to calculate complex mechanical, thermal or electrical problems, which cannot be solved analytically. In a FEA, first, the geometry is defined and the component under investigation is divided into small elements. In the three-dimensional case, these elements have typically tetrahedral or cubic shape. Then, the material parameters are assigned and loads and boundary conditions are defined and the problem is numerically solved. In this work, FEA is used to simulate the transient heating process of an AlGaAs coating on top of a Corning 7980 substrate.

Because the resonance scans during the measurements were carried out in hundreds of microseconds and thus, the heating process of mirror M_1 was far away from the steady state, it was sufficient to simulate a small section of the Corning 7980 mirror substrate with the AlGaAs coating on top in order to reduce the computation time. The mirror substrate was represented by a cylinder with a diameter of 2 mm and a thickness of 0.65 mm. The AlGaAs coating was designed as a cylinder with a diameter of 2 mm and a thickness of 3.9 μm (1064 nm) and 6.5 μm (1550 nm), respectively. The product of a spatially Gaussian-shaped inward heat flux and a time-dependent normalized Lorentzian-shaped resonance peak $L(t)$

$$H(t,r) = \frac{2P_{\max}L(t)}{\pi w_0^2}\exp\left(\frac{-r^2}{w_0^2}\right) \tag{3.35}$$

was applied to the AlGaAs coating to simulate the transient heating process during a resonance scan. Here $P_{\max}$ is the maximum power of the Gaussian-shaped inward heat flux and w_0 is its radius, corresponding to the waist size of the laser beam. Note that equation (3.35) is only a slight variation of equation (3.20) with an added time-dependence. Both, coating and substrate lost heat due to thermal surface radiation. The mesh of the COMSOL model, which is shown in figure 3.10, was carefully refined to guarantee a smooth transition from the fine meshed coating to the coarser meshed mirror substrate. To resolve the laser beam with diameter of $300\,\mu$m, the center area of the coating consisted of mesh elements with a maximum length of $75\,\mu$m. Local mesh refinements were performed and convergence was achieved. Furthermore, an appropriate time-discretization in COMSOL was chosen to properly resolve the transient heating process. To compare the COMSOL model to the theory of Hello and Vinet, the material parameters of the coating and the substrate were both set to the parameters of Corning 7980. The inward heat flux with the same time-dependent Lorentzian function and the same power was applied in COMSOL and TkSim. For both programs, the time-dependent temperature profiles were simulated and the corresponding thermally-induced phase shifts were calculated with equation (3.34). Figure 3.11 shows the comparison between the Hello and Vinet Model, calculated with TkSim, and the COMSOL model. For the same material parameters and the same inward heat flux, TkSim and COMSOL showed an excellent agreement.

3.10 Data evaluation method with TkSim and COMSOL

As emphasized in section 3.8, the coating material parameters cannot be neglected in TkSim, when the absorption of AlGaAs coatings is investigated. In this section, a method for obtaining the right parameter-weighting between coating (AlGaAs) and substrate (Corning 7980) parameters is introduced. With this method, also the laser power reduction factors for TkSim were obtained (see figure 3.13).

For each scan frequency, the cavity resonance peaks in reflection were measured with a photo diode for external shortening and for external lengthening of the resonator round-trip length. Only small thermally-induced resonance peak deformations were observed. Consequently, also the difference in the observed deformation between the resonance peak recorded for external shortening and the resonance peak detected for external lengthening, was small. Because of that, simply the resonance peak, measured for external lengthening, was chosen to evaluate the laser power reduction in direction of the optical axis as well as

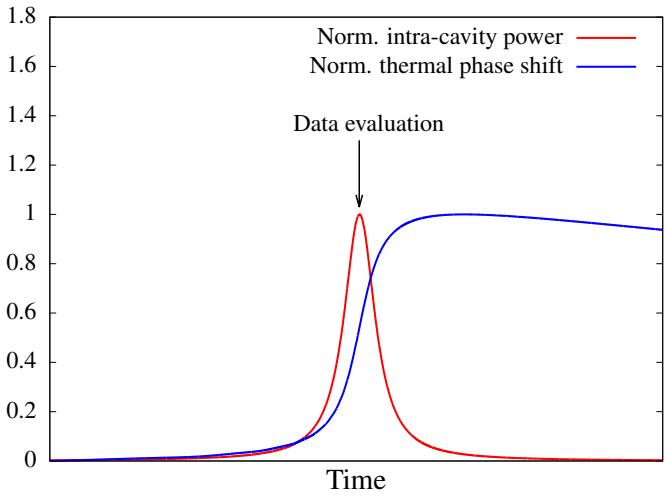

Figure 3.12: Normalized intra-cavity power and normalized thermal phase shift. The COMSOL simulations were evaluated at the time which corresponded to the maximum intra-cavity power (red curve). Here, the thermally-induced phase shift (blue graph) has its maximum slope.

the weighting between coating and substrate material parameters. The evaluation process consisted of three steps:

1. The recorded resonance peak for external resonator round-trip lengthening was fitted and the corresponding intra-cavity power was extracted and normalized. For the further data evaluation, the time corresponding to the maximum intra-cavity power was chosen, as depicted in figure 3.12 by the black arrow. At this point in time, the thermal phase shift, given by equation (3.34), has its maximum slope.

2. The factor which determined how much the laser power in TkSim needed to be reduced was determined by three COMSOL simulations. For the first simulation, both, the coating and the substrate parameters were set to Corning 7980 and a certain heat power P_{max} was used for the inward heat flux. The temperature distribution was evaluated at the time, corresponding to the maximum intra-cavity power. This is depicted by the black graph in figure 3.13, which shows the temperature inside of the coating and of the mirror substrate along the z-axis. In this figure, the mirror coating is localized between $z = 6.3539\,\mathrm{mm}$ and $z = 6.35\,\mathrm{mm}$ (corresponding to the dimensions of the AlGaAs coating specified at 1064 nm). The mirror substrate is localized between at $z = 0\,\mathrm{mm}$ and $z = 6.35\,\mathrm{mm}$. The transition between substrate and coating is illustrated by the black dashed line. The blue dashed line marks the middle of the coating at $z = 6.35195\,\mathrm{mm}$.

After that, the coating parameters were set to AlGaAs while the substrate parameters were kept as Corning 7980. A second COMSOL simulation was performed, using the same power P_{max} as in the first simulation, leading to the blue curve in figure 3.13. As expected, the AlGaAs coating reduced the temperature in z-direction inside of the Corning 7980 substrate.
For the third COMSOL simulation, the coating parameters were again set to Corning 7980 and the power P_{max} was reduced to approximate the temperature distribution which was computed in the second simulation. The corresponding temperature profile is depicted in figure 3.13 by the red graph. The red curve approximates the area below the blue curve and thus, corresponds to the heat input into the Corning 7980 substrate, caused by the AlGaAs coating.

3. To determine the parameter weighting between the AlGaAs coating parameters and the Corning 7980 substrate parameters, the heat inputs into the coating and into the substrate were evaluated by integrating the temperature along the z-axis. For the integration the temperature profile obtained by the COMSOL simulation for the AlGaAs coating on top of the Corning 7980 substrate was used. This is depicted in figure 3.14. First, the heat input inside of the AlGaAs coating was obtained by evaluating the integral

$$A_{\text{coating}} = \int_{6.35\,\text{mm}}^{6.3539\,\text{mm}} [T(t,0,z) - T_0]\,\mathrm{d}z. \tag{3.36}$$

Here the upper boundary for the integral corresponded to the 3.9 μm thick AlGaAs coating, specified for 1064 nm. For the AlGaAs coating specified for 1550 nm, the upper limit was 6.3565 mm. In the same way, the heat input into the Corning 7980 substrate was obtained by calculating the integral

$$A_{\text{substrate}} = \int_{0\,\text{mm}}^{6.35\,\text{mm}} [T(t,0,z) - T_0]\,\mathrm{d}z. \tag{3.37}$$

The contribution of the coating to the material parameter weighting for TkSim was

$$C_{\text{coating}} = \frac{A_{\text{coating}}}{A_{\text{coating}} + A_{\text{substrate}}}. \tag{3.38}$$

The substrate contribution to the material parameter weighting for TkSim was given by

$$C_{\text{substrate}} = \frac{A_{\text{substrate}}}{A_{\text{coating}} + A_{\text{substrate}}}. \tag{3.39}$$

With the factors C_{coating} and $C_{\text{substrate}}$, the weighted thermorefractive and thermoelastic coefficients for TkSim were calculated as

$$\frac{\mathrm{d}n}{\mathrm{d}T}_{\text{TkSim}} = C_{\text{coating}} \frac{\mathrm{d}n}{\mathrm{d}T}_{\text{AlGaAs}} + C_{\text{substrate}} \frac{\mathrm{d}n}{\mathrm{d}T}_{\text{Corning 7980}} \tag{3.40}$$

and

$$a_{\text{th, TkSim}} = C_{\text{coating}} a_{\text{th, AlGaAs}} + C_{\text{substrate}} a_{\text{th, Corning 7980}}. \tag{3.41}$$

In the numerical simulations performed with TkSim, only the thermal expansion of the input-coupling mirror M_1 was considered and the Phi-factor that determined the number of mirrors expanding into the cavity was set to one. Thus the thermal expansion of the second mirror M_2 was added to the first mirror and equation (3.41) became

$$a_{\text{th, TkSim}} = C_{\text{coating}} a_{\text{th, AlGaAs}} + C_{\text{substrate}} a_{\text{th, Corning 7980}} + a_{\text{th, Corning 7980}}. \tag{3.42}$$

This was possible because the coating applied to the second mirror was a standard SiO_2/Ta_2O_5 coating.

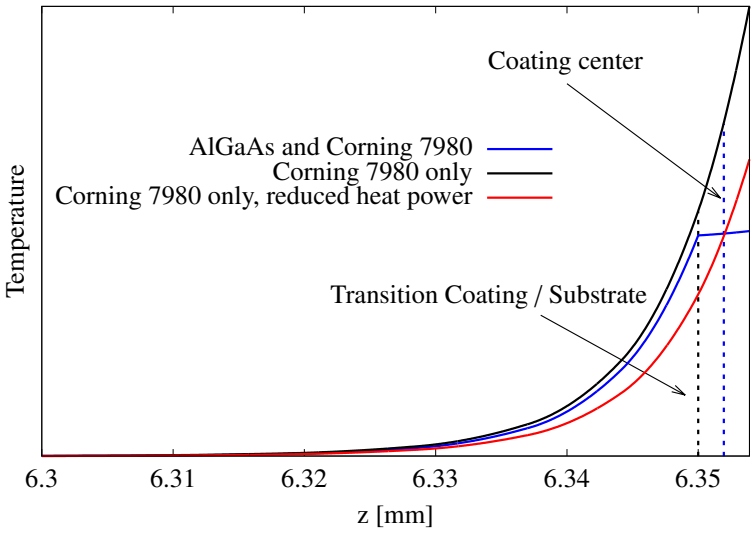

Figure 3.13: Simulation of coating and substrate temperature distributions with COMSOL. This plot shows a cross section of the AlGaAs coating and the Corning 7980 substrate along the z-axis. The coating starts at $z = 6.3539\,\text{mm}$ and ends at $z = 6.35\,\text{mm}$ (marked by the vertical dashed black line). The center of the coating is illustrated by the vertical blue dashed line. The substrate starts at $z = 6.35\,\text{mm}$ and ends at $z = 0\,\text{mm}$. To obtain the power reduction factor for TkSim, three COMSOL simulations were performed. The black curve depicts a COMSOL simulation, where the coating and the substrate material parameters were set to Corning 7980. For the generation of the blue graph, the coating parameters were set to AlGaAs. Due to its large thermal conductivity, the AlGaAs coating first spreads the heat in radial direction. Thus, the temperature in z-direction is reduced. To model this effect, the coating material parameters were again set to Corning 7980 and the power of the inward heat flux was reduced, resulting in the red curve. The red curve approximates the area below the blue curve and thus, the heat input caused by the AlGaAs coating into the Corning 7980 substrate.

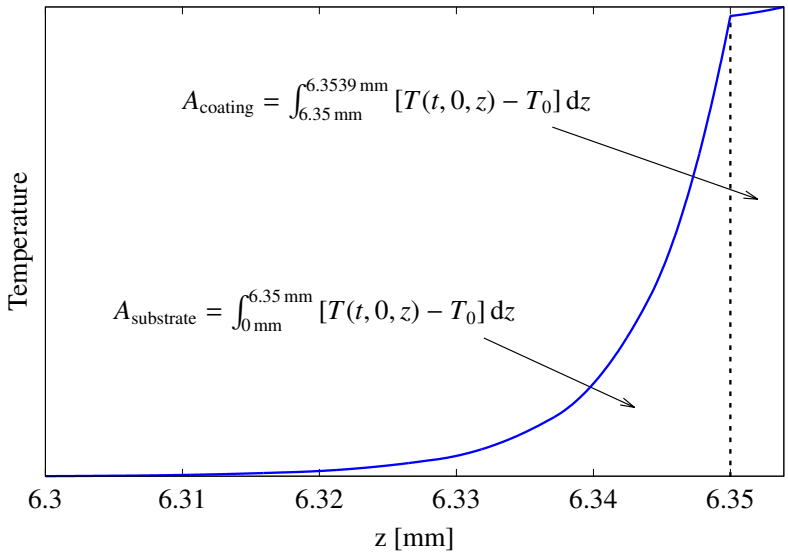

Figure 3.14: Determination of the heat input for the AlGaAs coating and the Corning 7980 substrate. The heat input into the coating is determined by the area A_{coating} and the heat input inside of the substrate is given by $A_{\text{substrate}}$. The temperature distribution is the same as in figure 3.13, where it was named 'AlGaAs and Corning 7980'.

3.11 Results at 1064 nm

First, a series of measurements using 82 mW input power and scan frequencies between 23 Hz and 31 Hz was recorded (plot a. in figure 3.15), yielding to scans of the cavity resonance within times between 600 μs and 460 μs. With subsequent COMSOL simulations, the effect of the AlGaAs coating was investigated. From the finite element simulations it was inferred, that the factors by which the laser power in TkSim has to be reduced were between 0.653 and 0.66. Furthermore, the COMSOL simulations determined the weighting of the coating and the substrate thermorefractive and thermoelastic coefficients. The weighting factors were within the intervals of $0.33 \leq C_{\text{coating}} \leq 0.36$ and $0.64 \leq C_{\text{substrate}} \leq 0.67$. Then, each measurement was processed with TkSim. The program varied the quantities R_1, $\widetilde{R_2}$ and α_{C} in order to obtain a numerical fit. The average values of the power reflectivities were $R_1 \approx 99.9529\,\%$ and $\widetilde{R_2} \approx 99.9745\,\%$. The inferred mean value of the coating absorption coefficient was $\alpha_{\text{C}} = (0.39 \pm 0.01)$ ppm.

A second series of measurements was performed with an input power of 163 mW and scan frequencies between 19 Hz and 38 Hz (plot b. in figure 3.15). This resulted in resonance scans with a minimal time of 400 μs and a maximal time of 800 μs. With COMSOL, the inferred power reduction factors were between 0.65 and 0.663. The derived factors for coating and substrate parameter weighting were within the intervals $0.31 \leq$

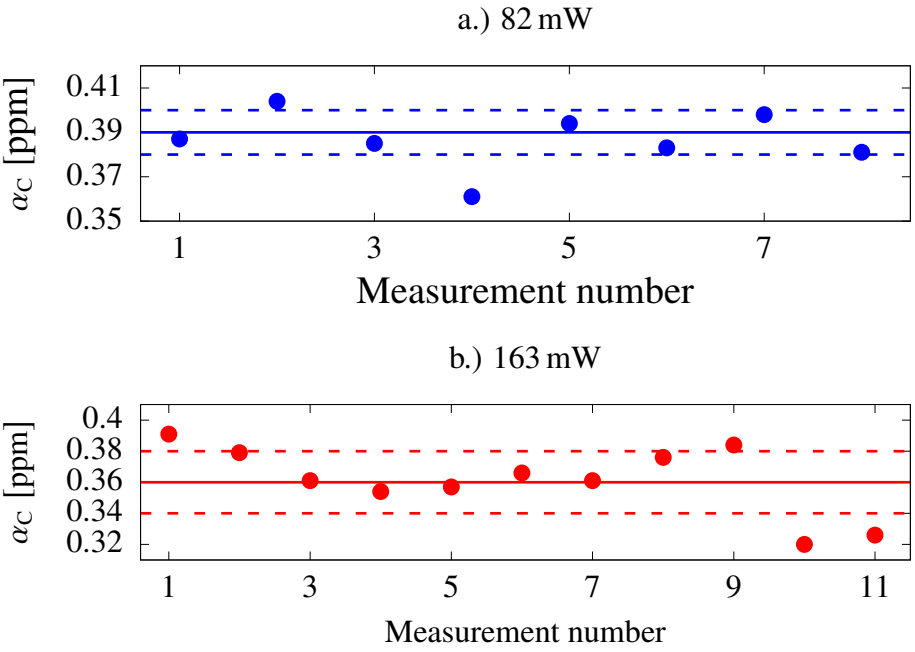

Figure 3.15: AlGaAs coating absorption measurements at 1064 nm. Plot a.) depicts the coating absorption measurements (blue dots) that were performed with an input power of 82 mW and scan frequencies between 23 Hz and 31 Hz. The obtained average value was $\alpha_C = (0.39 \pm 0.01)$ ppm, which is illustrated by the solid blue line. The dashed blue lines represent the standard deviation. Plot b.) shows the coating absorption measurements, carried out with an input power of 163 mW. The used scan frequencies were between 19 Hz and 38 Hz. A mean coating absorption of $\alpha_C = (0.36 \pm 0.02)$ ppm was computed, visualized by the solid red line. The dashed red lines represent the standard deviation. From both measurements, a mean absorption of $\alpha_{C,\,1064\,nm} = (0.38 \pm 0.02)$ ppm was calculated.

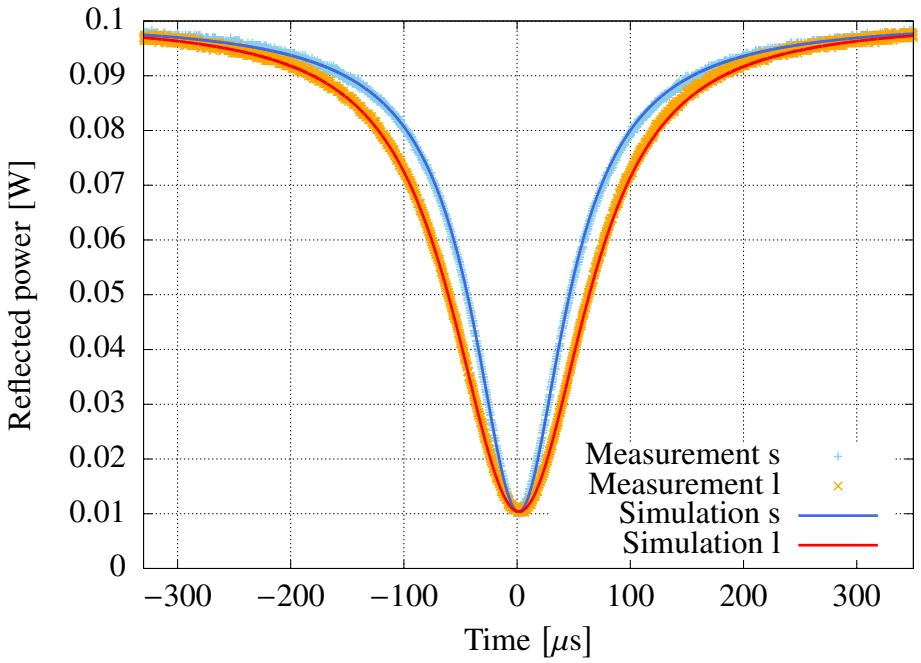

Figure 3.16: Measured and fitted resonance peaks in reflection at 1064 nm. During this measurement, an input power of 163 mW and a scan frequency of 19 Hz was used. A COMSOL simulation yielded a laser power reduction factor of 0.65. Thus, the y-axis is rescaled to a maximum reflected power of 0.1 mW. The blue crosses, correspond to the recorded resonance peak for external shortening of the resonator round-trip length and the solid blue line shows the numerical fit. The orange crosses represent the measured resonance peak for external lengthening of the round-trip length while the solid orange line depicts the corresponding numerical fit.

$C_{\text{coating}} \leq 0.385$ and $0.615 \leq C_{\text{substrate}} \leq 0.69$. Again, each measurement was numerically fitted with TkSim, yielding the power reflectivities $R_1 = (99.9529 \pm 0.0002)$ % and $\widetilde{R_2} = (99.9749 \pm 0.0001)$ %. The inferred coating absorption was $\alpha_C = (0.36 \pm 0.02)$ ppm. Thus, the overall obtained coating absorption at a wavelength of 1064 nm was

$$\alpha_{C,\,1064\,\text{nm}} = (0.38 \pm 0.02)\ \text{ppm}.$$

The calculated finesse of the resonator was $F = (8678 \pm 21)$ and it had a linewidth of (1.92 ± 0.02) MHz.

An example of a numerical fit is shown in figure 3.16 for a measurement with an input power of 163 mW and a scan frequency of 19 Hz. The detected resonance peak for external lengthening of the resonator round-trip length is depicted by the orange crosses and the corresponding numerical fit is given by the solid red line. The measured resonance peak for

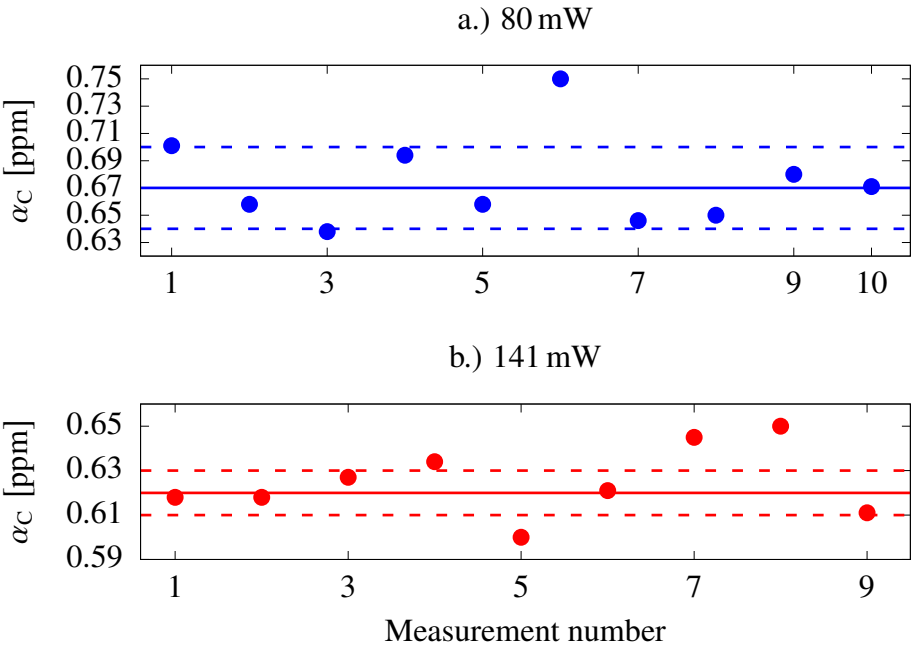

Figure 3.17: AlGaAs coating absorption measurements at 1550 nm. The upper blue plot a.) shows the coating absorption measurements (blue dots) that were performed with an input power of 80 mW and scan frequencies between 24 Hz and 34 Hz. The obtained average value was $\alpha_C = (0.67 \pm 0.03)$ ppm, which is illustrated by the solid blue line. The dashed blue lines represent the standard deviation. The lower red plot b.) shows the coating absorption measurements, carried out with an input power of 141 mW. The used scan frequencies were between 32 Hz and 50 Hz. A mean coating absorption of $\alpha_C = (0.62 \pm 0.01)$ ppm was computed, visualized by the solid red line. The dashed red lines represent the standard deviation. From both measurements, an average absorption of $\alpha_{C,\,1550\,nm} = (0.65 \pm 0.02)$ ppm was calculated.

external resonator round-trip shortening is illustrated by the blue crosses and the numerical fit by the solid blue line.

3.12 Results at 1550 nm

The first series of measurements at 1550 nm was performed with an input power of 80 mW and scan frequencies between 24 Hz and 34 Hz. This resulted in cavity resonance scans between 1200 μs and 800 μs. With COMSOL, the weighting factors for the calculation of the coating and the substrate parameters were within the intervals of $0.39 \leq C_{coating} \leq 0.43$ and $0.57 \leq C_{substrate} \leq 0.61$. For a scan frequency of 1200 μs, the coating contribution had its maximum value of $C_{coating} = 0.43$. The coating contribution decreased for slower scan

frequencies. The inferred power reduction factors were between 0.61 and 0.62. For each measurement, a numerical fit with TkSim was obtained, yielding the average power reflectivities of $R_1 = (99.9637 \pm 0.0002)$ % and $\widetilde{R_2} = (99.9699 \pm 0.0001)$ % and a mean coating absorption of $\alpha_C = (0.67 \pm 0.03)$ ppm.
The second series of measurements was carried out with a laser input power of 141 mW and scan frequencies between 32 Hz and 50 Hz, yielding to resonance scanning times between 900 μs and 600 μs. With COMSOL simulations, laser power reduction factors between 0.62 and 0.64 were derived. The inferred factors determining the weighting of coating and substrate parameters were within the intervals of $0.42 \leq C_{\text{coating}} \leq 0.46$ and $0.54 \leq C_{\text{substrate}} \leq 0.58$. Subsequent numerical fits with TkSim resulted in the mean power reflectivities of $R_1 = (99.9632 \pm 0.0002)$ % and $\widetilde{R_2} = (99.9709 \pm 0.0001)$ %. The obtained coating absorption was $\alpha_C = (0.62 \pm 0.01)$ ppm. Thus, the overall coating absorption at 1550 nm was calculated to

$$\alpha_{C,\,1550\,\text{nm}} = (0.65 \pm 0.02) \text{ ppm}.$$

The FWHM of the used resonator was computed to (1.75 ± 0.03) MHz and its finesse was $F = (9508 \pm 28)$.

3.13 Summary and conclusion

In this chapter, absorption measurements on AlGaAs coatings at 1064 nm and 1550 nm, performed with the photothermal self-phase-modulation technique, were presented. Due to the large thermal conductivity of AlGaAs, finite element simulations with COMSOL Multiphysics were performed to investigate the effect of the AlGaAs coating on the temperature distribution inside of the Corning 7980 substrate. The obtained result was, that the AlGaAs coating led to a decreased heat flux in direction of the optical axis. Furthermore, the thermorefractive coefficient of AlGaAs is about 31 times larger than the one of Corning 7980 and the thermoelastic coefficient of AlGaAs is a factor of 10.5 larger. Thus, these coating parameters needed to be included in the numerical fits which were performed with TkSim. By means of further COMSOL simulations, weighting factors for the thermorefractive and thermoelastic coefficients of AlGaAs and Corning 7980 were derived. The coating contribution at 1064 nm to the parameter weighting was between 31 % and 38 %. The AlGaAs coating caused a reduction of the inward heat flux into the substrate by factors between 0.61 and 0.65. At 1550 nm, the coating contribution to the material parameters was between 39 % and 46 %. Furthermore, the AlGaAs coating led to a decrease of the inward heat flux into the mirror substrate by factors between 0.61 and 0.663.

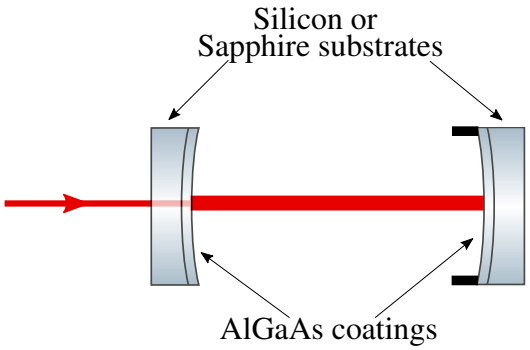

Figure 3.18: AlGaAs resonator with silicon or sapphire substrates. By employing substrate materials with a large thermal conductivity, like silicon or sapphire, the heat is faster conducted from the coating into the substrate.

At 1064 nm, a coating absorption of $\alpha_{\mathrm{C},\,1064\,\mathrm{nm}} = (0.38 \pm 0.02)$ ppm was measured and at 1550 nm, a coating absorption of $\alpha_{\mathrm{C},\,1550\,\mathrm{nm}} = (0.65 \pm 0.02)$ ppm was obtained.
To validate the measured absorption coeffcient at 1064 nm, the absorption of the same AlGaAs coating, specified at 1064 nm, was measured by Jessica Steinlechner in Glasgow with photothermal common-path interferometry [7], yielding a result of (3.0 ± 0.5) ppm. This result is almost a factor 8 larger than the absorption coefficient of (0.38 ± 0.02) ppm, inferred in this work. However, the reason for this deviation could not be identified.
To reduce the discrepancy between the Glasgow data and the measurements presented in this work, the following changes are suggested. In our method, the cause for the small obtained coating absorption coefficient was the large contribution of the thermorefractive coefficient of AlGaAs. At 1064 nm, its minimal contribution to the overall thermorefractive coefficient was 31 % and at 1550 nm, the minimal contribution was 39 %. The reason for the large AlGaAs contribution was the integrated temperature inside of the AlGaAs coating, performed with equation (3.36). In our case, the AlGaAs coating with a thermal conductivity of 63 W/mK was bonded to a Corning 7980 mirror substrate with a thermal conductivity of 1.38 W/mK. Due to the large difference in the thermal conductivities of both materials, the heat could not be conducted quickly into the mirror substrate. To reduce the coating contribution, a mirror substrate material with a larger thermal conductivity needs to be chosen for future experiments. Suitable substrate materials are silicon or sapphire. At room temperature, silicon has an average thermal conductivity of 142 W/mK ([82], p. 263) and the one of sapphire is 46 W/mK ([82], p. 263). An optical resonator, suited for future AlGaAs coating absorption measurements with the photothermal self-phase modulation technique is shown in figure 3.18. The mirror substrates are either made of silicon or

sapphire. On each substrate, an AlGaAs coating is bonded. The optical absorption of both AlGaAs coatings can be detected and also their scatter losses can be inferred by means of cavity round-trip loss measurements.

Chapter 4

Absorption measurements on sapphire at 1064 nm

4.1 Introduction

Entanglement describes a quantum mechanical state where two (or more) precisely defined subsystems, which can be arbitrarily far away from each other, do not have individual properties with respect to a third party. The entangled properties of the systems are however, precisely defined with respect to each other. In the 'MassQ project', it is planned to create and observe entanglement of the positions and momenta of two masses A and B in the kg-regime [69]. 2008 Müller-Ebhardt et al. [58] suggested a power-recycled Michelson interferometer as feasible setup to produce this kind of entanglement between the interferometer end test masses. Reference [69] proposed a Michelson-Sagnac-interferometer cooled to cryogenic temperatures as favorable topology.

One test mass candidate for the MassQ project is sapphire. Compared to fused silica, its only advantage at 300 K is the higher thermal conductivity while other properties as thermal expansion coefficient, thermorefractive coefficient and mechanical loss have larger values (see reference [82], p. 263 for details). However, this changes at cryogenic temperatures. At 20 K, the thermal conductivity of sapphire has a maximum of 20000 W/mK and decreases to 2900 W/mK at 10 K. Due to the small thermorefractive coefficient of $\mathrm{d}n/\mathrm{d}T \leq 9 \cdot 10^{-8}\,1/\mathrm{K}$ at temperatures below 30 K, thermal lensing and substrate thermorefractive noise are strongly reduced. Furthermore, the thermal expansion of sapphire and thus, also the thermoelastic noise is minimized at 10 K since the coefficient of thermal expansion drops to $a_{\mathrm{th}} = 1 \cdot 10^{-9}\,1/\mathrm{K}$. All parameter values at cryogenic temperatures were taken from ([82], p. 263).

To enable the cryogenic test mass cooling in MassQ, the heat generated by coating as well as by substrate absorption of light power needs to be minimized, because the employed

cryostat can only provide a certain amount of cooling power. The aimed substrate absorption level is below 30 ppm/cm. Thus, a first step is to find sapphire substrates and investigate their optical absorption at 300 K.
In this chapter, absorption measurements on a 3 cm long and on a 10 cm long monolithic sapphire resonator at 1064 nm are presented. The substrate absorption was obtained by means of resonator round-trip loss measurements at a temperature of 300 K.

4.2 Determination of the sapphire substrate absorption at 1064 nm via cavity round-trip loss measurements

4.2.1 Experimental setup and measurement method

In this section, the cavity-based round-trip loss measurements used to derive the bulk absorption coefficient α_s are shown. The investigated sapphire was produced by the company IMPEX. The loss measurements were performed on two monolithic sapphire cavities with geometrical lengths of 3 cm and 10 cm. Both cavities were fabricated from the same ingot. The end faces of both cavities were polished to have radii of curvature of 2 m in order to satisfy the stability criterion described by equation (3.4). For both cavities, the in-coupling face was coated with a power reflectivity of $R_1 = 99.6\%$ and the end face with $R_2 = 99.8\%$. The coatings were manufactured and applied by LASEROPTIK. A schematic of the experimental setup can be found in figure 4.1. The measurements were made with a Mephisto Laser that was manufactured by Coherent. It radiated monochromatic continuous-wave laser light at 1064 nm with a maximum output power of 1.2 W. At certain combinations of pump current and laser crystal temperature, the Mephisto laser emitted two fundamental modes at the same time. To ensure the emission of a single fundamental mode, the laser was operated at a pump current of 2.17 A and a crystal temperature of 30.74 °C. To scan the monolithic sapphire cavities, the frequency of the laser was changed using a function generator and a high voltage amplifier that acted on the PZT of the laser. The electro-optical modulator (EOM) imprinted phase-modulated sidebands at a frequency of 30 MHz on the laser light. The Faraday rotator (FR) separated incoming and reflected light and the photo diode PD_1 measured the cavity resonance peaks in reflection. Together with photo diode PD_1 which had an included mixer, the EOM was used to create an out of phase Pound-Drever-Hall [29] error signal. This error signal was used for the calibration of the time axis of the measured resonance peaks. The photo diode PD_2 in transmission of the sapphire cavity monitored the mode-matching of the laser beam to the cavity.

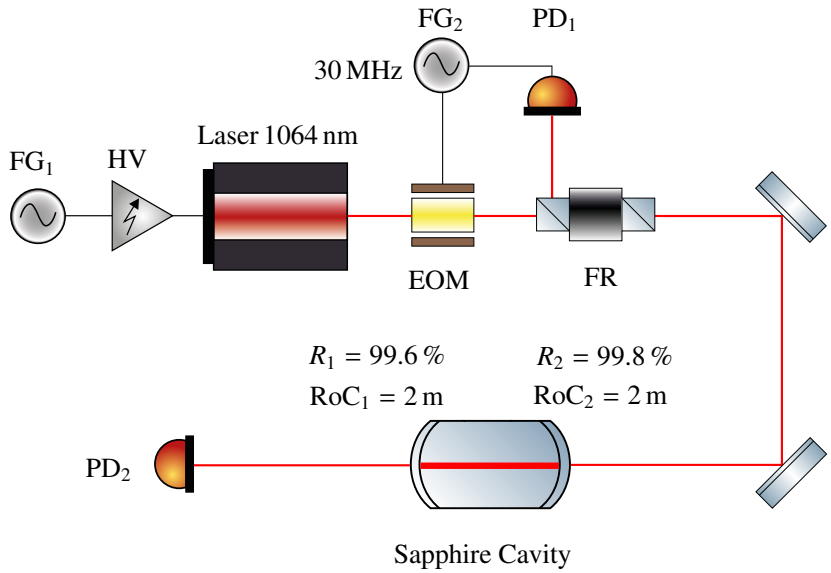

Figure 4.1: Schematic of the sapphire round-trip loss measurement setup. A continuous-wave 1064 nm laser was used to measure the round-trip losses of a monolithic sapphire cavity. The laser frequency was changed by a combination of function generator (FG_1) and a high voltage amplifier (HV) in order to scan the cavity. Incoming and reflected laser light were separated with a Faraday rotator (FR). Resonance peaks in reflection were measured with PD_1 and numerically fitted with the program TkSim to determine the reflectivities and calculate the round-trip losses. The combination of function generator (FG_2), electro-optical modulator (EOM) and PD_1 created an out of phase error signal using the Pound-Drever-Hall technique that was used to calibrate the time axis of the measured resonance peaks.

To determine the cavity round-trip losses, the sapphire cavity was scanned for an increasing and for a decreasing laser frequency. For each scan frequency, a pair of cavity resonance peaks in reflection (one for each scan direction) was measured with photo diode PD_1. For each measurement, the pair of resonance peaks was numerically fitted with the program Tksim ([50], pp. 69 – 91). Tksim varied the values for the mirror reflectivities R_1 and $\widetilde{R_2}$ to minimize the difference between simulated and measured data in order to gain a fit. Here, R_1 is the reflectivity of the in-coupling mirror M_1 and $\widetilde{R_2}$ corresponds to the effective reflectivity of mirror M_2. $\widetilde{R_2}$ includes all cavity round-trip losses except of the transmission of M_1. For the round-trip loss measurement, first the reflectivity R_1 and the effective reflectivity $\widetilde{R_2}$ were determined with the program TkSim for the case where M_1 was the in-coupling mirror of the sapphire cavity. In a second measurement, the sapphire cavity was turned and the reflectivity R_2 and the effective reflectivity $\widetilde{R_1}$ were measured. The overall intra-cavity round-trip losses which were caused by absorption and scattering of the sapphire substrate and absorption and scattering of the two coatings can be calculated as

$$L_{\mathrm{RT}} = |R_1 - \widetilde{R_1}| = |R_2 - \widetilde{R_2}|. \tag{4.1}$$

Note that the reflectivity without the tilde is always the one from the in-coupling mirror and the one with the tilde is the reflectivity of the end mirror.

4.2.2 Measurements on the 3 cm sapphire cavity

First, a series of 15 measurements with scan frequencies between 35 Hz and 45 Hz was carried out using 4 mW 1064 nm laser input power and M_1 as in-coupling mirror. The time in which the full width half maximum of the cavity resonance was scanned was between 1228 μs and 950 μs. After numerically fitting the recorded resonance peaks in reflection, the reflectivities and their standard deviations were calculated to

$$R_1 = (99.626 \pm 0.001)\,\% \text{ and } \widetilde{R_2} = (98.095 \pm 0.009)\,\%.$$

This is depicted in figure 4.2. The FWHM of the 3 cm long sapphire cavity was $\Delta f \approx 10.5$ MHz and together with the FSR of 2.86 GHz, a finesse of $F = 273.4$ was calculated. Figure 4.3 shows an example of such a numerical fit. The depicted resonance peaks were recorded for an increasing laser frequency (orange crosses) as well as for a decreasing laser frequency (blue crosses). The solid red line represents the numerical fit with TkSim.
Then the cavity was turned and M_2 was treated as in-coupling mirror and a light power

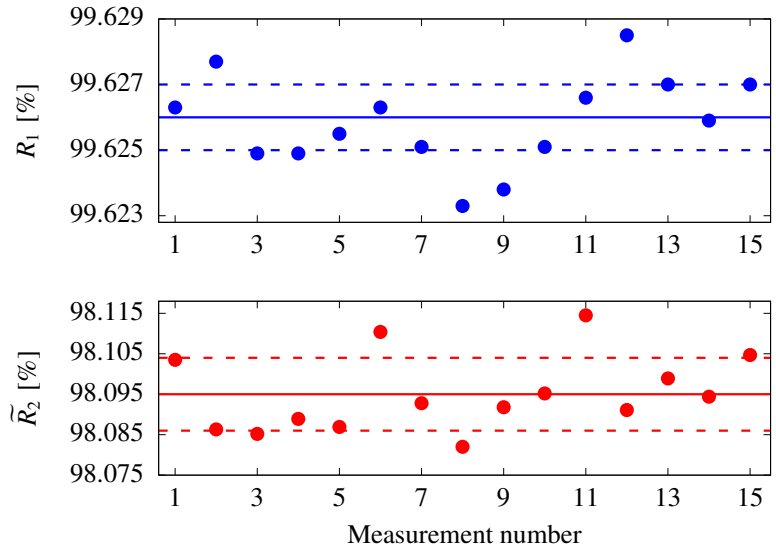

Figure 4.2: Results of the reflectivities R_1 and $\widetilde{R}_2$ of the 3 cm sapphire cavity. Here, mirror M_1 was used as in-coupling mirror and 15 measurements were carried out, using an input laser power of 4 mW. The dots depict single measurements at different scan frequencies, the solid lines are the average reflectivities and the dashed lines represent the standard deviation. $R_1 = (99.626 \pm 0.001)\,\%$ (blue) and $\widetilde{R}_2 = (98.095 \pm 0.009)\,\%$ (red) were obtained.

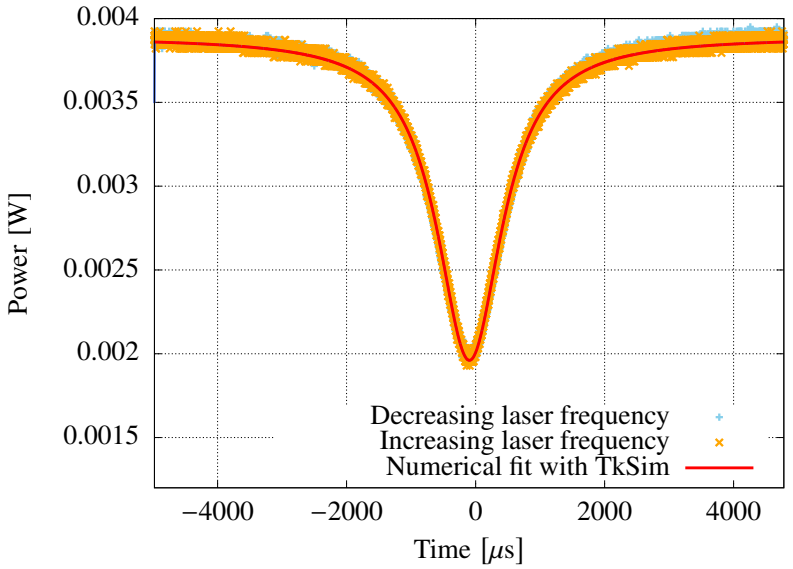

Figure 4.3: Example of in reflection measured and fitted resonance peaks. The orange crosses correspond to a measured resonance peak, where the laser frequency was increased. The blue crosses are related to a resonance scan, where the laser frequency was decreased. Both resonance peaks were recorded using a laser input power of 4 mW and a scan frequency of 35 Hz. The solid red line represents the numerical fit with TkSim. In this measurement, mirror M_1 was used as in-coupling mirror.

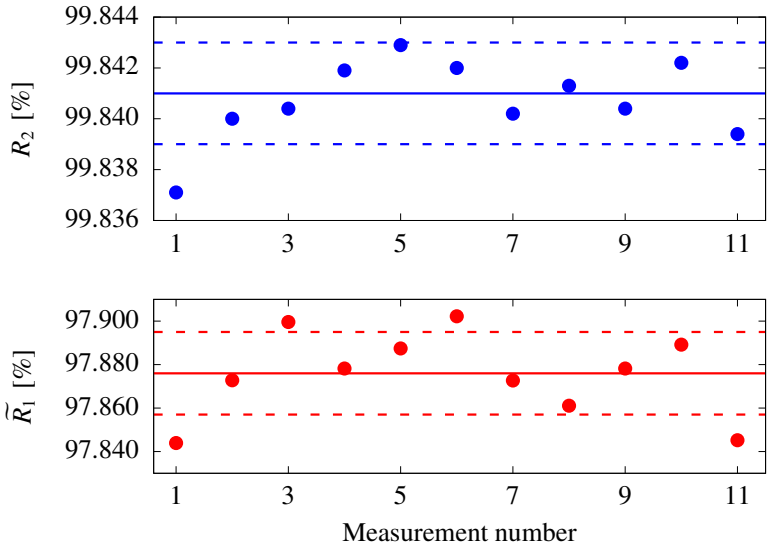

Figure 4.4: Results of the reflectivities R_2 and $\widetilde{R_1}$ of the 3 cm sapphire cavity. Here, mirror M_2 was used as in-coupling mirror and 11 measurements were performed with an input laser power of 7 mW. The average reflectivities $R_2 = (99.841 \pm 0.002)\,\%$ (blue) and $\widetilde{R_1} = (97.876 \pm 0.019)\,\%$ (red) and their standard deviations are illustrated as solid lines and dashed lines, respectively. The dots show the single measurements.

of 7 mW was mode-matched into the cavity. 11 measurements with scan frequencies between 30 Hz and 40 Hz were recorded, resulting in scans over the full width half maximum between 1140 μs and 854 μs. The data evaluation yielded

$$R_2 = (99.841 \pm 0.002)\,\% \text{ and } \widetilde{R_1} = (97.876 \pm 0.019)\,\%.$$

The reflectivities and their standard deviations are presented in figure 4.4. The cavity round-trip losses were computed to

$$L_{3\text{cm},1} = |R_1 - \widetilde{R_1}| = |\,(99.626 \pm 0.002)\,\% - (97.876 \pm 0.019)\,\%| = (1.75 \pm 0.02)\,\% \text{ and}$$
$$L_{3\text{cm},2} = |R_2 - \widetilde{R_2}| = |\,(99.841 \pm 0.002)\,\% - (98.095 \pm 0.009)\,\%| = (1.75 \pm 0.01)\,\%.$$

Thus, the average round-trip loss for the monolithic 3 cm long sapphire resonator (without the transmissions of the two coatings) was

$$\overline{L_{3\text{cm}}} = (1.75 \pm 0.02)\,\% \;\Leftrightarrow \overline{L_{3\text{cm}}} = (2917 \pm 33)\,\frac{\text{ppm}}{\text{cm}}.$$

4.2.3 Measurements on the 10 cm sapphire cavity

Using M_1 as in-coupling mirror, 9 measurements with scan frequencies between 20 Hz and 30 Hz were made with a laser input power of 15 mW. The time needed to scan the full width

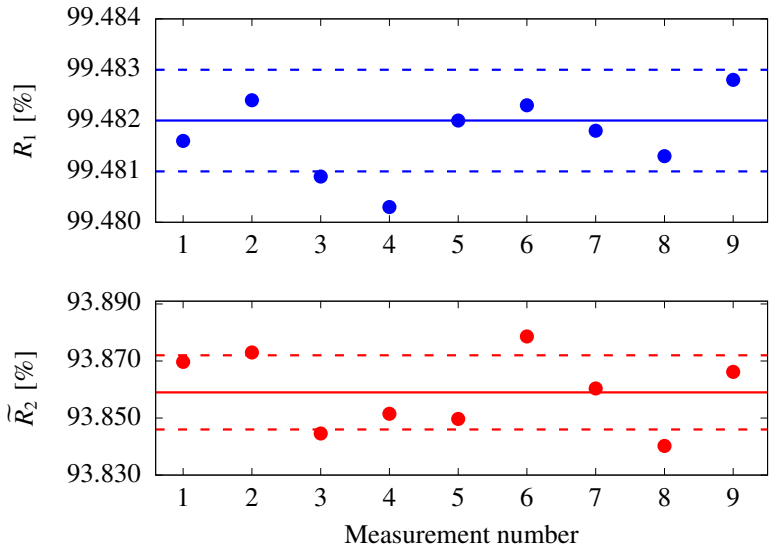

Figure 4.5: Results of the reflectivities R_1 and $\widetilde{R}_2$ of the 10 cm sapphire cavity. Here, mirror M_1 was taken as in-coupling mirror and 9 measurements were performed while a laser power of 15 mW was injected. The obtained average reflectivities and their standard deviations were $R_1 = (99.482 \pm 0.001)\,\%$ (blue) and $\widetilde{R}_2 = (93.859 \pm 0.013)\,\%$ (red). They are depicted as solid lines and dashed lines, respectively, while the dots show the single measurements.

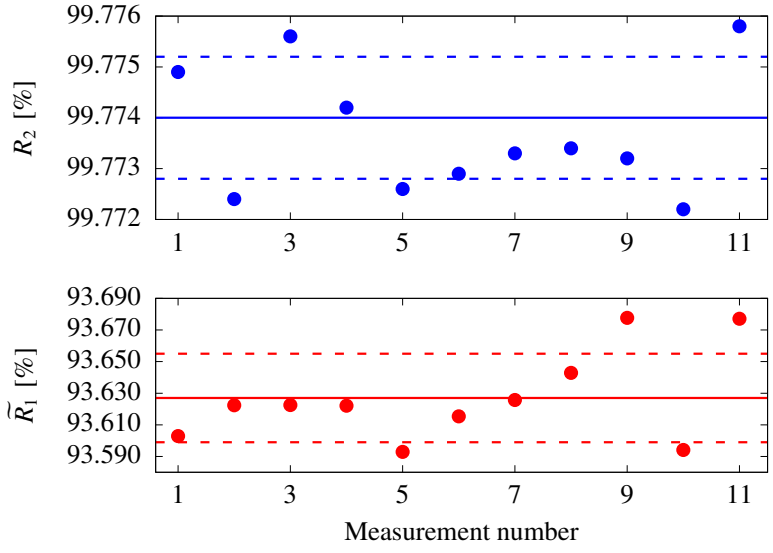

Figure 4.6: Results of the reflectivities R_2 and $\widetilde{R}_1$ of the 10 cm sapphire cavity. Here, mirror M_2 was used as in-coupling mirror and 11 measurements (dots) were carried out with an incident laser power of 11 mW. The calculated reflectivities $R_2 = (99.774 \pm 0.001)\,\%$ and $\widetilde{R}_1 = (93.627 \pm 0.028)\,\%$ and their standard deviations are shown as solid and dashed lines.

half maximum of the cavity was between 1923 μs and 1174 μs. As shown in figure 4.5, the data evaluation of the recorded and fitted resonance peaks yielded the average reflectivities of

$$R_1 = (99.482 \pm 0.001)\,\% \text{ and } \widetilde{R_2} = (93.859 \pm 0.013)\,\%.$$

After turning the sapphire cavity, 11 measurements with scan frequencies between 10 Hz and 15 Hz were carried out using 11 mW laser input power. The time needed to scan the full width half maximum of the cavity was between 3980 μs and 2650 μs. The average reflectivities and their standard deviations were calculated to

$$R_2 = (99.774 \pm 0.001)\,\% \text{ and } \widetilde{R_1} = (93.627 \pm 0.028)\,\%.$$

Thus, the round-trip losses were

$$L_{10\text{cm},1} = |R_1 - \widetilde{R_1}| = |\,(99.482 \pm 0.001)\,\% - (93.627 \pm 0.028)\,\%| = (5.86 \pm 0.03)\,\% \text{ and}$$
$$L_{10\text{cm},2} = |R_2 - \widetilde{R_2}| = |\,(99.774 \pm 0.001)\,\% - (93.859 \pm 0.013)\,\%| = (5.92 \pm 0.01)\,\%.$$

The average round-trip loss for the monolithic 10 cm long sapphire resonator (without the transmissions of the two coatings) was

$$\overline{L_{10\text{cm}}} = (5.89 \pm 0.02)\,\% \;\Leftrightarrow \overline{L_{10\text{cm}}} = (2945 \pm 10)\,\frac{\text{ppm}}{\text{cm}}.$$

4.2.4 Results

Both cavity round-trip loss measurements, $\overline{L_{3\text{cm}}} = (2917 \pm 33)$ ppm/cm and $\overline{L_{10\text{cm}}} = (2945 \pm 10)$ ppm/cm included absorption and scattering of the sapphire substrate itself and absorption and scattering due to the two applied coatings. Here, multilayer coatings consisting of silica and tantalum pentoxide were used. Their absorption was for example determined in [77] to $\alpha_{\text{coat}} = (24.4 \pm 3.2)$ ppm and their scatter loss is between 7 ppm and 21 ppm [31]. A sapphire scatter loss of 13 ppm/cm at 1064 nm was measured in [16]. Since all these contributions were small compared to $\overline{L_{3\text{cm}}}$ and $\overline{L_{10\text{cm}}}$, the round-trip loss was treated as loss due to absorption. Therefore the overall substrate absorption coefficient was

$$\alpha_{\text{IMPEX},2013} = (2931 \pm 22)\,\text{ppm/cm}.$$

4.2.5 Summary and conclusion

For the planned MassQ project, a test mass material with low substrate power absorption is needed in order to enable cryogenic cooling of the test masses. Due to its large thermal conductivity and small thermorefractive and thermoelastic coefficients at cryogenic temperatures, sapphire is a suitable test mass material. In this chapter, the substrate absorption of two sapphire samples at a wavelength of 1064 nm was determined by means of cavity round-trip loss measurements. The measurements were performed on a 3 cm and a 10 cm long sapphire cavity and yielded a bulk absorption of (2931 ± 22) ppm/cm. Compared to other bulk absorption measurements of 40 ppm/cm and $(3 - 140)$ ppm/cm reported in [8, 85], the substrate absorption found in this work is very high. The reason for the large absorption could not be identified with our measurement method. Such a large absorption could result in thermal lensing inside of the test mass substrate as well as in thermal expansion. Because the used cryostat can only extract a certain amount of heat power, a large absorption would also set a limit for the cryogenic test mass operation. Thus, we can conclude that the measured substrate absorption is too high for a use in the MassQ project. In order to find a suitable test mass with low absorption, more sapphire substrates from different manufacturers need to be investigated.

Chapter 5

Summary and conclusions

Strongly squeezed vacuum states generated by means of the cascaded optical Kerr effect can be used for the generation of Wigner functions with a non-gaussian probability distribution. In the first part of this thesis, the production of squeezed vacuum states with the cascaded optical Kerr effect at a wavelength of 1550 nm was demonstrated. The resonator for the production of the squeezed states was a four-mirror bow-tie resonator which contained a PPKTP crystal. First, the conversion from the fundamental 1550 nm to the SHG light was detected. The first conversion minimum was found at a crystal temperature of 61.2 °C and the second at 81.8 °C. A conversion maximum was measured at 40.5 °C. The occurrence of the cascaded optical Kerr effect was observed in the first SHG conversion minimum by detecting the deformed resonance peaks in transmission of the bow-tie resonator. A thermally-induced resonance peak deformation was excluded by fast resonance scans where the FWHM of the bow-tie resonator was crossed within times of 3.7 μs and 5.5 μs. To furthermore verify the dependence of the resonance peak deformation on the fundamental pump power, the deformed resonances peaks in transmission were detected for light powers between 77.8 mW and 102.2 mW. It was observed, that a larger pump power leads to a stronger resonance peak deformation. At a sideband frequency of 358.26 MHz a squeezed variance of (2.0 ± 0.1) dB and an anti-squeezed variance of (9.5 ± 0.1) dB were measured using a fundamental pump power of 85 mW and a crystal temperature of 61.2 °C. The total optical losses including phase noise were 61 %. At a sideband frequency of 1074.78 MHz a non-classical noise reduction of (2.5 ± 0.1) dB was measured with a pump power of 120 mW. In separate measurements, squeezing produced by the cascaded optical Kerr effect in the first and second SHG conversion minimum was distinguished from squeezing of the fundamental field by the SHG process that was observed in the SHG conversion maximum. The measured Kerr squeezed vacuum states were mainly limited by acoustically-induced phase noise and by optical losses. The phase noise can be decreased by a more stable squeezing resonator design and by placing the squeezing resonator on

top of a mechanical damping stage. To further reduce the impact of acoustically-induced vibrations, the squeezing resonator should be operated in vacuum.

In the second part of this thesis, the optical absorption of multilayer coatings made of GaAs and $Al_{0.92}Ga_{0.08}As$ that were bonded on a Corning 7980 mirror substrate was measured at 1064 nm and 1550 nm. These coatings are a promising candidate to reduce the coating thermal noise in high-precision experiments such as gravitational-wave detectors. The employed measurement method was the photothermal self-phase modulation technique that is based on the thermal Kerr effect. The coating under investigation was placed inside an optical two-mirror resonator and resonance peaks showing thermally-induced deformations were measured in reflection and fitted. The fit was obtained by means of a time-domain simulation that varied the mirror power reflectivities R_1, R_2 and the coating absorption coefficient α_C to gain a fit. Because the thermal conductivity of AlGaAs is 46 times larger than the thermal conductivity of the Corning 7980 substrate and the thermorefractive and thermoelastic coefficients of AlGaAs are 31 times and 10.5 times larger compared to Corning 7980, the coating parameters needed to be included in our time-domain simulation. The effect of the AlGaAs coating on the temperature distribution inside of the Corning 7980 mirror substrate as well as the weighting factors between coating and substrate material parameters was obtained by means of finite element simulations that were performed with COMSOL Multiphysics. At 1064 nm, the coating contribution to the overall material parameters was between 31 % and 38 %. Furthermore, the AlGaAs coating led to a reduction of the inward heat flux into the substrate by factors between 0.61 and 0.65. With these results, the optical coating absorption at 1064 nm was determined to be (0.38 ± 0.02) ppm. At 1550 nm, the coating contribution to the overall material parameters was between 39 % and 46 % and the AlGaAs coating caused a reduction of the inward heat flux into the mirror substrate by factors between 0.61 and 0.663. With these values, a coating absorption of (0.65 ± 0.02) ppm was inferred. The measurement of the AlGaAs coating specified at 1064 with photothermal-common-path interferometry led to a result of (3.0 ± 0.5) ppm. To reduce the discrepancy between the two results, mirror substrates with a larger thermal conductivity such as sapphire or silicon should be used when measuring with the photothermal self-phase modulation technique.

Due to its large thermal conductivity and small thermorefractive and thermoelastic coefficients at cryogenic temperatures, sapphire is a suitable test mass material for optomechanical experiments. In the third part of this thesis, the optical absorption of two sapphire substrates from the same ingot was measured by means of cavity-based round-trip loss measurements. As a first step, the absorption measurements were made at room temperature. The obtained substrate absorption coefficient was (2931 ± 22) ppm/cm. Such a high

substrate absorption could lead to large increased temperatures inside of the mirror substrates. As a result, thermal lensing and thermally-induced test mass deformations because of thermal expansion can occur. Due to the limited cooling power of the employed cryostat, the cryogenic test mass operation would be restricted. Thus, more sapphire substrates need to be investigated to find substrates with an optical absorption of about 30 ppm/cm or below.

Appendix A

GHz bandwidth homodyne detector spectrum

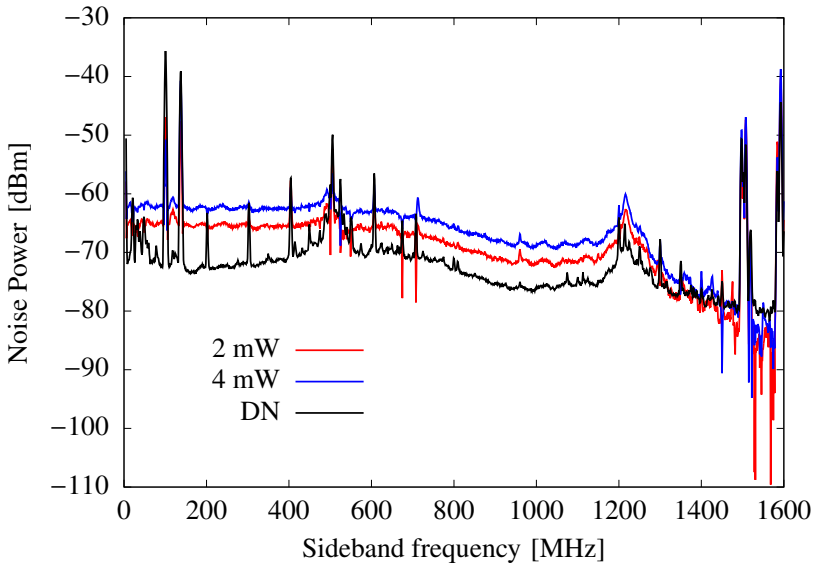

Figure A.1: Measured spectrum of the GHz-bandwidth homodyne detector.

The spectrum of the homodyne detector was measured for local oscillator powers of 2 mW (red) and 4 mW (blue), while the signal path was blocked. Doubling the local oscillator power resulted in an increase of the noise power level of 3 dB. This showed, that the squeezing measurement was vacuum noise limited and the homodyne detector behaved linear. Both spectra were dark noise corrected. The detector dark noise is shown in black. The dominant peaks in the spectrum are the modulation frequencies of 20.9 MHz, 101 MHz and 138 MHz, which were used for the length-stabilization of several optical resonators. Higher order harmonics of this frequencies were also observed.

Appendix B

Input Parameters of TkSim

The input parameters of TkSim [49], ([75], pp. 36 – 39) are listed in table B.1. The section 'Laser' consists of the incident laser power P, the laser wavelength λ and the beam waist w_0 of the used resonator. The section 'Cavity' includes parameters about the used resonator and the resonator scan. *mm* is the fraction of the power P which is coupled into the resonator and s denotes the geometrical mirror spacing. $\mathrm{NFSR_i}$ and $\mathrm{NFSR_d}$ are the number of FSRs scanned for increasing or decreasing resonator round-trip length and Ω_s is the scan frequency. $\mathrm{delta_{start}}$ is the initial resonator detuning and $\mathrm{delta_{range}}$ describes the complete scanned range. R_1 and R_2 are the power reflectivities of mirror $\mathrm{M_1}$ and $\mathrm{M_2}$. The section 'Measurement' contains the parameters $\mathrm{shift_i}$ and $\mathrm{shift_d}$, which are time-axis offsets to superimpose the measured and the simulated resonance peaks for increasing and for decreasing resonator length as well as the parameter ref-val. The latter is used to convert the measured photo diode signal in Volts into a signal in Watt. The section 'Mirror 1' consists of the material parameters of the mirror substrate. n is the refractive index, $\mathrm{d}n/\mathrm{d}T$ is the thermorefractive coefficient and a_th the coefficient of thermal expansion. c_w, k_th and ρ are the specific heat, the thermal conductivity and the density of the substrate material and L_s and R_s denote the length and the radius of the mirror substrate. α_c is the coating power absorption coefficient of the in-coupling mirror $\mathrm{M_1}$ and ϵ is the emissivity, which is set to 1. The section 'Control' incorporates parameters which determine the precision of the calculations performed by TkSim. The parameter xRes determines the number of data points used for a plot of the measured and simulated resonance peaks. The parameters pstep and mstep determine the upper bounds of the summations of equation (27) from reference [40], which is used to compute the transient temperature profile in the mirror substrate of $\mathrm{M_1}$. Every Tstep round-trip, the temperature profile is calculated again with the accuracy given by TEPS. T_0 is the environment temperature and the parameter phiFactor determines the number of mirrors which expand into the resonator.

Laser	
P [W]	Laser power
λ [m]	Laser wavelength, 1064 nm or 1550 nm
w_0 [m]	Resonator waist, 150 μm or 181 μm
Cavity	
mm	Amount of light injected into the resonator
s [m]	Distance between both mirrors, 0.009 m
$\mathrm{NFSR_i}$	Number of FSRs scanned (increasing ramp)
$\mathrm{NFSR_d}$	Number of FSRs scanned (decreasing ramp)
Ω_s [Hz]	Scan frequency
$\mathrm{delta_{start}}$ [FWHM]	Initial resonator detuning, -4
$\mathrm{delta_{range}}$ [FWHM]	Scanned range, 8
R_1	Power reflectivity of mirror $\mathrm{M_1}$
R_2	Power reflectivity of mirror $\mathrm{M_2}$
Measurement	
$\mathrm{shift_i}$	Offset along the time axis (increasing ramp)
$\mathrm{shift_d}$	Offset along the time axis (decreasing ramp)
ref-val	Factor for the photo diode calibration in reflection
Mirror 1	
n	Refractive index, 1.45 [28], 1.44 [28]
$\mathrm{d}n/\mathrm{d}T$ [1/K]	Thermorefractive coefficient, $8.6 \cdot 10^{-6}$ 1/K [28], $8.57 \cdot 10^{-6}$ 1/K [28]
a_th [1/K]	Coefficient of thermal expansion, $5.2 \cdot 10^{-7}$ [25]
c_w [J/kgK]	Specific heat, 703 J/kg [54]
k_th [W/mK]	Thermal conductivity, 1.38 W/mK [54]
ρ [kg/m^3]	Density, 2203 kg/m^3 [54]
α_c	Coating power absorption coefficient
L_s [m]	Length of the mirror substrate, 0.00635 m
R_s [m]	Radius of the mirror substrate, 0.0127 m
ϵ	Emissivity, 1
Control	
xRes	Number of data points used in the plot, 6000
pstep, mstep	Upper limits for the summations in equation 27 from reference [40], set to 100 and 1
Tstep	Every Tstep round-trip, the temperature profile is computed again, 6000
TEPS	Accuracy of the temperature profile calculation, $1 \cdot 10^{-6}$
T_0 [K]	Environment temperature, 293.15 K
phiFactor	Number of mirrors expanding into the resonator, 1

Table B.1: List of input parameters for the time-domain simulation TkSim [49], ([75], pp. 36 – 39).

Appendix C

Calculation of the AlGaAs coating material parameters

C.1 Material Parameters at 1064 nm

	GaAs	$Al_xGa_{1-x}As$	$Al_{0.92}Ga_{0.08}As$
n	3.48 [26]		2.977 [26]
k_{th} [W/mK]	55 [44]	$0.55 - 2.12x + 2.48x^2$ [42]	69.9
c_w [J/kgK]	330 [44]	$0.33 + 0.12x$ [42]	440
ρ [kg/m^3]	5320 [43]	$5.32 - 1.56x$ [41]	3884.8
a_{th} [1/K]	$5.73 \cdot 10^{-6}$ [44]	$(5.73 - 0.53x) \cdot 10^{-6}$ [42]	$5.24 \cdot 10^{-6}$
dn/dT [1/K]	$3.66 \cdot 10^{-6}$ [80, 81]	$(3.66 - 2.03x) \cdot 10^{-4}$ [21, 80, 81]	$1.79 \cdot 10^{-4}$

Table C.1: Material parameters of GaAs and $Al_xGa_{1-x}As$, calculated for an aluminum contribution of $x = 0.92$. In this table, n and dn/dT are specified for a wavelength of 1064 nm.

The AlGaAs coating at 1064 nm consisted of 23.5 bilayers of GaAs and $Al_{0.92}Ga_{0.08}As$. Each bilayer was made of a one quarter-wave GaAs and one quarter-wave $Al_{0.92}Ga_{0.08}As$ layer. At 1064 nm, the optical thickness of each quarter-wave layer was 266 nm. For the high-index GaAs layers, this resulted in a geometrical thickness of 76.44 nm and for the low-index $Al_{0.92}Ga_{0.08}As$ layers in a geometrical thickness of 89.26 nm (for this calculation, the refractive indices from table C.1 were used). Thus, the GaAs layers were a factor 0.856 thinner, than the $Al_{0.92}Ga_{0.08}As$ layers and the coating contained more $Al_{0.92}Ga_{0.08}As$. Thus, the overall coating material parameters were calculated as weighted mean values.

$$k_{\text{th, AlGaAs}} = \frac{0.856 \cdot 55 + 69.9}{0.856 + 1} \frac{\text{W}}{\text{mK}} = 63.0 \frac{\text{W}}{\text{mK}} \tag{C.1}$$

$$c_{\text{w, AlGaAs}} = \frac{0.856 \cdot 330 + 440}{0.856 + 1} \frac{\text{J}}{\text{kgK}} = 389.27 \frac{\text{J}}{\text{kgK}} \tag{C.2}$$

$$\rho_{\mathrm{AlGaAs}} = \frac{0.856 \cdot 5320 + 3884.8}{0.856 + 1} \frac{\mathrm{kg}}{\mathrm{m}^3} = 4546.72 \frac{\mathrm{kg}}{\mathrm{m}^3} \tag{C.3}$$

$$\frac{\mathrm{d}n}{\mathrm{d}T}_{\mathrm{AlGaAs}} = \frac{(0.856 \cdot 3.66 + 1.79) \cdot 10^{-4}}{0.856 + 1} \frac{1}{\mathrm{K}} = 2.66 \cdot 10^{-4} \frac{1}{\mathrm{K}} \tag{C.4}$$

$$a_{\mathrm{th,\,AlGaAs}} = \frac{(0.856 \cdot 5.73 + 5.24) \cdot 10^{-6}}{0.856 + 1} \frac{1}{\mathrm{K}} = 5.47 \cdot 10^{-6} \frac{1}{\mathrm{K}} \tag{C.5}$$

The $k_{\mathrm{th,\,AlGaAs}}$, $c_{\mathrm{w,\,AlGaAs}}$ and ρ_{AlGaAs} are the parameters which were used in the COMSOL simulations. $\mathrm{d}n/\mathrm{d}T_{\mathrm{AlGaAs}}$ and $a_{\mathrm{th,\,AlGaAs}}$ were used in TkSim.

C.2 Material Parameters at 1550 nm

	GaAs	$\mathrm{Al}_x\mathrm{Ga}_{1-x}\mathrm{As}$	$\mathrm{Al}_{0.92}\mathrm{Ga}_{0.08}\mathrm{As}$
n	3.38 [26]		2.93 [26]
$\mathrm{d}n/\mathrm{d}T$ [1/K]	$2.04 \cdot 10^{-6}$ [80, 81]	$(2.04 - 0.3x) \cdot 10^{-4}$ [21, 80, 81]	$1.76 \cdot 10^{-4}$

Table C.2: Refractive indices and thermorefractive coefficients of GaAs and $\mathrm{Al}_x\mathrm{Ga}_{1-x}\mathrm{As}$, calculated for an aluminum contribution of $x = 0.92$. In this table, n and $\mathrm{d}n/\mathrm{d}T$ are specified for a wavelength of 1550 nm.

The AlGaAs coating at 1550 nm consisted of 26.5 bilayers of the high-index GaAs and low-index $\mathrm{Al}_{0.92}\mathrm{Ga}_{0.08}\mathrm{As}$. One bilayer was made of a quarter-wave GaAs layer and a quarter-wave $\mathrm{Al}_{0.92}\mathrm{Ga}_{0.08}\mathrm{As}$ layer. The optical thickness of a quarter-wave layer was 387.5 nm, resulting in a geometrical thickness of 114.64 nm (GaAs) and 132.25 nm ($\mathrm{Al}_{0.92}\mathrm{Ga}_{0.08}\mathrm{As}$) (for this calculation, the refractive indices from table C.2 were used). Thus, the coating at 1550 nm had a total geometrical thickness of 6.5 μm. The GaAs layers were a factor of 0.867 thinner than the $\mathrm{Al}_{0.92}\mathrm{Ga}_{0.08}\mathrm{As}$ layers. Since this factor is almost the same as the one for the AlGaAs coating specified at 1064 nm, also the difference in thermal conductivity $k_{\mathrm{th,\,AlGaAs}}$, density ρ_{AlGaAs} specific heat $c_{\mathrm{w,\,AlGaAs}}$ and thermal expansion $a_{\mathrm{th,\,AlGaAs}}$ was negligible and the parameters from C.1 were used. The thermorefractive coefficient was calculated using the data in table C.2

$$\frac{\mathrm{d}n}{\mathrm{d}T}_{\mathrm{AlGaAs,\,1550\,nm}} = \frac{(0.867 \cdot 2.04 + 1.76) \cdot 10^{-4}}{0.867 + 1} \frac{1}{\mathrm{K}} = 1.89 \cdot 10^{-4} \frac{1}{\mathrm{K}}. \tag{C.6}$$

Appendix D

Further resources

During this thesis, the programs TkSim and N.L.C.S. [50] from Nico Lastzka were used. The numerical simulation of the bow-tie resonator was carried out with a self-written C++ program from Tobias Meier. Further optical resonator simulations were performed with Finesse, versions 2.0 and 2.1 [36]. For the finite element simulations, COMSOL Multiphysics, version 5.2a was used and the numerical integration of the temperature profiles generated with COMSOL was carried out with Matlab, version R2014b. All plots in this thesis were generated with gnuplot, version 5.0. All schematic drawings were performed with Inkscape, version 0.91. For the schematic drawings of the experimental setups, the Component Library by Alexander Franzen and Jan Gniesmer was used. The simulation of various electronic filters was performed with Filter Pro from Texas Instruments. The CAD drawings of the mechanical components used in this thesis were made with various student versions of Autodesk Inventor 2012 – 2017. Calculations of mean values and standard deviations during the AlGaAs coating absorption and the sapphire substrate absorption measurements were performed with OpenOffice Calc, version 4. All mode-matchings were calculated with JamMt, version 0.24 which was programmed by Andre Thüring and Nico Lastzka. This thesis was written with TeXnicCenter version 2.02 and MiKTeX version 2.9.

Acknowledgements

First I would like to thank my parents for their never ending support during my studies and during my PhD. Thank you very much!
I would like to thank my supervisor, Prof. Roman Schnabel for giving me the opportunity to make my master thesis and my PhD thesis in his group. Thank you very much for your support and help.
Special thanks go to Sebastian, Jan, Daniela, Julian, Mikhail, Lisa, Jascha and my father for the proof reading of this thesis.
Furthermore I would like to thank Sebastian, Stefan, Mikhail and Axel for fruitful discussions resulting in an increase of my knowledge about physics.
I also thank the Hannover people, especially Andreas, Philipp and Jörg from the E-workshop, Philipp from the mechanical workshop and to Klaus from the IT department. I thank Prof. Danzmann for making the AEI Hannover to such a great place for research. I also thank Prof. Sengstock for making the ILP to an excellent place for science.
I also want to thank my former office colleagues Melanie, Christoph and Axel for the pleasant and cheerful times.

Thank your very much!

Eidesstattliche Versicherung / Declaration on oath

Hiermit versichere ich an Eides statt, die vorliegende Dissertationsschrift selbst verfasst und keine anderen als die angegebenen Hilfsmittel und Quellen benutzt zu haben.

Die eingereichte schriftliche Fassung entspricht der auf dem elektronischen Speichermedium.

Die Dissertation wurde in der vorgelegten oder einer ähnlichen Form nicht schon einmal in einem früheren Promotionsverfahren angenommen oder als ungenügend beurteilt.

Hamburg, den 16.03.2018

Unterschrift des Doktoranden

Bibliography

[1] B. P. Abbott and Abbott et al. Gw170104: Observation of a 50-solar-mass binary black hole coalescence at redshift 0.2. *Phys. Rev. Lett.*, 118:221101, Jun 2017.

[2] B. P. et al. Abbott. Gw151226: Observation of gravitational waves from a 22-solar-mass binary black hole coalescence. *Phys. Rev. Lett.*, 116:241103, Jun 2016.

[3] B. P. et al. Abbott. Observation of gravitational waves from a binary black hole merger. *Phys. Rev. Lett.*, 116:061102, Feb 2016.

[4] B. P. et al. Abbott. Gw170814: A three-detector observation of gravitational waves from a binary black hole coalescence. *Phys. Rev. Lett.*, 119:141101, Oct 2017.

[5] B. P. et al. Abbott. Gw170817: Observation of gravitational waves from a binary neutron star inspiral. *Phys. Rev. Lett.*, 119:161101, Oct 2017.

[6] Rana X. Adhikari. Gravitational radiation detection with laser interferometry. *Rev. Mod. Phys.*, 86:121–151, Feb 2014.

[7] A. Alexandrovski, Martin Fejer, and Roger Route A. Markosian. Photothermal common-path interferometry (pci): new developments. https://doi.org/10.1117/12.814813, 2009.

[8] Roger Route Alexei Alexandrovski, Martin Fejer. Optical absorption measurements in sapphire, June 2003.

[9] Ulrik L Andersen, Tobias Gehring, Christoph Marquardt, and Gerd Leuchs. 30 years of squeezed light generation. *Physica Scripta*, 91(5):053001, 2016.

[10] Muzammil A. Arain, Volker Quetschke, Joseph Gleason, Luke F. Williams, Malik Rakhmanov, Jinho Lee, Rachel J. Cruz, Guido Mueller, D. B. Tanner, and David. H. Reitze. Adaptive beam shaping by controlled thermal lensing in optical elements. *Appl. Opt.*, 46(12):2153–2165, Apr 2007.

[11] Stefan Ast. New approaches in squeezed light generation: Quantum states of light with ghz squeezing bandwidth and squeezed light generation via the cascaded kerr effect. *PhD Thesis*, October 2015.

[12] Stefan Ast, Ramon Moghadas Nia, Axel Schönbeck, Nico Lastzka, Jessica Steinlechner, Tobias Eberle, Moritz Mehmet, Sebastian Steinlechner, and Roman Schnabel. High-efficiency frequency doubling of continuous-wave laser light. *Opt. Lett.*, 36(17):3467–3469, Sep 2011.

[13] Peter Aufmuth and Karsten Danzmann. Gravitational wave detectors. *New Journal of Physics*, 7(1):202, 2005.

[14] Hans-A. Bachor and Timothy C. Ralph. *A Guide to Experiments in Quantum Optics*. WILEY-VCH Verlag GmbH and Co. KGaA, 2 edition, 2004.

[15] Massimo Bassan. *Advanced Interferometers and the Search for Gravitational Waves*. Springer International Publishing, 1 edition, 2014.

[16] F. Benabid, M. Notcutt, L. Ju, and D.G. Blair. Rayleigh scattering in sapphire test mass for laser interferometric gravitational-wave detectors:: Ii: Rayleigh scattering induced noise in a laser interferometric-wave detector. *Optics Communications*, 170(1):9 – 14, 1999.

[17] Charlotte Bond, Daniel Brown, Andreas Freise, and Kenneth A. Strain. Interferometer techniques for gravitational-wave detection. *Living Reviews in Relativity*, 19(1):3, Feb 2017.

[18] Robert W. Boyd. *Nonlinear Optics, Third Edition*. Academic Press, 3rd edition, 2008.

[19] G. Breitenbach, S. Schiller, and J. Mlynek. Measurement of the quantum states of squeezed light. *Nature*, 387, May 1997.

[20] Amber L. Bullington. *Thermal loading and model frequency degeneracy in optical resonators for the Laser Interferometer Gravitational-Wave Observatory (LIGO)*. PhD thesis, January 2009.

[21] Tara Chalermsongsak, Evan D Hall, Garrett D Cole, David Follman, Frank Seifert, Koji Arai, Eric K Gustafson, Joshua R Smith, Markus Aspelmeyer, and Rana X Adhikari. Coherent cancellation of photothermal noise in gaas/al 0.92 ga 0.08 as bragg mirrors. *Metrologia*, 53(2):860, 2016.

[22] Simon Chelkowski. *Squeezed Light and Laser Interferometric Gravitational Wave Detectors*. PhD thesis, Leibniz Universität Hannover, 2007.

[23] The LIGO Scientific Collaboration. Advanced ligo. *Classical and Quantum Gravity*, 32(7):074001, 2015.

[24] The Virgo Collaboration. The virgo physics book, vol. ii - optics and related topics, 12 2005.

[25] CORNING. HPFS Industrial Grade Product Information Sheet. https://www.corning.com/media/worldwide/csm/documents/acc05106b701420999327978ea88a83b4.pdf. Accessed: 2018-03-08.

[26] Cole Garrett D., Zhang Wei, Martin Michael J., Ye Yun, and Aspelmeyer Markus. Tenfold reduction of brownian noise in high-reflectivity optical coatings. *Nature Photonics*, 7, 2013.

[27] Stefan L. Danilishin and Farid Ya. Khalili. Quantum measurement theory in gravitational-wave detectors. *Living Reviews in Relativity*, 15(1):5, Apr 2012.

[28] Bradley J. Frey Douglas B. Leviton. Temperature-dependent absolute refractive index measurements of synthetic fused silica. https://doi.org/10.1117/12.672853, 2006.

[29] R. W. P. Drever, J. L. Hall, F. V. Kowalski, J. Hough, G. M. Ford, A. J. Munley, and H. Ward. Laser phase and frequency stabilization using an optical resonator. *Applied Physics B*, 31(2):97–105, Jun 1983.

[30] B. P. Abbott et al., (LIGO Scientific Collaboration, and Virgo Collaboration). Gw170608: Observation of a 19 solar-mass binary black hole coalescence. *The Astrophysical Journal Letters*, 851(2):L35, 2017.

[31] Liyuan Zhang et al. The coating scattering and absorption measurements of ligo i mirrors at caltech, 2008.

[32] Noboru Uehara et al. Modeling of efficient mode-matching and thermal-lensing effect on a laser-beam coupling into a mode-cleaner cavity. *Proc.SPIE*, 2989:2989 – 2989 – 12, 1997.

[33] Takashi Uchiyama et al. Reduction of thermal fluctuations in a cryogenic laser interferometric gravitational wave detector. *Phys. Rev. Lett.*, 108:141101, Apr 2012.

[34] M. M. Fejer, G. A. Magel, D. H. Jundt, and R. L. Byer. Quasi-phase-matched second harmonic generation: tuning and tolerances. *IEEE Journal of Quantum Electronics*, 28(11):2631–2654, Nov 1992.

[35] Janyce Franc, Nazario Morgado, Raffaele Flaminio, Ronny Nawrodt, Iain Martin, Liam Cunningham, Alan Cumming, Sheila Rowan, and James Hough. Mirror thermal noise in laser interferometer gravitational wave detectors operating at room and cryogenic temperature. 12 2009. Accessed: 2018-03-11.

[36] Andreas Freise. Finesse. http://www.gwoptics.org/finesse, 2017.

[37] C.C. Gerry and P.L. Knight. *Introductory Quantum Optics*. Cambridge University Press, 2005.

[38] Gregory Harry. *Optical Coatings and Thermal Noise in Precision Measurement*. Cambridge University Press, 2012.

[39] Joel Heersink, Vincent Josse, Gerd Leuchs, and Ulrik L. Andersen. Efficient polarization squeezing in optical fibers. *Opt. Lett.*, 30(10):1192–1194, May 2005.

[40] Hello, Patrice and Vinet, Jean-Yves. Analytical models of thermal aberrations in massive mirrors heated by high power laser beams. *J. Phys. France*, 51(12):1267–1282, 1990.

[41] Ioffe Institute. AlGaAs, Basic Parameters at 300 K. url-http://www.ioffe.ru/SVA/NSM/Semicond/AlGaAs/basic.html. Accessed: 2018-02-12.

[42] Ioffe Institute. AlGaAs, Thermal Properties. url-http://www.ioffe.ru/SVA/NSM/Semicond/AlGaAs/thermal.html. Accessed: 2018-02-12.

[43] Ioffe Institute. GaAs, Basic Parameters at 300 K. url-http://www.ioffe.ru/SVA/NSM/Semicond/GaAs/basic.html. Accessed: 2018-02-12.

[44] Ioffe Institute. GaAs, Thermal Properties. url-http://www.ioffe.ru/SVA/NSM/Semicond/GaAs/thermal.html. Accessed: 2018-02-12.

[45] Alexander Khalaidovski. Der optische kerr-effekt im fabry-perot interferometer. *Diploma Thesis*, March 2007.

[46] Alexander Khalaidovski, André Thüring, Henning Rehbein, Nico Lastzka, Benno Willke, Karsten Danzmann, and Roman Schnabel. Strong reduction of laser power noise by means of a kerr nonlinear cavity. *Phys. Rev. A*, 80:053801, Nov 2009.

[47] M. Kitagawa and Y. Yamamoto. Number-phase minimum-uncertainty state with reduced number uncertainty in a kerr nonlinear interferometer. *Phys. Rev. A*, 34:3974–3988, Nov 1986.

[48] Nico Lastzka. Analyse nichtlinearer resonatoren. *Diploma Thesis*, May 2005.

[49] Nico Lastzka. *Thermal Kerr effect*, 2009.

[50] Nico Lastzka. *Numerical modelling of classical and quantum effects in non-linear optical systems*. PhD thesis, Leibniz Universität Hannover, Sept 2010.

[51] Nico Lastzka, Jessica Steinlechner, Sebastian Steinlechner, and Roman Schnabel. Measuring small absorptions by exploiting photothermal self-phase modulation. *Appl. Opt.*, 49(28):5391–5398, Oct 2010.

[52] Uld Leonardt. *Measuring the Quantum State of Light*. Cambridge University Press, 1997.

[53] Ruo-Ding Li and Prem Kumar. Squeezing in traveling-wave second-harmonic generation. *Opt. Lett.*, 18(22):1961–1963, Nov 1993.

[54] COMSOL Multiphysics 5.2 Material Library, 2017.

[55] Joji Maeda, Ichiro Matsuda, and Yutaka Fukuchi. Analysis of amplitude squeezing of harmonic generation in a quasi-phase-matched device: effect of stochastic variation of domain length. *J. Opt. Soc. Am. B*, 17(6):942–951, Jun 2000.

[56] David McClelland, Nergis Mavalvala, Yanbei Chen, and Roman Schnabel. Advanced interferometry, quantum optics and optomechanics in gravitational wave detectors. 5:677 – 696, 03 2011.

[57] Moritz Mehmet. Gequetschtes licht bei 532 nm, 2006.

[58] Helge Müller-Ebhardt, Henning Rehbein, Roman Schnabel, Karsten Danzmann, and Yanbei Chen. Entanglement of macroscopic test masses and the standard quantum limit in laser interferometry. *Phys. Rev. Lett.*, 100:013601, Jan 2008.

[59] L. Noirie, P. Vidaković, and J. A. Levenson. Squeezing due to cascaded second-order nonlinearities in quasi-phase-matched media. *J. Opt. Soc. Am. B*, 14(1):1–10, Jan 1997.

[60] Horst Weber Norman Hodgson. *Laser Resonators and Beam Propagation*. Springer, New York, NY, 1 edition, 1997.

[61] OSI Optoelectronics. Photodiode characteristics and applications. Technical report, OSI Optoelectronics, 2016.

[62] Patrice Hello and Jean-Yves Vinet. Numerical model of transient thermal effects in high power optical resonators. *J. Phys. I France*, 3(3):717–732, 1993.

[63] Maria Principe. Reflective coating optimization for interferometric detectors of gravitational waves. *Opt. Express*, 23(9):10938–10956, May 2015.

[64] V. Quetschke, J. Gleason, M. Rakhmanov, J. Lee, L. Zhang, K. Yoshiki Franzen, C. Leidel, G. Mueller, R. Amin, D. B. Tanner, and D. H. Reitze. Adaptive control of laser modal properties. *Opt. Lett.*, 31(2):217–219, Jan 2006.

[65] Henning Rehbein. Optische bistabilität und gequetschtes licht in einem kerr-interferometer. *Diploma Thesis*, September 2004.

[66] Henning Rehbein. *On the enhancement of future gravitational wave laser interferometers and the prospects of probing macroscopic quantum mechanics*. PhD thesis, Leibniz Universität Hannover, 2009.

[67] Henning Rehbein, Jan Harms, Roman Schnabel, and Karsten Danzmann. Optical transfer functions of kerr nonlinear cavities and interferometers. *Phys. Rev. Lett.*, 95:193001, Nov 2005.

[68] S. Reynaud, C. Fabre, E. Giacobino, and A. Heidmann. Photon noise reduction by passive optical bistable systems. *Phys. Rev. A*, 40:1440–1446, Aug 1989.

[69] Roman Schnabel. Einstein-podolsky-rosen˘entangled motion of two massive objects. *Phys. Rev. A*, 92:012126, Jul 2015.

[70] Roman Schnabel. Lecture 'nichtklassisches licht', 2016.

[71] Roman Schnabel. Squeezed states of light and their applications in laser interferometers. *Physics Reports*, 684(Supplement C):1 – 51, 2017.

[72] D. K. Serkland, Prem Kumar, M. A. Arbore, and M. M. Fejer. Amplitude squeezing by means of quasi-phase-matched second-harmonic generation in a lithium niobate waveguide. *Opt. Lett.*, 22(19):1497–1499, Oct 1997.

[73] Anthony E. Siegman. *Lasers*. University Science Books, 1 edition, 1986.

[74] Amrit Pal Singh. Aufbau eines gefalteten wanderwellenresonators zur beobachtung des kaskadierten kerr-effekts bei 1550 nm, 2013.

[75] Jessica Steinlechner. *Optical Absorption Measurements for Third Generation Gravitational Wave Detectors*. PhD thesis, Leibniz Universität Hannover, 2013.

[76] Jessica Steinlechner, Stefan Ast, Christoph Krüger, Amrit Pal Singh, Tobias Eberle, Vitus Händchen, and Roman Schnabel. Absorption measurements of periodically poled potassium titanyl phosphate (ppktp) at 775 nm and 1550 nm. *Sensors*, 13(1):565–573, 2013.

[77] Jessica Steinlechner, Lars Jensen, Christoph Krüger, Nico Lastzka, Sebastian Steinlechner, and Roman Schnabel. Photothermal self-phase-modulation technique for absorption measurements on high-reflective coatings. *Appl. Opt.*, 51(8):1156–1161, Mar 2012.

[78] Sebastian Steinlechner. Gequetschtes licht bei 1550 nm. *Diploma Thesis*, March 2004.

[79] Yuishi Takeno, Mitsuyoshi Yukawa, Hidehiro Yonezawa, and Akira Furusawa. Observation of -9 db quadrature squeezing with improvement of phase stability in homodyne measurement. *Opt. Express*, 15(7):4321–4327, Apr 2007.

[80] J. Talghader and J. S. Smith. Thermal dependence of the refractive index of gaas and alas measured using semiconductor multilayer optical cavities. *Applied Physics Letters*, 66(3):335–337, 1995.

[81] J. Talghader and J. S. Smith. Erratum: "thermal dependence of the refractive index of gaas and alas measured using semiconductor multilayer optical cavities" [appl. phys. lett. 66, 335 (1995)]. *Applied Physics Letters*, 69(17):2608–2608, 1996.

[82] ET Science Team. Einstein gravitational wave telescope conceptual design study. Technical report, European Commission, 6 2011.

[83] André Thüring. *Investigations of coupled and Kerr non-linear optical resonators*. PhD thesis, Leibniz Universität Hannover, 2009.

[84] André Thüring and Roman Schnabel. Critical kerr nonlinear optical cavity in the presence of internal loss and driving noise. *Phys. Rev. A*, 84:033839, Sep 2011.

[85] Takayuki Tomaru, Takashi Uchiyama, Daisuke Tatsumi, Shinji Miyoki, Masatake Ohashi, Kazuaki Kuroda, Toshikazu Suzuki, Akira Yamamoto, and Takakazu Shintomi. Cryogenic measurement of the optical absorption coefficient in sapphire crystals at 1.064 μm for the large-scale cryogenic gravitational wave telescope. *Physics Letters A*, 283(1):80 – 84, 2001.

[86] Henning Vahlbruch. *Squeezed Light for GravitationalWave Astronomy*. PhD thesis, Leibniz Universität Hannover, 2008.

[87] Henning Vahlbruch. Generation of squeezed light, 2017. Talk IMPRS LW3.

[88] Henning Vahlbruch, Moritz Mehmet, Karsten Danzmann, and Roman Schnabel. Detection of 15 db squeezed states of light and their application for the absolute calibration of photoelectric quantum efficiency. *Phys. Rev. Lett.*, 117:110801, Sep 2016.

[89] D.F. Walls and G.J. Milburn. *Quantum Optics*. Springer Berlin Heidelberg, 2 edition, 2008.

[90] Andrew White. *Classical and quantum dynamics of optical frequency conversion*. PhD thesis, Australian National University, 1997.

[91] Andrew G White, Ping Koy Lam, David E McClelland, Hans-A Bachor, and William J Munro. Kerr noise reduction and squeezing. *Journal of Optics B: Quantum and Semiclassical Optics*, 2(4):553, 2000.

[92] W. Winkler, K. Danzmann, A. Rüdiger, and R. Schilling. Heating by optical absorption and the performance of interferometric gravitational-wave detectors. *Phys. Rev. A*, 44:7022–7036, Dec 1991.

[93] Ling-An Wu, H. J. Kimble, J. L. Hall, and Huifa Wu. Generation of squeezed states by parametric down conversion. *Phys. Rev. Lett.*, 57:2520–2523, Nov 1986.

[94] K. S. Zhang, T. Coudreau, M. Martinelli, A. Maître, and C. Fabre. Generation of bright squeezed light at 1.06 μm using cascaded nonlinearities in a triply resonant cw periodically-poled lithium niobate optical parametric oscillator. *Phys. Rev. A*, 64:033815, Aug 2001.